UNIVERSIDAD DE GRANADA

FACULTAD DE CIENCIAS

Departamento de Química Inorgánica

PROGRAMA DE DOCTORADO EN QUÍMICA

TESIS DOCTORAL

TRANSFORMADO DE GELES ORGÁNICOS Y RESIDUOS PLÁSTICOS EN MATERIALES AVANZADOS PARA LA REDUCCIÓN ELECTRO-CATALÍTICA DE DIÓXIDO DE CARBONO Y OXÍGENO

Jesica Castelo Quibén

Granada, Mayo 2019

Editor: Universidad de Granada. Tesis Doctorales
Autor: Jesica Castelo Quibén
ISBN: 978-84-1306-213-6
URI: http://hdl.handle.net/10481/55925


UNIVERSITAS · GRANATENSIS
PLUS
ULTRA
· 1531 ·

TRANSFORMADO DE GELES ORGÁNICOS Y RESIDUOS PLÁSTICOS EN MATERIALES AVANZADOS PARA LA REDUCCIÓN ELECTRO-CATALÍTICA DE DIÓXIDO DE CARBONO Y OXÍGENO

por

JESICA CASTELO QUIBÉN

Memoria presentada para optar al grado de Doctor

por la Universidad de Granada

Fdo.: Jesica Castelo Quibén

Licenciada en Química

Los Directores de la Tesis

Prof. Dr. Francisco Carrasco Marín

Catedrático del Departamento de Química Inorgánica,

Universidad de Granada

Prof. Dr. Agustín Francisco Pérez Cadenas

Catedrático del Departamento de Química Inorgánica,

Universidad de Granada


UNIVERSITAS · GRANATENSIS
PLUS
ULTRA
· 1531 ·

Francisco Carrasco Marín y Agustín Francisco Pérez Cadenas como directores de la presente Tesis Doctoral y la doctoranda Jesica Castelo Quibén

GARANTIZAN QUE

el trabajo ha sido realizado por el doctorando respetando los derechos de otros autores a ser citados cuando se han utilizado sus resultados o publicaciones.

Y para que conste a los efectos oportunos, en el cumplimiento de la legislación vigente, firmamos el presente certificado en Granada a 24 de Mayo de 2019.

Fdo.: Francisco Carrasco Marín

Catedrático de Química Inorgánica de

la Universidad de Granada

Fdo.: Agustín F. Pérez Cadenas

Catedrático de Química Inorgánica de

la Universidad de Granada

Fdo.: Jesica Castelo Quibén

Licenciada en Química


UNIVERSITAS · GRANATENSIS
PLUS
ULTRA
· 1531 ·

“Que ser valiente no salga tan caro,

que ser cobarde no valga la pena”

Joaquín Sabina

“Dende aquí vexo un camiño que non sei adónde vai,

polo mismo que n’o sei quixera o poder andar”

Rosalía de Castro


UNIVERSITAS · GRANATENSIS
PLUS
ULTRA
· 1531 ·

Agradecimientos

No puedo comenzar sino agradeciendo a mis Directores de Tesis, Prof. Dr. Agustín Pérez Cadenas y Prof. Dr. Francisco Carrasco Marín su dirección durante el camino que me llevó hasta la defensa de esta Tesis Doctoral, que es tan mía como suya. A vosotros os agradezco todo lo que me habéis enseñado, el apoyo que me habéis brindado, la ayuda, los ánimos y los consejos, los grandes ratos que hemos pasado, en definitiva, no solo por la dirección sino por la gran amistad que me habéis regalado, GRACIAS.

Quiero agradecer también al Prof. Dr. Carlos Moreno, por darme la oportunidad de realizar mi Tesis Doctoral en el Grupo de Investigación de Materiales de Carbón de la Universidad de Granada. De igual modo, agradecer a todos los profesores del Grupo, Pepe Rivera, Isa, María Ángeles y en especial, a mi Paco Pepe, gracias por todo lo que me habéis enseñado, por el cariño y la amistad. Sergio y Luisa, que alegría trabajar con vosotros! gracias por toda la ayuda, el cariño y los buenos momentos. Os deseo lo mejor en vuestro nuevo hogar con la pequeña Amelia.

A mis compañeros, con los que empecé, en especial Esthercita, Jose y Hakim, con vosotros he pasado los mejores momentos en este laboratorio, gracias por ayudarme en los primeros pasos y en los que siguieron, gracias por todo amigos míos, os deseo lo mejor en vuestras carreras y nos vemos pronto en el Menorca. A Nere, mucho ánimo con tus dos Tesis, ole tú! A Safae, te deseo lo mejor y que continúes con esa alegría contagiosa. Al resto de compañeros y estancias que han pasado por este laboratorio y han dejado huella, Hesham, Mary, Amra, Said, Ilaria, Bruno, Stefi, Sonia, Luis, Diana, y en especial a mis amiguitas del alma Adri, Karol y Eli, que bien nos lo hemos pasado! Cuando hemos llorado XD! qué suerte la mía de teneros…!

Gracias también al grupo de Carbones de la Universidad de Jaén, Miguel Ángel y Vicky, gracias por la amistad.

Agradecer a la Prof. Vanessa Fierro por acogerme y darme la oportunidad de realizar mi estancia predoctoral en el Grupo de Bio-sourced Materials del

Institute Jean Lamour. A todos mis compañeros y amigos que conocí en Épinal, Jime (todavía nos quedan muchos Catanes por jugar), Oussamita (un viaje en globo inolvidable), Ángela, Giuseppe, Sebastien, Zèlie, Lalo, Blagoj, Phillipe, con vosotros he pasado los -15 ºC más cálidos de mi vida.

Dar las gracias a todos los miembros del Departamento de Química Inorgánica, por ayudarme siempre que lo he necesitado, en especial, a Mari Carmen, a Antonio de la Torre, a María Ángeles y a Puri, con las que que además tuve el placer de compartir docencia.

Gracias a los miembros del Centro de Investigación Científica de la Universidad de Granada, en especial a Pablo, a Bendi y a María del Mar, es un placer trabajar con vosotros.

A mis amigos, de norte a sur, que siempre han estado ahí, Lidia, Fran, Marina, Cesc, Sonia, Eri, Chuchi, Palom, Ta y Celi, y sobre todo a Berta, a Luis y a Jose, por todo lo que hemos vivido y lo que nos queda por vivir!

A mi familia en general por apoyarme y animarme siempre, a mi madre y mis hermanos que gracias a ellos estoy hoy aquí y sé el enorme orgullo que sienten, a mi padre, que sé que lo sentiría más si cabe.

Y por supuesto, a Ale, mi mejor amigo, mi compañero de viaje. No hay palabras con las que pueda expresar lo agradecida que me siento. Soy tremendamente afortunada. GRACIAS.

Jesica Castelo Quibén agradece la financiación recibida a través del contrato predoctoral asociado a proyectos de investigación de excelencia de la Junta de Andalucía. Este Trabajo de Investigación ha sido financiando por la Junta de Andalucía mediante el proyecto P12-RNM-2892 y el Grupo de Investigación RNM-172.

La doctoranda y los directores también quieren agradecer la financiación por parte de distintas entidades: Ministerio de Economía y Competitividad, Fondos FEDER, proyecto CTQ2013-44789-R y ERASMUS+.

a mis hermanos Hugo, Marcos y Edgar

a mis padres Guada y Chema


UNIVERSITAS · GRANATENSIS
PLUS
ULTRA
· 1531 ·

CONTENIDO Y ESTRUCTURA DE LA TESIS


UNIVERSITAS · GRANATENSIS
PLUS
ULTRA
· 1531 ·

CONTENIDO Y ESTRUCTURA DE LA TESIS

En la presente Tesis Doctoral se describe la preparación de distintos materiales de carbono y su utilización en aplicaciones electroquímicas: en las reacciones de electro-reducción de oxígeno (ORR) y electro-reducción de CO_2 a hidrocarburos. Los materiales de carbono fueron preparados a partir de residuos plásticos, así como a partir de polímeros comerciales y otros polímeros sintetizados de tipo bencenodiol-formaldehído.

Los materiales de carbono fueron minuciosamente caracterizados tanto a nivel textural, como a nivel químico y las reacciones de electro-reducción se llevaron a cabo en diferentes celdas electroquímicas dotadas con sistemas de 3 electrodos.

El **capítulo I** ***(Introducción y Objetivos)*** analiza la situación energética actual junto con la crisis medioambiental que estamos sufriendo hoy en día, lo que sustenta el marco teórico para la elaboración de la presente tesis doctoral. A lo largo de este capítulo de *Introducción* también se comenta la utilidad de las pilas de combustible y de la obtención de hidrocarburos a partir de CO_2 además del papel que juegan en la situación actual y las prospectivas de futuro. Así mismo, se detallan las reacciones que tienen lugar dichos procesos.

Por otra parte, se describe la preparación de materiales de carbono y se trata en profundidad la versatilidad de los mismos junto con las ventajas que ofrecen en las presentes aplicaciones.

En el **capítulo II** ***(Materiales y Métodos)*** se describe la preparación de los materiales de carbono obtenidos, las técnicas empleadas para su caracterización y los métodos utilizados para llevar a cabo las aplicaciones de ORR y electro-reducción de CO_2. Además, se muestran las ecuaciones y modelos matemáticos aplicados para analizar los resultados.

El **capítulo III** ***(Metal-carbon-CNF composites obtained by catalytic pyrolysis of urban plastic residues as electro-catalysts for the reduction of CO2)*** muestra la síntesis, caracterización y aplicación de materiales de carbono a partir de residuos plásticos urbanos, en concreto, a partir de bolsas, cuyo principal componente es el polietileno de baja densidad. Los materiales descritos en este capítulo fueron dopados con metales de transición y, posteriormente, fueron empleados en la reacción de electro-reducción de CO_2 a hidrocarburos (metano, etano, etileno, propano, propileno y butano).

El **capítulo IV** ***(From Polyethylene to Highly Graphitic and Magnetic Carbon Spheres Nanocomposites: Carbonization under Pressure)*** trata sobre la obtención de microesferas de carbono altamente grafíticas a partir de polietileno de baja densidad (LDPE) comercial. Estos materiales se obtuvieron en un reactor de alta presión y a una temperatura relativamente baja. Durante el proceso de síntesis se añadieron precursores metálicos y se obtuvieron materiales de carbono dopados con Fe, Co y Ni. Fueron caracterizados minuciosamente mediante numerosas técnicas y se detallan los resultados obtenidos.

En el **capítulo V** ***(Electro-catalytic Behaviour of Highly Graphitic Carbon Spheres Nanocomposites for the Oxygen Reduction Reaction (ORR))*** se emplean los materiales obtenidos en el capítulo anterior en la reacción de electro-reducción de oxígeno. Además, se realiza una caracterización pormenorizada de los mismos, lo que complementa los resultados del capítulo anterior y, con todo ello, se realiza la discusión de los resultados electro-catalíticos obtenidos.

En el **capítulo VI** ***(Mesoporous Carbon Nanospheres with improved conductivity for electro-catalytic reduction of Oxygen and CO_2)*** se detalla la síntesis y caracterización de esferas de carbono mesoporosas obtenidas mediante el proceso sol-gel y la posterior

carbonización. Durante el proceso de síntesis, las esferas se doparon con nanoestructuras (nanotubos o nanohorns) y/o con Níquel. Este hecho, además de modificar las propiedades texturales, produjo una mejora significativa de la conductividad. Estos materiales fueron testeados como cátodos en las reacciones de electro-reducción de oxígeno y electro-reducción de CO_2.

El **capítulo VII** ***(Synthesis and Characterization of Carbon Spheres Doped with Nitrogen and Tungsten for the Oxygen Reduction Reaction)*** versa sobre la preparación, caracterización y aplicación de nanoesferas de carbono dopadas con wolframio. Las esferas (gel orgánico) se obtuvieron mediante polimerización solvotermal de pirocatecol y formaldehído en medio básico. Posteriormente, las esferas poliméricas se doparon con un precursor de wolframio y tras el proceso de pirólisis se obtuvieron las esferas de carbono recubiertas con wolframio. Estos materiales se aplicaron en la reacción de ORR.

El **capítulo VIII** ***(Conclusiones generales)*** recoge las conclusiones principales obtenidas durante el desarrollo de la presente tesis doctoral.

Parte de los resultados obtenidos durante el trabajo de investigación de esta Tesis Doctoral han sido publicados, o se encuentran bajo consideración, en revistas de alto índice de impacto y difusión internacional:

- Jesica Castelo-Quibén, Abdelhakim Elmouwahidi, Francisco J. Maldonado-Hódar, Francisco Carrasco-Marín and Agustín F. Pérez-Cadenas*, *"Metal-Carbon-CNF composites obtained by catalytic pyrolysis of urban plastic residues as electro-catalysts for the reduction of CO_2"* Catalysts, 2018, **8** (5), 198; DOI: 10.3390/catal8050198.

- Jesica Castelo-Quibén*, Luisa M. Pastrana-Martínez, Francisco Carrasco-Marín and Agustín F. Pérez-Cadenas, *"From Polyethylene to Highly Graphitic and Magnetic Carbon Spheres Nanocomposites: Carbonization under Pressure"* Nanomaterials, 2019, **9** (4), 606; DOI : 10.3390/nano9040606


UNIVERSITAS · GRANATENSIS
PLUS
ULTRA
· 1531 ·


UNIVERSITAS · GRANATENSIS
PLUS
ULTRA
· 1531 ·

ÍNDICE

CAPÍTULO I: INTRODUCCIÓN Y OBJETIVOS

CAPÍTULO II: MATERIALES Y MÉTODOS

CAPÍTULO V: ELECTRO-CATALYTIC BEHAVIOUR OF HIGHLY GRAPHITIC CARBON SPHERES NANOCOMPOSITES FOR THE OXYGEN REDUCTION REACTION (ORR)

CAPÍTULO VI: MESOPOROUS CARBON NANOSPHERES WITH IMPROVED CONDUCTIVITY FOR ELECTRO-CATALYTIC REDUCTION OF OXYGEN AND CO_2

CAPÍTULO VIII: CONCLUSIONES GENERALES


UNIVERSITAS · GRANATENSIS
PLUS
ULTRA
· 1531 ·


UNIVERSITAS · GRANATENSIS
PLUS
ULTRA
· 1531 ·

CAPÍTULO II

MATERIALES

Y

MÉTODOS


UNIVERSITAS · GRANATENSIS
PLUS
ULTRA
· 1531 ·

En el presente Capítulo II, *Materiales y Métodos,* se detallan los distintos procesos experimentales que se llevaron a cabo para obtener los materiales que forman parte de esta Tesis Doctoral. Además, se describen las técnicas utilizadas para su caracterización, tanto química como textural, así como los modelos que permitieron analizar los datos.

También se describe en detalle el diseño de las instalaciones donde se llevaron a cabo las reacciones de electro-reducción de oxígeno y electro-reducción de CO_2.

II.1. Preparación de los materiales

II.1.1. Materiales de carbono a partir de residuos plásticos.

Los residuos plásticos utilizados en este caso fueron bolsas usadas de supermercado, cuya composición principal es el polietileno de baja densidad (LDPE). Se obtuvieron 3 materiales compuestos carbono-nanofibras tras el dopado con Fe, Co y Ni.

La primera etapa en la preparación de estos materiales consistió en trocear y disolver 10g de bolsa en 100mL de *o*-xyleno a 80 ºC. A continuación, se añadieron 2g de hidróxido de Fe, de Co o de Ni. Esta mezcla, se continuó agitando durante 3 horas con el objetivo de distribuir el precursor metálico homogéneamente en la muestra. Esta mezcla se introdujo en un reactor cerrado de Parr Instrument (reactor modelo A1828HC2) y se aplicó un tratamiento térmico a 350 ºC durante 4 horas. El sólido obtenido se pirolizó en un reactor tubular bajo atmósfera de N_2 (300 mL/min) con una rampa de calentamiento de 10ºC/min hasta 900ºC y se mantuvo durante 2h a esa temperatura. Finalmente estos materiales fueron lavados con agua para eliminar las posibles impurezas. La figura II.1 representa el esquema de preparación de los materiales.

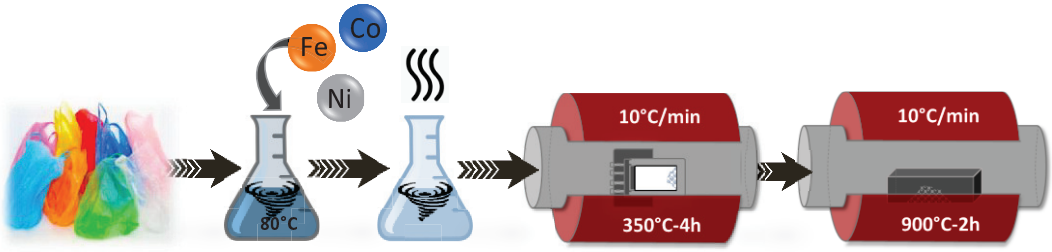

Figura II. 1. Esquema experimental de la preparación de las muestras

Los materiales así obtenidos se nombraron como PFe, PCo y PNi siendo Fe, Co y Ni el metal con el que fueron dopados respectivamente.

II.1.2. Microesferas de carbono a partir de polietileno de baja densidad (LDPE).

En este caso se partió, como materia prima, de polietileno de baja densidad (LDPE) puro, suministrado por Sigma-Aldrich, y se obtuvieron microesferas de carbono altamente grafíticas.

En primer lugar, 0.5 g de LDPE se introdujeron en un reactor cerrado de Hastelloy® de fabricación casera de 25 mL de capacidad y se aplicó un tratamiento térmico, con una velocidad de calentamiento de 10 ºC/min, hasta 700 ºC y se mantuvo 2 horas a esa temperatura. Esta experiencia se repitió varias veces con el objetivo de obtener un rendimiento medio del proceso (≈ 38.3%). Dicho rendimiento fue tenido en cuenta para calcular el precursor metálico necesario para obtener el carbono final dopado con un 10% teórico de Fe, Co o Ni. Como precursores metálicos se utilizaron el acetato de Fe, acetato de Co y acetato de Ni.

Así, 0.5 g de LDPE en polvo se mezclaron físicamente con los correspondientes acetatos y se realizó el mismo tratamiento térmico: 2 h a 700 ºC con una rampa de temperatura de 10 ºC/min. En la figura II.2 se muestra el esquema experimental.

Se obtuvieron los materiales PE, PE-Fe, PE-Co, PE-Ni

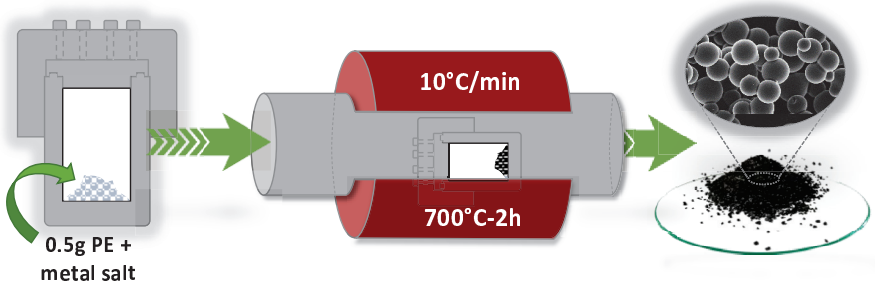

Figura II. 2. Esquema experimental de la preparación de las muestra PE, PE-Fe, PE-Co y PE-Ni

II.1.3. Nanoesferas de carbono mesoporosas con conductividad mejorada.

En este caso la preparación de las esferas se llevó a cabo mediante la condensación de resorcinol y formaldehído en presencia de diferentes surfactantes y añadiendo tanto Ni como nanoestructuras de carbono (nanotubos (MWCNTs) o nanoconos (SWNHs)) para mejorar su conductividad y su actividad catalítica. Esta policondensación se realizó mediante el método de emulsión inversa como se comenta a continuación.

II.1.3.1 Síntesis de xerogeles de carbono (sin dopar) (J y J-CTAB).

En primer lugar, el surfactante (S) fue dispersa en 900 mL de heptano y fueron calentados a 65ºC bajo reflujo y agitación (450rpm). Una vez estabilizada la temperatura, se añadió gota a gota una disolución con el resorcinol, formaldehído, agua y cierta cantidad de dodecilbenceno sulfonato sódico (DBSS). El DBSS se utiliza para facilitar la dispersión de los MWCNTs y SWNHs, en este caso se añadió de igual modo para mantener las condiciones de síntesis.

Las relaciones molares utilizadas en todos los casos fueron: F/R=2, W/R=14, R/S=4.5 y R/DBSS=245.

El gel R-F se mantuvo a 65 ºC durante 24 h bajo agitación, después, se filtró y se introdujo en acetona durante 5 días, renovando la acetona dos veces al día. Así se produjo el intercambio del disolvente del interior de los poros por acetona que, como ya se comentó en el Capítulo I, previene el colapso de la porosidad.

Pasados 5 días, se procedió al secado subcrítico: se secó en microondas durante periodos de 1 minuto a 300 W bajo atmósfera de argón hasta peso constante. De este modo se obtuvo el xerogel orgánico.

Finalmente, se aplicó un proceso de pirólisis para obtener el correspondiente xerogel de carbono. La carbonización se llevó a cabo en un horno tubular bajo atmósfera de N_2 (300 cm^3/min) hasta 900 ºC, con una velocidad de calentamiento de 1 ºC/min, y se mantuvo 2 h a esa temperatura.

Con el objetivo de estudiar la influencia de la naturaleza del surfactante, se utilizaron dos tipos de surfactantes: Span80 (no iónico) y Bromuro de hexadeciltrimetilamonio, CTAB (catiónico). Las muestras así obtenidas fueron “J” y “J-CTAB”.

II.1.3.2 Síntesis de xerogeles de carbono dopados con MWCNTs o SWNHs (JT y JH).

El procedimiento llevado a cabo en este caso, fue el mismo que el anterior, a excepción de que a la disolución de R-F con DBSS fue añadida también cierta cantidad de MWCNTs o SWNHs (Sigma Aldrich). Esta solución fue sonicada durante 30 min para permitir una buena dispersión de los nanomateriales antes de añadirla a la disolución de heptano y Span80. La cantidad de nanomateriales a añadir fue calculada para obtener xerogeles de carbono dopados con un 1% de nanomateriales, suponiendo un 50% de pérdida de masa durante el proceso de carbonización.

Tras el proceso de curado, secado y carbonización, se obtuvieron los materiales “JT” (dopado con MWCNT) y “JH” (dopado con SWNHs).

II.1.3.3 Síntesis de xerogeles de carbono dopados con Ni

La adición de níquel se llevó a cabo mediante dos métodos diferentes, pero en ambos casó se calculó y añadió la cantidad adecuada para obtener un 2% de níquel en el material de carbono final.

- *Método 1: dopado de Ni durante el proceso sol-gel.*
  A la mezcla R-F se le añadió la cantidad adecuada de acetato de níquel y se procedió de igual modo que anteriormente. De nuevo, se supuso un 50% de pérdida de masa durante el proceso de carbonización.

- *Método 2: dopado de Ni mediante impregnación incipiente.*
  En este caso, una vez obtenidos los materiales de carbono J, JT y JH, se mantuvieron a vacío durante toda la noche y posteriormente se añadió una disolución de acetato de Ni. El volumen de disolución utilizado fue el mismo volumen que V_{TOTAL} poroso de cada muestra, obtenido por porosimetría de intrusión de mercurio. A continuación, las muestras secaron a 120 ºC durante toda la noche y finalmente, se aplicó un tratamiento térmico a 350 ºC durante 2 h bajo atmósfera de N_2, para descomponer la sal.

Así, se obtuvieron las muestras J-Ni1, JT-Ni1, JH-Ni1, J-Ni2, JT-Ni2 y JH-Ni2.

A continuación se muestra un esquema experimental del proceso de síntesis de dichos materiales, además de una tabla resumen de la composición de los mismos.

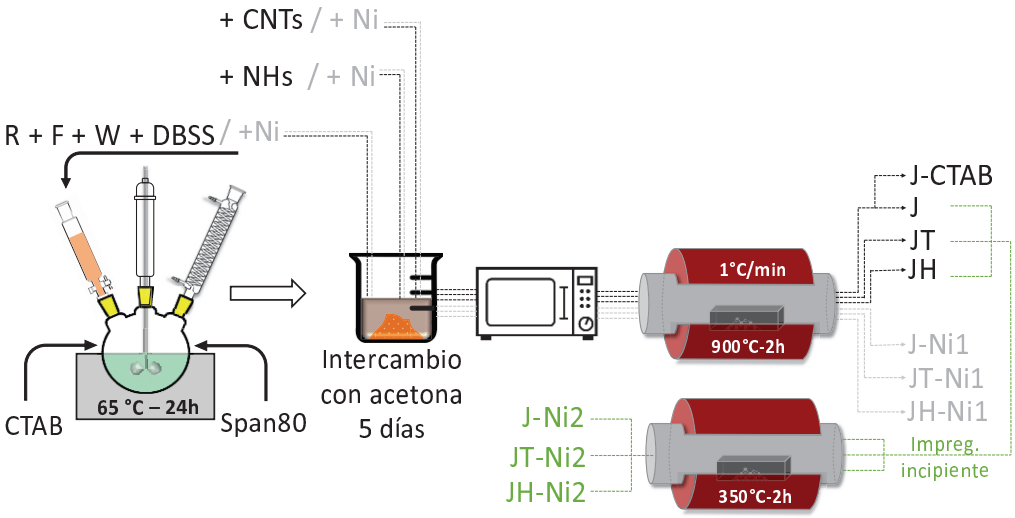

Figura II. 3. Esquema de síntesis.

Tabla II. 1. Tabla de composición de los materiales

Muestra	Método	Composición (% wt.)
J	Condensación R-F	Xerogel de C
JT	Condensación R-F	Xerogel de C + 1% MWCNTs
JH	Condensación R-F	Xerogel de C + 1% SWCNHs
J-Ni1	Dopado Ni durante condensación R-F	Xerogel de C + 2.0% Ni
JT-Ni1	Dopado Ni durante condensación R-F	Xerogel de C + 1% MWCNTs + 2.0% Ni
JH-Ni1	Dopado Ni durante condensación R-F	Xerogel de C + 1% SWCNHs + 2.0% Ni
J-Ni2	Condensación R-F + impregnación incipiente	Xerogel de C + 2.0% Ni
JT-Ni2	Condensación R-F + impregnación incipiente	Xerogel de C + 1% MWCNTs + 2.0% Ni
JH-Ni2	Condensación R-F + impregnación incipiente	Xerogel de C + 1% SWCNHs + 2.0% Ni

II.1.4. Nanoesferas de carbono dopadas con Wolframio.

Se obtuvieron nanoesferas poliméricas mediante síntesis sol-gel hidrotermal utilizando como monómeros pirocatecol y formaldehído en una disolución acuosa etanol:agua y en presencia de amoníaco. El procedimiento llevado a cabo es una extensión del método Stöber [1], concretamente siguiendo el procedimiento utilizado recientemente por Moreno *et. al* [2].

En primer lugar, se disolvió el pirocatecol en 60 mL de una disolución agua:EtOH en una relación de volúmenes 2.5:1, a continuación se añadió una disolución de NH_3 y el formaldehído. Esta mezcla se introdujo en un autoclave (Parr Instruments) de 100 mL de capacidad y se introdujo en una estufa a 100 ºC durante 24 horas.

Pasadas 24 horas se filtró el precipitado, se lavó con etanol y se realizó el intercambio del disolvente con acetona durante 3 días, cambiando la acetona diariamente. Finalmente, el material se secó bajo lámpara IR. La muestra de esferas de gel orgánico así obtenida se nombró como “S”,

La muestra S, fue carbonizada en atmósfera de N_2 en un horno tubular a 2 ºC/minuto hasta 900 ºC durante 2 h y se obtuvieron las esferas de carbono CS.

Por otra parte, la muestra S fue impregnada con una disolución de wolframato amónico, $[(NH_4)_2(WO_4)]$, mediante el método de impregnación incipiente. El volumen de disolución utilizado fue el V_{TOTAL} poroso de S obtenido mediante porosimetría de intrusión de mercurio. La impregnación se realizó con disoluciones de wolframato amónico de distinta concentración para obtener esferas dopadas con un 2%, 5% y 10% de W en el carbono final. Para hacer el cálculo, se supuso una pérdida de masa del 50% durante la carbonización. Así, se obtuvieron las muestras CSW2, CSW5 y CSW10.

II. 2. Técnicas de Caracterización

II. 2. 1 Caracterización textural

II. 2.1.1 Adsorción física de gases.

Las isotermas de adsorción de N_2 a -196 °C y de CO_2 a 0 °C fueron obtenidas en un equipo QUADRASORB-SI de la casa comercial Quantachrome Ins. Para ello, aproximadamente 0.1 g de muestra se introducen en un bulbo de 9 mm y se desgasifican a alto vacío (10^{-6} bar) a 110 °C durante 12 h. Los adsorbatos fueron nitrógeno (99.999 %) y dióxido de carbono (99.999 %) suministrados por Air Liquide.

A partir de las isotermas de N_2 se calcularon los siguientes parámetros: la superficie específica (S_{BET}) mediante el modelo propuesto por Brünauer, Emmett y Teller [3] (B.E.T.), el volumen de microporos (W_0) por el método de Dubinin-Radushkevich [4], la anchura media de microporos (L_0) a partir de la ecuación de Stoeckli [5] y el volumen de mesoporos (V_{meso}) aplicando el método de Barrett, Joyner y Halenda [6] (B.J.H.). En el caso de la isoterma de adsorción de CO_2 se obtuvieron también el volumen y la anchura media de los microporos más estrechos de la misma forma. Las ecuaciones y los distintos modelos empleados se describen a continuación.

II.2.1.1.1 Ecuación de B.E.T

El modelo de Brünauer-Emmett-Teller [3] se basa en la formación de una monocapa a bajas presiones, de manera que sabiendo la cantidad de moléculas adsorbida y la superficie que ocupa cada una de estas moléculas, podemos calcular la superficie total del adsorbente. El cálculo de la S_{BET} se lleva a cabo aplicando las Ecuaciones 2.1 y 2.2.

Ecuación 2.1

$$\frac{P}{V_{ads}(P_0 - P)} = \frac{1}{V_m C} + \frac{C-1}{V_m C}\frac{P}{P_0}$$

Ecuación 2.2

$$S_{BET}(m^2 g^{-1}) = V_m(cm^3 g^{-1}) \times \frac{1\ (mol)}{22400\ (cm^3)} \times N_A\left(\frac{molec}{mol}\right) \times 0.162\left(\frac{nm^2}{molec}\right) \times 10^{-18}\left(\frac{m^2}{nm^2}\right)$$

II.2.1.1.2 Ecuación de Dubinin-Radushkevich y ecuación de Stoeckly

El modelo de Dubinin-Radushkevich [4] es posterior y tiene en cuenta que la adsorción depende en gran medida del tamaño de poro, ya que para poros más pequeños la interacción adsorbato-adsorbente será más grande y, por lo tanto, a bajas presiones la adsorción se dará sólo en los microporos. Por ello, en lugar de suponer la formación de monocapa y a partir de la misma calcular la superficie, el modelo propuesto por Dubinin-Radushkevich (ecuaciones 2.3 y 2.4) se utiliza para calcular el volumen de microporos teniendo en cuenta que una vez adsorbido, el adsorbato va a pasar de estado gaseoso a líquido en el interior del poro.

Ecuación 2.3

$$W = W_0 exp\left[-\left(\frac{A}{\beta E_0}\right)^2\right]$$

Ecuación 2.4

$$A = RTln\left(\frac{P}{P_0}\right)$$

La ecuación se linealiza tomando logaritmos, de manera que a partir de la ordenada en el origen se obtiene el volumen de microporos (W_0) y de la pendiente se obtiene la energía de adsorción (E_0). La ecuación se aplica tanto a las isotermas de adsorción de nitrógeno a -196 °C como a las de dióxido de carbono a 0 °C, de manera que obtenemos dos valores $W_0(N_2)$ y $W_0(CO_2)$. Hay que tener en cuenta que a presión atmosférica el CO_2 sólo se puede adsorber en poros menores de 0.7 nm, por lo que el $W_0(CO_2)$

puede ser menor que el $W_0(N_2)$ en los casos en los que los microporos sean más anchos. Por el contrario, cuando existen constricciones a la entrada de los microporos la adsorción de nitrógeno se ve impedida y en este caso $W_0(CO_2)$ será mayor que $W_0(N_2)$. La anchura media de los microporos se puede obtener a partir de la Ecuación de Stoeckli [5] (Ecuación 2.5) o de Dubinin [7] (Ecuación 2.6) cuando E_0 es menor de 20 $kJ \cdot mol^{-1}$.

Ecuación 2.5

$$L_0(nm) = \frac{10.8}{(E_0 - 11.4\ KJ/mol)}$$

Ecuación 2.6

$$L_0(nm) = \frac{24}{E_0(KJ/mol)}$$

II.2.1.1.3 Método de B.J.H

Cuando se analizan muestras mesoporosas mediante adsorción de nitrógeno, las isotermas generalmente presentan ciclos de histéresis, es decir, la rama de adsorción y la de desorción no son coincidentes. Esto se debe a la forma en la que se produce la adsorción y la desorción en poros cilíndricos abiertos, lo que hace que para una presión relativa dada haya una cantidad de gas adsorbida, mientras que la presión relativa necesaria para desorber esta misma cantidad de gas será menor. El fenómeno de histéresis puede explicarse mediante la ecuación de Kelvin [8], que relaciona el radio de un poro con la presión relativa a la que es llenado en función de las características del sistema adsorbente-adsorbato. Basándose en esto se puede aplicar el modelo propuesto por Barrett, Joyner y Halenda [6] para calcular, generalmente a partir de la rama de desorción, tanto la distribución del tamaño de poros en la región

correspondiente al llenado de mesoporos como el volumen total de mesoporos.

II. 2.1.2 Porosimetría de intrusión de Mercurio

La porosimetría de intrusión de mercurio permite obtener el volumen total poroso (macroporos y mesoporos más grandes) así como la curva de distribución de tamaño de poros. Puesto que el mercurio tiene una tensión superficial muy alta, no moja la superficie del sólido y debe ser introducido en los poros a presión. De esta forma, a presiones más bajas se llenaran los poros más anchos y a presiones más altas los más estrechos. La relación entre el radio de un poro y la presión a la que hay que introducir el Hg para que penetre en el mismo viene dada por la Ecuación de Washburn [9] (ecuación 2.7).

Ecuación 2.7

$$r = \frac{-2\sigma cos\theta}{P}$$

De este modo se puede saber cuál es el tamaño del poro que se está llenando en función de la presión aplicada y así se puede obtener la curva de distribución de tamaño de poro. Las porosimetrías de mercurio se llevaron a cabo en un porosímetro modelo PoreMaster33 de la firma Quantachrome Instruments.

II. 2.1.3 Microscopía Electrónica de Barrido (SEM)

La morfología de las muestras se estudió mediante Microscopía Electrónica de Barrido (SEM). Las microfotografías se tomaron en un microscopio electrónico de alta resolución modelo GEMINI-1430-VP de la casa comercial LEO Carl Zeiss.

II. 2. 2 Caracterización química

II. 2.2.1. Análisis termogravimétrico (TGA)

El análisis termogravimétrico de los materiales nos permite conocer la estabilidad de los mismos frente a la oxidación (en caso de hacerlo en atmósfera oxidante) así como conocer en contenido de cenizas o el contenido total real de metal, en aquellos casos en los que el material de carbono provenga de un polímero puro.

Los experimentos se realizaron en un termobalanza Shimadzu modelo TGA-50H, bajo flujo de aire con una velocidad de calentamiento de 10 ºC/min hasta 950 ºC y manteniéndolo 30 minutos a esa temperatura.

II. 2.2.2. Difracción de Rayos-X (XRD)

Mediante XRD caracterizamos tanto la fase metálica como los clústeres grafíticos que se hayan podido formar. La difracción de rayos-X nos permite analizar las fases cristalinas (puesto que todos los sólidos cristalinos poseen su difractograma característico) y la comparación de los patrones obtenidos con las distintas bibliotecas disponibles (ej. cartas JCPDS) nos permite asignar inequívocamente las fases presentes.

Además, mediante la aplicación de la ecuación de Scherrer, podemos estimar el tamaño promedio del cristal:

Ecuación 2.8

$$D = \frac{0.9 \cdot \lambda}{\beta \cdot \cos(\theta)}$$

Donde D es el tamaño medio del cristal; K (=0.9) es el factor de forma del cristal y 0.9 es el valor más utilizado ya que está considerado una buena aproximación; λ es la longitud de onda de radiación utilizada (λ_{Cu}=0.15406 nm); β es la anchura a mitad de altura del pico considerado para el cálculo

(FWHM – full-width at half-maximum) y θ es el ángulo de Bragg, la posición del pico de difracción.

El equipo utilizado para llevar a cabo los análisis de difracción de rayos-X en polvo fue un difractómetro BRUKER D8 ADVANCE con radiación de Cu y detector LINXEYE.

II. 2.2.3. Microscopía Electrónica de Transmisión de Alta Resolución (HRTEM)

La microscopía de transmisión nos permite estudiar la morfología de la muestra además de conocer su composición y distribución de la fase metálica a través del material. Además, las líneas de alta resolución nos permiten diferenciar las fases cristalinas y estudiar las nanoestructuras de carbono.

Estos análisis se realizaron en un microscopio de ultra alta resolución TITAN G2 de la casa FEI.

II. 2.2.4. Espectroscopía de Fotoemisión de Rayos-X (XPS)

La espectroscopía de fotoemisión de Rayos-X (XPS) nos permite estudiar la química superficial de la muestra en su superficie más externa.

Los espectros de las muestras se obtuvieron con un espectrómetro de fotoelectrones de Rayos-X Kratos Axis Ultra-DLD, con fuente de Rayos-X de ánodo AlKα y un analizador hemiesférico de electrones. La fuente de rayos X operaba a 450W. Las regiones analizadas fueron siempre C y O además de cada uno de los metales presentes en las muestras.

Las señales correspondientes a cada región fueron deconvolucionadas usando funciones de tipo suma asimétricas Gaussianas-Lorentzianas para determinar el número de componentes, la energía de ligadura de los picos (B.E.) y las áreas de los mismos (análisis cuantitativo). La energía de ligadura del pico de la región C_{1s},

correspondiente a C=C, se tomó como pico de referencia para conocer la posición de los demás, asignándole el valor de 284,6 eV.

II. 2.2.5. Espectroscopía Micro-Raman

La espectroscopía Raman es de gran utilidad en la caracterización de materiales de carbono. En el tipo de materiales que nos ocupa, la relación de las bandas D y G nos indica el ordenamiento grafítico, ya que la banda G está asociada con el desarrollo de las estructuras sp^2 del carbono mientras que la banda D, banda de defecto, se asocia con los bordes y los defectos de las capas grafénicas.

El equipo utilizado fue un espectrómetro Micro-Raman dispersivo JASCO NRS-5100 equipado con láser verde de 532 nm.

Cabe destacar que los análisis de SEM, HRTEM, TGA, XRD, XPS y Raman fueron realizados en el Centro de Instrumentación Científica de la Universidad de Granada.

II.3. Electro-reducción de oxígeno

El estudio de la reacción de electro-reducción de oxígeno se llevó a cabo en una celda electroquímica convencional de 3 electrodos conectada a un potenciostato multicanal modelo VMP3 EC-Lab de la casa comercial BioLogic Science Instruments.

Se utilizaron como electrodos:

- Electrodo de trabajo (WE): la muestra objeto de estudio soportada sobre un electrodo de disco rotatorio (RDE) con punta de glaxy carbon, modelo Autolab RDE-2 de Metrohm.
- Contraelectrodo (CE): un hilo de Pt.
- Electrodo de referencia (RE): Ag/AgCl (KCl sat.).

Mientras que, como electrolito se utilizó KOH 0.1M.

La preparación y soporte de la muestra se llevó a cabo de la siguiente manera:

5 mg de catalizador se dispersaron en 1 mL de una disolución 1:9 Nafión (5% wt.):agua, esta dispersión se sonicó durante 30 minutos. Luego, 10 μL de dicha dispersión se depositaron en el la superficie del disco rotatorio y se secaron bajo lámpara IR. A continuación se muestra un esquema del proceso:

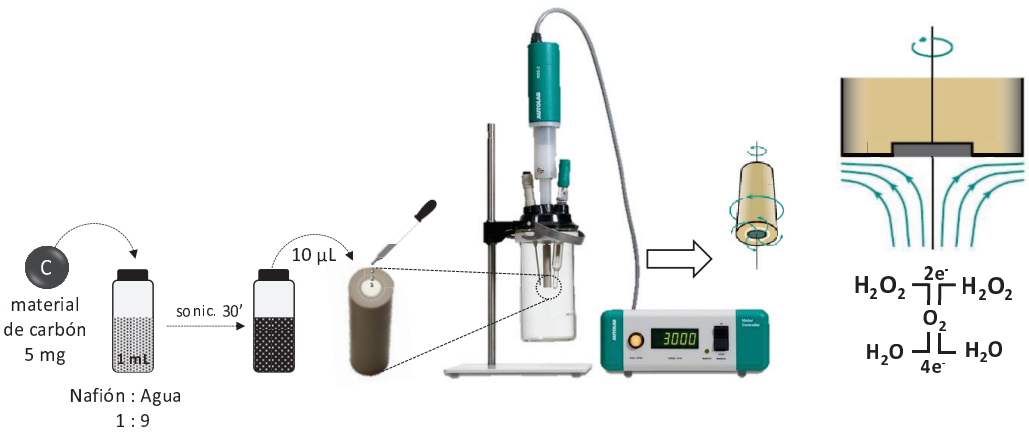

Figura II. 4. Esquema experimental de la electro-reducción de oxígeno (ORR)

Una vez preparado el electrodo de disco rotatorio, de introduce en una disolución electrolítica de KOH 0.1 M. Esta disolución se desairea haciendo burbujear nitrógeno durante 30 minutos, luego, se realiza una voltametría cíclica (CV) desde 0.4 a -0.8 V (vs. Ag/AgCl) con una velocidad de rotación de 1000 rpm con el objetivo de estudiar el comportamiento electroquímico del material en ausencia de oxígeno. Luego, se satura la disolución con O_2 durante 1h y se realiza de nuevo una voltametría cíclica entre 0.4 V y -0.8 V para estudiar y comparar el comportamiento del material en presencia de oxígeno.

Finalmente, se realizan diferentes voltametrías lineales de barrido (LSV) en el mismo intervalo de potenciales pero modificando la velocidad de rotación del electrodo entre 500 rpm- 4000 rpm.

Los datos experimentales obtenidos de las LSV se ajustan a la ecuación de Koutecky-Levich [10] (ec. 2.9) para estudiar el mecanismo de la reacción y así conocer si la electro-reducción de oxígeno se produce por la vía de 2 o 4 electrones.

Ecuación 2.9

$$\frac{1}{j} = \frac{1}{j_k} + \frac{1}{B \cdot \omega^{1/2}}$$

Donde j es la densidad de corriente ($A \cdot cm^{-2}$) y ω es la velocidad de rotación (rpm). Por lo tanto, representando la inversa de J frente la inversa de ω obtenemos una recta de ordenada en el origen j_k^{-1} (densidad de corriente cinética) y pendiente B^{-1} (constante de Levich). Y a partir de esta constante obtendremos el número de electrones, ya que B viene definido por:

Ecuación 2.10

$$B = 0.2nF(D_{O_2})^{2/3}v^{-1/6}C_{o_2}$$

Donde:

n, número de electrones transferido	
F , constante de Faraday (C mol^{-1})	96485
D_{O2} ,coeficiente de difusión del oxígeno (cm^2 s^{-1})	1.90E-05
v, viscosidad cinética (cm^2 s^{-1})	0.01
$C_{O2,}$ concentración de oxígeno (mol cm^{-3})	1.20E-06

II.4. Electro-reducción de CO_2

La electro-reducción de CO_2 se llevó a cabo en una celda electroquímica de 3 electrodos de 300 mL de capacidad conectada a un potenciostato multicanal modelo VMP3. Los electrodos utilizados fueron, el catalizador soportado sobre una lámina de grafito como electrodo de trabajo, y Ag/AgCl y un hilo de Pt como electrodo de referencia y electrodo contador respectivamente, mientras que el electrolito utilizado fue una disolución 0.1 M KHCO3 (150 mL).

En primer lugar se preparó una pasta con el catalizador y un 10% wt. de una suspensión de PTFE (60% wt.) con el objetivo te poder depositarla sobre una lámina de grafito. A continuación, la lámina de grafito dispuesta con el catalizador, se introduce en la disolución electrolítica (previamente saturada de CO_2) y se aplica un potencial continuo de -1.6 V (vs Ag/AgCl). Los hidrocarburos producidos en la fase líquida, viajan a la fase gas de la celda electroquímica y son analizados mediante cromatografía de gases. La fase gas continúa recirculándose (celda-cromatógrafo-celda) durante todo el experimento con ayuda de una bomba de recirculación de gases.

El cromatógrafo de gases (GC) es un Bruker modelo 456-GC equipado con detector FID y columna Chrompack Poraplot Q de 50m x 0.53mm.

La distribución de productos obtenidos se puede expresar en función de la selectividad del carbono a formar un producto específico frente a todos los átomos de carbono convertidos en hidrocarburos. Entonces:

Ecuación 2.10

$$S_{C_i}(\%) = \frac{i \cdot nC_i}{\sum_i i \cdot nC_i} \times 100$$

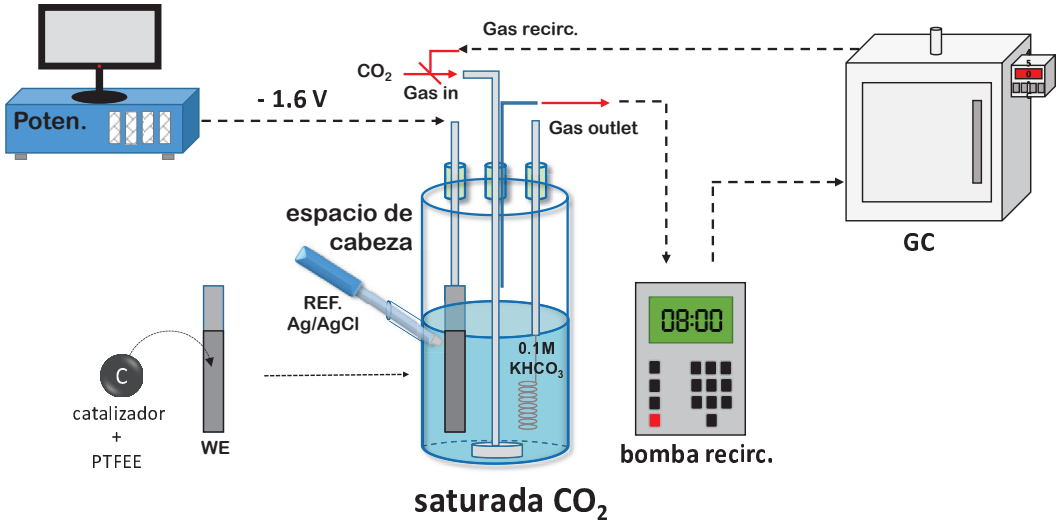

Figura II. 5. Esquema del proceso de electro-reducción de CO_2

II. 4. Bibliografía

[1] W. Stöber, A. Fink, E. Bohn, Controlled growth of monodisperse silica spheres in the micron size range, J. Colloid Interface Sci. 26 (1968) 62–69. doi:10.1016/0021-9797(68)90272-5.

[2] C. Moreno-Castilla, H. García-Rosero, F. Carrasco-Marín, Synthesis and characterization of solid polymer and carbon spheres derived from an emulsion polymerization reaction of different phenolic compounds with formaldehyde, Colloids Surfaces A Physicochem. Eng. Asp. 520 (2017) 488–496. doi:10.1016/j.colsurfa.2017.02.021.

[3] S. Brunauer, P.H. Emmett, E. Teller, Adsorption of gases in multimolecular layers, J. Am. Chem. Soc. 60 (1938) 309–319. doi:10.1021/ja01269a023.

[4] M.M. Dubinin, Inhomogeneous microporous structures of carbonaceous adsorbents, Carbon N. Y. 19 (1981) 321–324. doi:10.1016/0008-6223(81)90079-8.

[5] J.W. Patrick, Porosity in carbons: characterization and applications, Wiley, 1995.

[6] E.P. Barrett, L.G. Joyner, P.P. Halenda, The determination of pore volume and area distributions in porous substances. I. Computations from nitrogen isotherms, J. Am. Chem. Soc. 73 (1951) 373–380. doi:10.1021/ja01145a126.

[7] M.M. Dubinin, Generalization of the theory of volume filling of micropores to nonhomogeneous microporous structures, Carbon N. Y. 23 (1985) 373–380. doi:10.1016/0008-6223(85)90029-6.

[8] L.. Skinner, J.. Sambles, The Kelvin equation—a review, J. Aerosol Sci. 3 (1972) 199–210. doi:10.1016/0021-8502(72)90158-9.

[9] E.W. Washburn, Note on a method of determining the distribution of pore sizes in a porous material, Proc. Natl. Acad. Sci. U. S. A. 7 (1921) 115.

[10] C. Du, Q. Tan, G. Yin, J. Zhang, 5 - Rotating Disk Electrode Method, in: W. Xing, G. Yin, J. Zhang (Eds.), Rotating Electrode Methods Oxyg. Reduct.

Electrocatal., Elsevier, Amsterdam, 2014: pp. 171–198. doi:https://doi.org/10.1016/B978-0-444-63278-4.00005-7.


UNIVERSITAS GRANATENSIS
PLUS ULTRA
1531


UNIVERSITAS · GRANATENSIS
PLUS
ULTRA
· 1531 ·

CAPÍTULO III

METAL-CARBON-CNF COMPOSITES OBTAINED BY CATALYTIC PYROLYSIS OF URBAN PLASTIC RESIDUES AS ELECTRO-CATALYST FOR THE REDUCTION OF CO_2


UNIVERSITAS · GRANATENSIS
PLUS
ULTRA
· 1531 ·

III.1. Introduction

The increase of CO_2 concentration in the atmosphere is thought to be one of the main causes of global climate change [1]. In particular, the CO_2 emission from the use of fossil fuels contributes to the increasing concentration because it establishes a continuous net increase in the natural cycle of the tropospheric carbon.

There are different strategies proposed to control this issue [2] being the most extended the CO_2 storage, and the CO_2 transformation to other valuable products, together with the implementation of renewable energies.

On the other hand, renewable energy sources are supposed to be a replacement, but nowadays they are not producing the constant currents that fossil fuels provide. For this reason, the storage of surplus electrical energy produced during the peak production periods, and its release during peak demand periods, should be crucial. In this manner, extensive research effort has focused on battery storage [3]. However, battery manufacturing requires a lot of resources, reducing their contribution to controlling CO_2 emission, and its life is relatively limited. Furthermore, recycling of their components is also a challenge.

One possible option to address the problem of temporary storing and local surplus of renewable energy is the electro-catalytic reduction of CO_2 to hydrocarbons in water [4]. In this process, the water is split to provide the required hydrogen atoms, which react with CO_2 to form hydrocarbons that can be used directly in the existing infrastructure of fuel transportation as well as in storing the renewable energy.

The direct electrochemical reduction of CO_2 in aqueous solution has been typically studied with metal electrodes like Cu, Au, or Sn during the past few decades [5–10]. Copper electrodes have been found to be quite good in the reduction of CO_2 to hydrocarbons, although the faradaic efficiency was still low as a result of the dissociation of H_2O to H_2 [9]. More recently, metallic electrodes derived from corresponding metal oxides, like

SnO_x, seemed to show promising results in certain catalytic performance for CO_2 reduction [11–13], and only a few transition-metal oxides such as TiO_2, FeO_x and Cu_2O have been reported as potential electro-catalysts for this application [14].

Alternatively, the application of carbon materials in electro-catalytic CO_2 reduction process is a plausible option, which has been tested with platinum catalysts supported on carbon nanotubes, carbon cloth or carbon black [15,16], and even metal-free carbons [17]. Centi et al. [15] showed for the first time the possibility of electro-catalytically converting CO_2 to hydrocarbons with carbon chains >C5, and with product distributions which do not follow the Anderson–Schulz–Flory distribution model typical for Fischer-Tropsch synthesis. Li et al. [17] addressed nanoporous S-doped and S,N-codoped carbons as catalysts for electrochemical reduction CO_2 to CO and CH_4, where the negative charge on the pyridinic nitrogen groups promotes electron–proton transfer to CO_2 leading to COOH* intermediates, which are further reduced to CO.

Carbon gels doped with transition metals have also shown activity in this reaction [18,19]. Although this CO_2 reduction mechanism is still being studied [20], the products obtained in the direct electrochemical reduction of CO_2 to hydrocarbons can achieve several carbon atoms [21]. Regarding the hydrocarbon selectivity, recently [22,23], a high selectivity to C3-hydrocarbons among the detected products has been reported using Co- and Fe-carbon electrodes. Moreover, Fe-carbon electrodes have shown a well-fitted linear correlation between the average crystal sizes of iron and the faradaic efficiencies: the smaller the crystal size, the higher the faradaic efficiency [23].

On the other hand, the large amounts of plastic residue is also a very important environmental problem, and the out-of-control combustion method should not be an option, because it would increase the CO_2 atmospheric and cause other environmental pollution problems [24]. Within

these materials, polyethylene (HDPE or LDPE) based plastic bags represent a significant proportion. There are several propositions for the recycling of plastic waste, as their transformation in fuels [25], the recovering of valuable components [26] of their transformation in carbon-based materials or composites [27]. However, the direct application of carbon-metal composites, obtained from real world plastic waste as CO_2 electro-catalysts have not been reported yet. One important advantage of these composite materials as electro-catalysts compared to other proposed carbon based electro-catalysts is the low cost of the raw material since they can be obtained directly from the plastic waste. Therefore, with this proposal, we are focusing our actions on the CO_2 problem twice, (i) researching in its electro-catalytic transformation to hydrocarbons; and (ii) proposing a way for the transformation of LDPE based residues in valuable products.

In the present work, we demonstrate the application of metal-carbon-carbon nanofibers composites obtained from real world plastic waste as promising electrodes in the electro-catalytic reduction of CO_2 to hydrocarbons.

III.2. Materials and Methods

Three different composites of metal-carbon-carbon nanofibers (-CNF) were prepared by a catalyzed pyrolysis of urban plastic residues which were thermally pre-treated in a closed reactor. These residues were plastic bags that were used in several well-known supermarkets in Spain, in which the polymer composition mainly consisted of low-density polyethylene (LDPE). Firstly, 10 g of the above-mentioned plastic bags were dissolved in 100 mL of o-xylene at 80 °C, and then 2 g of the catalyst precursor was added. The catalyst precursors were the corresponding hydroxides of Fe, Co and Ni, and the resulting mixture was stirred for 4 h. After that, the o-xylene was evaporated, and the solid was heat treated at 350 °C in a closed reactor

(Parr Instrument, Moline, Illinois, USA) (reactor ref. A1828HC2) for four hours. Finally, the so pre-treated solid was pyrolised under N_2 flow (300 mL min^{-1}) at 900 °C. Before the characterization, the composites were washed with cool water several times. The obtained composites were named as PFe, PCo and PNi, being Fe, Co and Ni the pyrolitic catalyst, respectively.

The metal contents of the composites were determined by inductively coupled plasma optical emission spectrometry (ICP-OES) using an ICP-OES PerkinElmer OPTIMA 8300 spectrometer (PerkinElmer, Madrid, Spain).

The samples were texturally characterized by physical adsorption of nitrogen, scanning electron microscopy (SEM), high resolution transmission electron microscopy (HRTEM), and chemically characterized by X-ray diffraction (XRD) and X-ray photoelectron spectroscopy (XPS) and Linear sweep voltammetries (LSV) were also carried out.

N_2 adsorption was carried out at −196 °C. Prior to this measuring process, the samples were outgassed overnight at 110 °C under high vacuum (10^{-6} mbar). The BET equation was applied to the N_2 adsorption data obtaining the apparent surface area, S_{BET}. The Dubinin-Radushkevich (DR) equation was applied to the N_2 adsorption data to obtain the corresponding micropore volume (W_0) and micropore mean width (L_0). Total pore volumes ($V_{0.95}$) were calculated from N_2 adsorption isotherms at −196 °C and at 0.95 relative pressure.

SEM was carried out using a GEMINI-1430-VP scanning electron microscope (Carl Zeiss AG, Oberkochen, Germany), equipped with a secondary electron detector, back-scatter electron detector and by using an X-Max 50 mm energy dispersive X-ray microanalysis system. All the samples were crushed before performing this analysis.

HRTEM was performed using a FEI Titan G2 60–300 microscope (FEI, Eindhoven, The Netherlands) with a high brightness electron gun (X-FEG)

operated at 300 kV and equipped with a Cs image corrector (CEOS), and for analytical electron microscopy (AEM) a SUPER-X silicon-drift window-less EDX detector.

XRD analysis was carried out in a BRUKER D8 ADVANCE diffractometer (BRUKER, Rivas-Vaciamadrid, Spain) using CuKα radiation. JCPDS files were searched to assign the different diffraction lines observed. Diffraction patterns were recorded between 10° and 70° (2θ) with a step of 0.02° and a time per step of 96 s. The average crystal size was determined using the Scherrer equation.

XPS measurements of the metal-carbon-CNF composites were performed using a Rayos-X Kratos Axis Ultra-DLD equipped with a MgKα X-ray source ($h\nu$ = 1253.6 eV) operating at 12 kV and 10 mA and a hemispherical electron analyzer. The obtained binding energy (BE) values were referred to the C_{1s} peak at 284.7 eV. A base pressure of 10^{-9} mbar was maintained during data acquisition. The survey and multi-region spectra were recorded at C_{1s}, O_{1s}, Fe_{2p}, Co_{2p}, Ni_{2p}, K_{2p} and Ca_{2p} photoelectron peaks. Each spectral region was scanned enough times to obtain adequate signal-to-noise ratios. The spectra obtained after the background signal correction were fitted to Lorentzian and Gaussian curves to obtain the number of components, the position of each peak, and the peak areas.

Electro-catalytic reduction of CO_2 to hydrocarbons was carried out in a three-electrode cell, working in batch mode at ambient temperature and pressure. The cell has 300 cm^3 of total capacity. A Biologic VMP multichannel potentiostat (Bio-Logic Spain, Barcelona, Spain) was used to induce and control the electro-catalytic reaction by applying the selected potential differences over the electrodes. A platinum electrode was used as a counter electrode and Ag/AgCl as a reference electrode. The used electrolyte was 150 cm^3 of CO_2-saturated 0.1 M potassium bicarbonate aqueous solution. The setup was used in potentiostatic mode at −1.6 V,

reproducing the voltage conditions of previous works [19]. Prior to the electro-catalytic CO_2 reduction, the liquid phase was saturated through bubbling with CO_2 for 3 h. After saturation, the pH of the solution was 6.7. The CO_2 feed and exit lines were closed off and the reactor was operated in the batch mode. The amount of composite used in the cathode as electro-catalyst (working electrode) was 80 mg which was homogeneously pasted on both faces of a graphite sheet with dimensions of 50 mm × 8 mm. In the preparation of the cathode, the metal-carbon-CNF composite was mixed with the corresponding amount of polytetrafluoroethylene (PTFE) in a weight ratio of (80:7) using a PTFE (60%) water solution. All working electrodes were kept in 0.1 M potassium bicarbonate aqueous solution overnight before being used in the electro-reactor. The samples were also tested as electro-catalysts carrying out the reaction under Ar-saturated solution and, therefore, using electrolytes free of CO_2.

The samples were also characterized by LSV. The cathodic sweep analysis was conducted from the equilibrium electrode potential to negative electric potential of −2.0 V vs. Ag/AgCl, with a scan rate of 5 mVs^{-1}, using the same experimental conditions and reactor set-up for the electro-catalytic reduction of CO_2.

The hydrocarbons produced by the electro-chemical reduction of CO_2 were analyzed from the gas phase using a gas chromatograph (GC) (Bruker Española, Rivas-Vaciamadrid, Spain), where the gases were directly injected into the GC column using a gas recirculating pump for low flows. The GC (carrier gas: He, column: Chrompack Poraplot Q, 50 m × 0.53 mm) was equipped with a FID and TCD detectors. The distribution of gaseous products can be expressed in terms of the carbon selectivity as the amount of carbon atoms (from CO_2) in a specific product relative to the total amount of carbon atoms in the detected hydrocarbons.

$$S_{C_i}(\%) = \frac{i \cdot nC_i}{\sum_i i \cdot nC_i} \times 100$$

Here *nCi* represents the mol of product *Ci*, and i the number of carbon atoms in that product.

The liquid phase was also analyzed by Headspace Gas Chromatography-Mass Spectrometry using another GC equipped with a HP-INNOWax 30 m × 0.25 mm × 0.25 μm column, which was coupled to a MS-Triple quadrupole. The presence of carboxylic acids or alcohols of one to four carbon atoms were not detected.

III.3. Results and Discussion

III.3.1 Textural and Chemical Characterization of the Composites

Table III.1 summarizes the surface areas and pore volumes of the composites. These materials show apparent surface areas between 44 and 80 $m^2\ g^{-1}$, and an extremely low microporosity, in fact, their N_2 adsorption isotherms show typical type IV shapes.

Table 1. Name, surface area and pore volumes of the composites.

Sample	S_{BET} ($m^2\ g^{-1}$)	W_0 ($cm^3\ g^{-1}$)	L_0 (nm)	$V_{0.95}$ ($cm^3\ g^{-1}$)
PFe	44	0.01	2.08	0.100
PCo	80	0.02	2.16	0.189
PNi	44	0.01	2.18	0.149

SEM images of the composites are collected in Figure III.1. The morphology consists in a mixture of carbon particles pseudo-flats, overlapped among them from where carbon-nanofibers (CNF) emerge. These CNF are clearly visible in sample PNi, where they are longer than in the other composites, although by HRTEM (Figure III.2) the presence of CNF has been detected in all the samples being these CNF clearly hollow and maintaining the metal particle inside of them in most cases. Moreover,

the main metal particles Fe, Co or Ni are very well dispersed throughout the carbon matrix (Figure III.2), showing a wide range of sizes but all within the nanometric scale.

Figure III.1. SEM microphotographs showing the morphology of the different composites. Red circles indicate CNF in sample PCo.

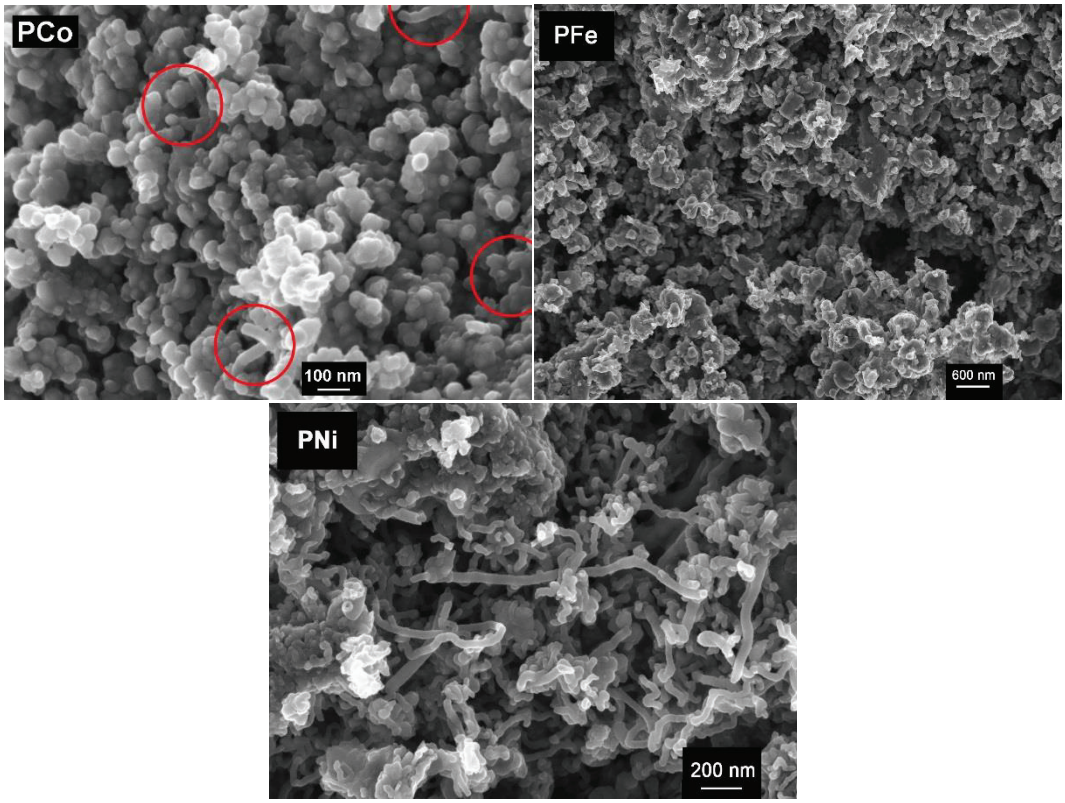

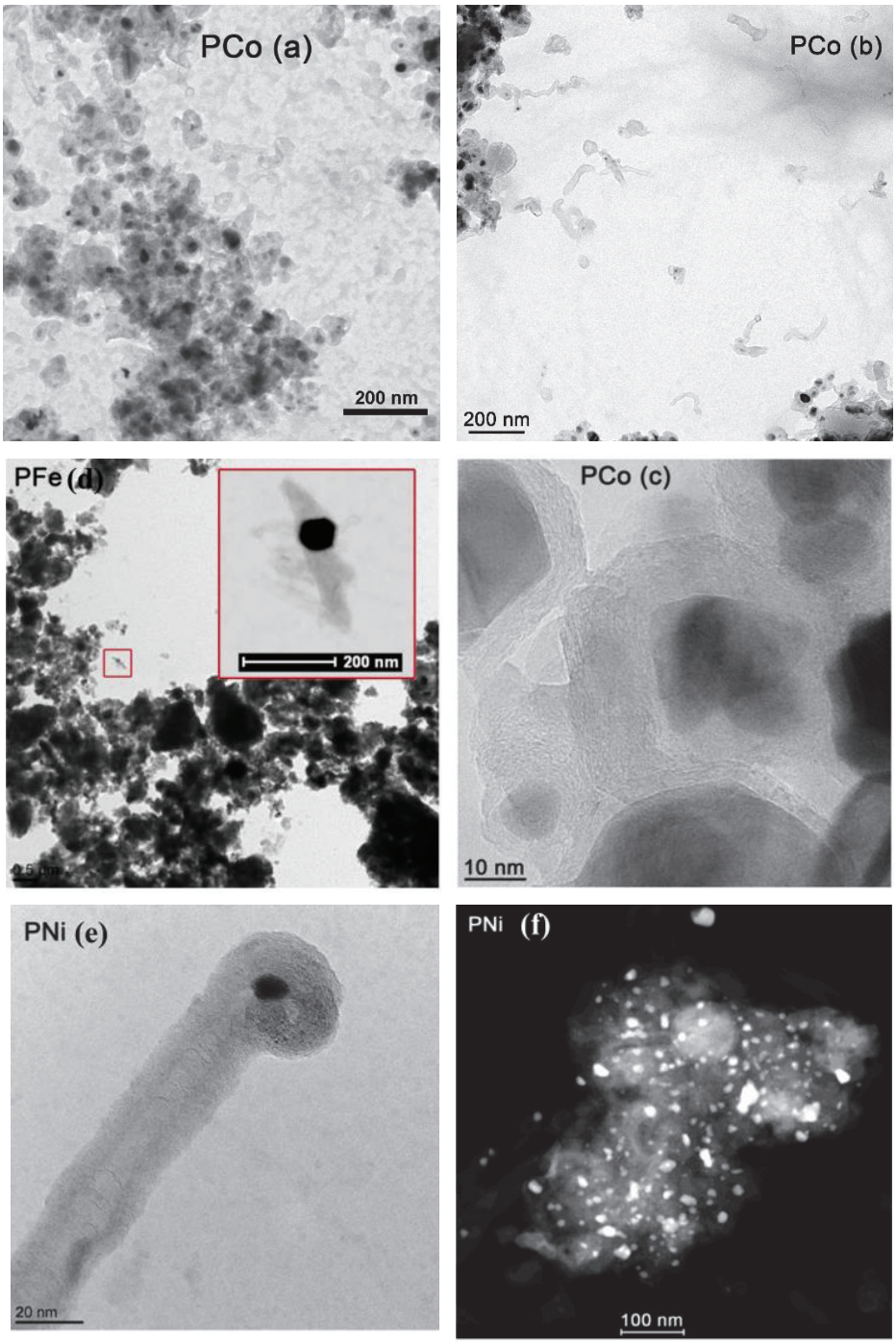

Figure III.2. (**a**–**e**) High-resolution transmission electron microscopy (HRTEM) images of the composites; (**f**) scanning transmission electron microscopy (STEM) image, using a high angle annular dark field (HAADF) detector of the PNi sample.

Regarding the metal chemical composition of the composites, Table III.2 collects the ICP analysis of the samples. Firstly, it is observed that the content of the pyrolitic catalyst is not the same among the composites which denote a different catalytic behavior and, therefore, indicates different yield in carbon phases. In this line, composite PFe shows the highest metal loading, followed by PCo and lastly by PNi. Thus, small amounts of Fe, Co or Ni are present in all the samples which are in agreement with other studies where the metal content of commercial plastic bags have been analyzed [28]. Much more significant are the relatively high contents of Ca and K; these metals are typical additives of the commercial plastic bags to enhance stiffness and mechanical properties [29].

Table III.2. Metal content of the composites determined by inductively coupled plasma optical emission spectrometry (ICP-OES).

Sample	Ca_{ICP} (wt. %)	Co_{ICP} (wt. %)	Fe_{ICP} (wt. %)	K_{ICP} (wt. %)	Ni_{ICP} (wt. %)
PCo	2.31	**9.93**	0.36	2.56	0.12
PFe	3.75	0.07	**15.92**	4.68	0.43
PNi	1.56	0.02	0.29	2.02	**6.52**

On the other site, Fe, Co, and Ni nanoparticles are mainly reduced in zero oxidation state (Figure 3) and situated in both of the carbon phases. This conclusion results from the corresponding XRD peaks that are clearly visible at 44.7°, 44.4° and 44.5° for Fe, Co, and Ni, respectively, while practically negligible amounts of these metals were detected by XPS (Table 3). Moreover, the aforementioned Fe, Co or Ni nanoparticles situated in the amorphous carbon phase are covered by graphitic clusters as it has been observed by HRTEM (Figure 2c), which is due to the fact that these metals are also the catalytic metals of graphitization [30,31].

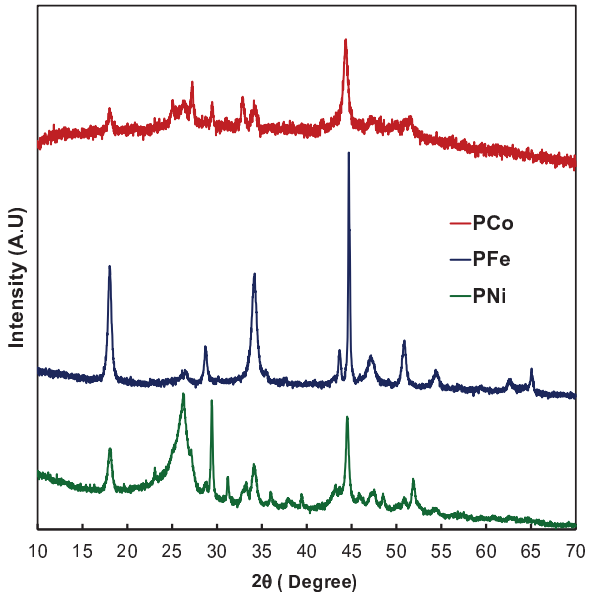

Figure III.3. XRD patterns of the composites.

Table III.3. Superficial chemical content of the composites determined by XPS.

Sample	C (wt. %)	O (wt. %)	K (wt. %)	Ca (wt. %)	Co (wt. %)	Fe (wt. %)	Ni (wt. %)
PCo	87.71	6.93	2.05	2.97	0.34	0.00	0.00
PFe	82.21	8.53	5.35	3.81	0.00	0.10	0.00
PNi	89.84	4.12	3.91	1.98	0.00	0.00	0.15

Nevertheless, the case of Ca and K are very different, also between them: Ca particles are clearly Ca(II) forming part of $Ca(OH)_2$; XRD peaks at 18 and 34° seem to confirm it (Figure III.3) and the $Ca2p_{3/2}$ XPS peak at 348.4 eV as well (Figure III.4). However, K particles have not been detected by XRD, which means that its sizes should be lower than 4 nm approx., however, K(0) peaks have been clearly detected by XPS at 293.7 eV (Figure III.4; only XPS spectra of PNi has been included in this Figure being the corresponding PCo and PFe XPS spectra very similar to this one). A plausible explanation would be that K(0) nanoclusters or atoms could be mainly inserted between the graphenic layers, as it is only in this situation

that they could they keep the zero oxidation state after the final washing treatment of the samples. Finally, it should be noted that both data of chemical analysis, ICP and XPS are in good agreement: PNi is the composite with the lowest transition metal content obtained by ICP analysis and with the highest carbon content determined by XPS, while in the case of PFe, opposites occur. On the other hand, both K and Ca are homogeneously distributed throughout the composite since similar contents are obtained from both techniques.

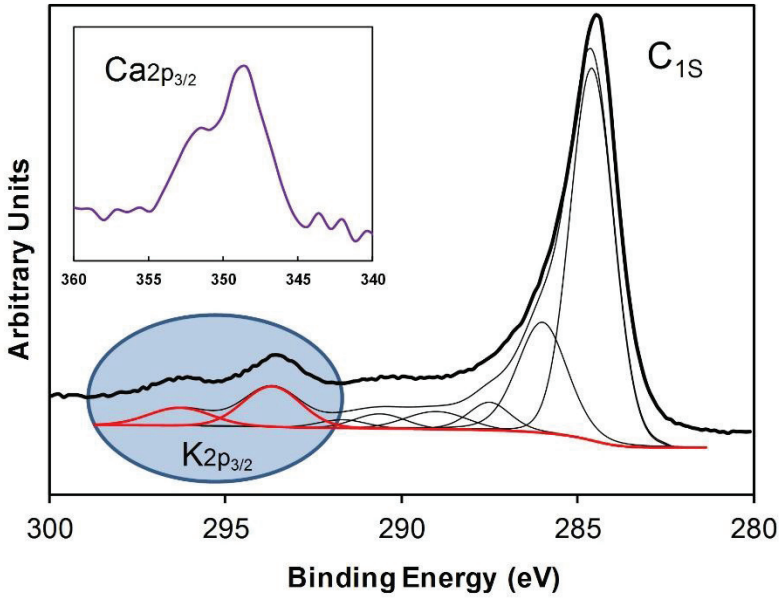

Figure III.4. XPS spectra of composite PNi

III.3.2 Electro-reduction of CO_2

The three composites were used as a cathode in the electro-catalytic reduction of CO_2. A graphite sheet with dimensions of 50 mm × 8 mm was also tested as a blank cathode in the electro-catalytic reduction of CO_2. The products analyzed in the gas phase of the reactor were the following: methane (CH_4), ethane (C_2H_6), ethene (C_2H_4), propane (C_3H_8), propene (C_3H_6), propyne (C_3H_4) and n-butane (C_4H_{10}); Figure III.5 shows the evolution of these compounds vs. the reaction time.

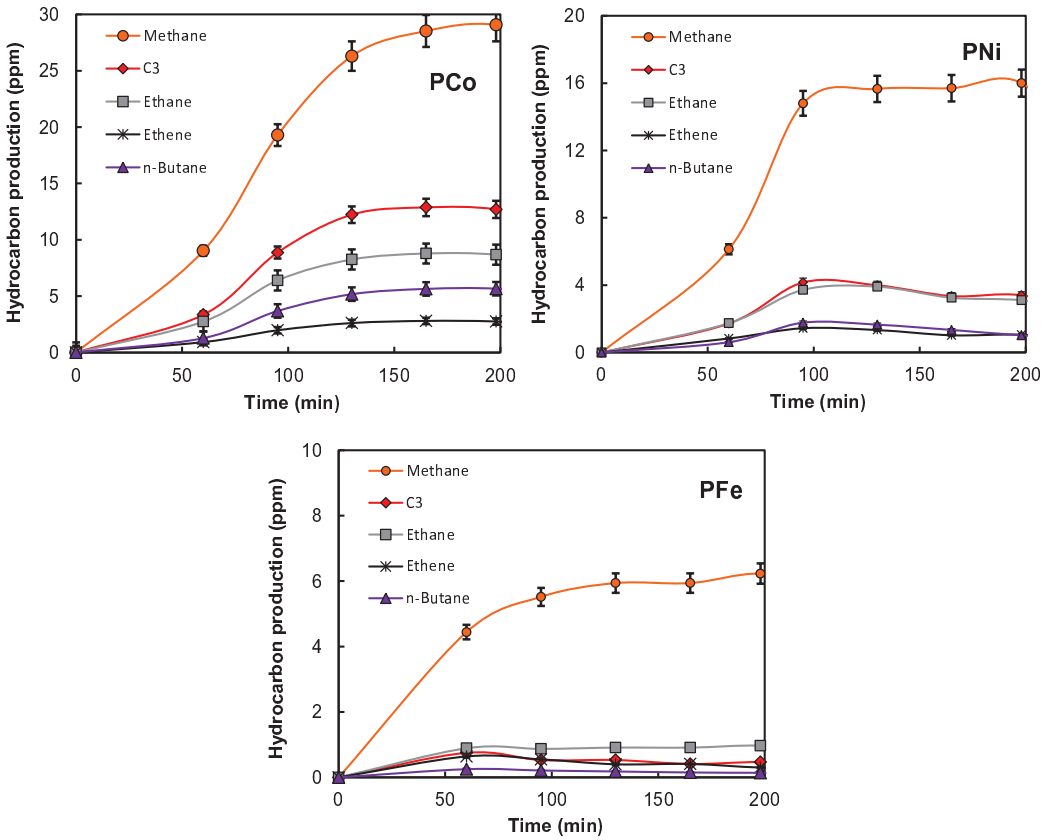

Figure III.5. Product distribution (ppm) vs. reaction time.

The molar production has also been described regarding C1, C2, C3 and C4 hydrocarbons, 1 to 4 being the number of carbon atoms in the molecules to simplify the discussion about the reaction selectivity. Nevertheless, methane was the major product in all of the cases, and minor amounts of other detected products (probably C4 isomers, or C5, hydrocarbons) have not been quantified. Thus, it is necessary to clarify that when an electrolyte free from dissolved CO_2 was used (that is, carrying out the reaction under Ar-saturated solution), hydrocarbons, CO or CO_2 were not detected in any cases. Similarly, in the presence of CO_2 (normal experimental reaction conditions) and using only the pure graphite cathode, no hydrocarbons were detected. Regarding the molar production, although the surface area and pore volume of the composites were relatively low, the

adsorption of a part of the product in the porous structure of the carbon phases could never be ruled out.

Data of the total molar productions of hydrocarbons in the reactor are collected in Figure III.6; from this Figure, an adequate comparison of the electro-catalytic behavior of these composites is not straightforward because they do not present similar textural characteristics or metal contents. On the other side, we can see that the rate of hydrocarbon formation tends to decrease after ~100 min of reaction for PNi and PFe, and somewhat later for PCo. This type of catalytic behavior has been previously observed [22] and explained by a high formation of H_2 and O_2, which can provoke a dilution effect of the hydrocarbon formation in the gas phase of the reactor [32]. In any case, the following catalytic tendency can clearly be observed: PCo > PNi > PFe, which is in accordance with the apparent faradaic efficiencies calculated at 95 min of reaction time (Table III.4). It is important to clarify that that only the detected hydrocarbons (nor H_2 neither O_2 formation) have been included in the faradaic efficiencies calculations. Faradaic efficiencies of this order have been previously obtained with Fe and Co doped carbon gels [22,23].

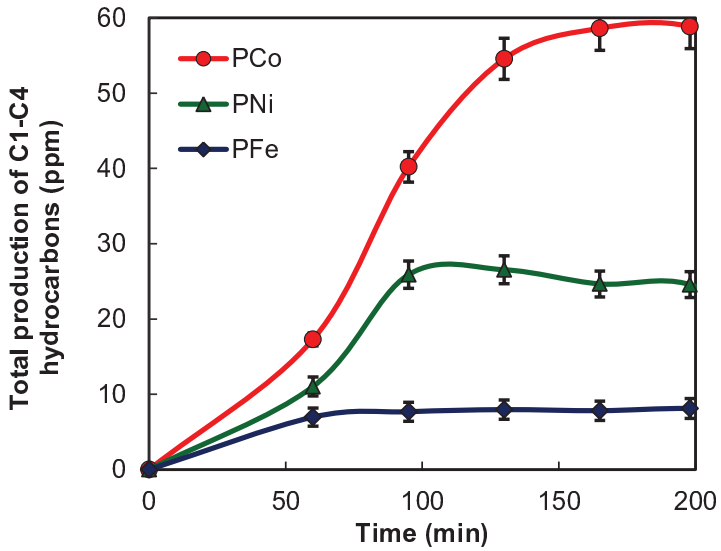

Figure III.6. Molar production vs. time obtained with the electro-catalysts.

Table 4. Mean crystal particle size (d_{XRD}), and apparent faradaic efficiencies (F.E.) for the electro-catalytic CO_2 reduction determined at 95 min of reaction time at −1.6 V vs. Ag/AgCl.

Composite	d_{XRD}* (nm)	F.E. (%)
PCo	13.6	0.46
PNi	20.7	0.40
PFe	39.4	0.06

(*) Co, Ni or Fe, respectively.

Therefore, the current findings demonstrate that all composites work as electro-catalysts in this reaction and that they are able to produce the CO_2 transformation to at least C4 hydrocarbons. Moreover, the composite PCo exhibits high selectivity to C3 products (Figure III.7) within this group of detected products, which is in accordance with a recent finding with another type of Co doped carbon materials [22]. On the other hand, although PNi is mainly selective to CH_4, the amount of C3 produced was also higher than C2. Finally, composite PFe was the least active catalyst, and it was also least selective to long chain hydrocarbons, despite it having the highest metal loading (Table III.2). As previously reported, this behavior is most likely due to its large mean crystal size of Fe (Table III.4) [23]. In this line, it should be noted that this composite has a mean metal particle size much larger than the other samples. Figure III.8 compares the LSV curves of CO_2 reduction obtained with all the electro-catalysts. The strong increase of the current values at −1.6 V of the composite PFe denotes a low electro-catalytic capacity of this cathode in comparison with the other two samples.

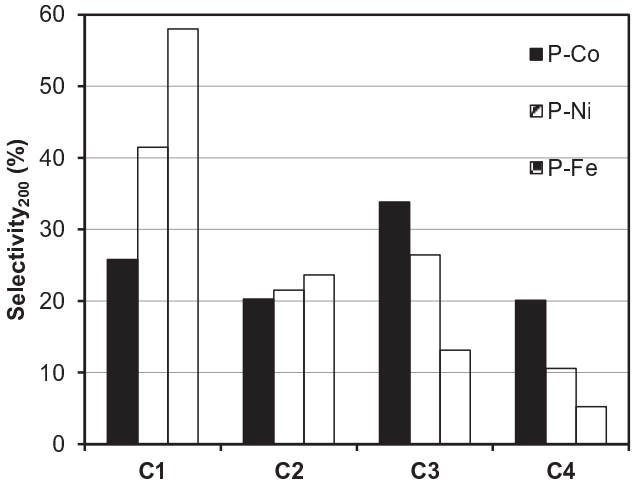

Figure III.7. Product distribution (%) in terms of carbon selectivity in gas phase products after 200 min of reaction time.

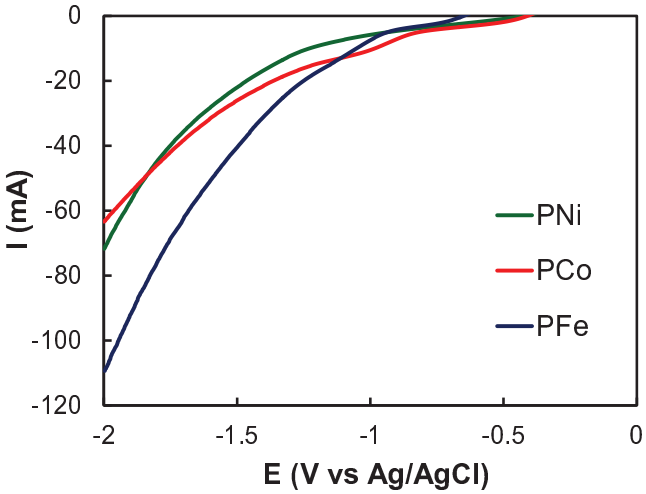

Figure III.8. Linear sweep voltammetries obtained from the equilibrium electrode potential to a negative electric potential of −2.00 V vs. Ag/AgCl. Scan rate: 5 mV/s. Fresh electrodes in CO_2 saturated 0.1 M $KHCO_3$.

III.4. Conclusions

Metal-carbon-CNF composites have been obtained from the urban plastic waste. The amount and type of carbon nanofibers and final carbon contents depend on the pyrolitic used metal: Fe, Co or Ni. Ni catalysts yield the major amount of CNF and carbon phases in the composites. On the other hand, significant contents of Ca and K are also present in the composites, however, while Ca is forming part of $Ca(OH)_2$, K atoms could be embedded inside the carbon phases as K metallic. The composites have been tested as electro-catalyst in the CO_2 reduction to hydrocarbons, and all of them promoted the formation of C1 to C4 hydrocarbons with different activity: PCo > PNi > PFe, which is in accordance with the apparent faradaic efficiencies. It should be highlighted that PCo shows high selectivity to C3 products within this group of compounds.

III.5. References

[1] International Energy Agency, (n.d.). https://www.iea.org/ (accessed 30 March 2019).

[2] BP-Energy economics, Statistical Review of World Energy, (n.d.). https://www.bp.com/en/global/corporate/energy-economics/statistical-review-of-world-energy.html (accessed 31 March 2019).

[3] K.J. Stevenson, The origin, development, and future of the lithium-ion battery, J. Solid State Electrochem. 16 (2012) 2017–2018. doi:10.1007/s10008-012-1745-0.

[4] M. Bevilacqua, J. Filippi, H.A. Miller, F. Vizza, Recent Technological Progress in CO2 Electroreduction to Fuels and Energy Carriers in Aqueous Environments, Energy Technol. 3 (2015) 197–210. doi:doi:10.1002/ente.201402166.

[5] Y. Hori, A. Murata, Electrochemical evidence of intermediate formation of adsorbed CO in cathodic reduction of CO2 at a nickel electrode, Electrochim. Acta. 35 (1990) 1777–1780. doi:10.1016/0013-4686(90)87078-G.

[6] Y. Hori, A. Murata, R. Takahashi, Formation of hydrocarbons in the electrochemical reduction of carbon dioxide at a copper electrode in aqueous solution, J. Chem. Soc. Faraday Trans. 1 Phys. Chem. Condens. Phases. 85 (1989) 2309–2326. doi:10.1039/F19898502309.

[7] Y. Hori, H. Wakebe, T. Tsukamoto, O. Koga, Electrocatalytic process of CO selectivity in electrochemical reduction of CO2 at metal electrodes in aqueous media, Electrochim. Acta. 39 (1994) 1833–1839. doi:10.1016/0013-4686(94)85172-7.

[8] M. Jitaru, D.A. Lowy, M. Toma, B.C. Toma, L. Oniciu, Electrochemical reduction of carbon dioxide on flat metallic cathodes, J. Appl. Electrochem. 27 (1997) 875–889. doi:10.1023/A:1018441316386.

[9] M. Gattrell, N. Gupta, A. Co, A review of the aqueous electrochemical reduction of CO2 to hydrocarbons at copper, J. Electroanal. Chem. 594 (2006) 1–19.

[10] R.P.S. Chaplin, A.A. Wragg, Effects of process conditions and electrode material on reaction pathways for carbon dioxide electroreduction with particular reference to formate formation, J. Appl. Electrochem. 33 (2003) 1107–1123. doi:10.1023/B:JACH.0000004018.57792.b8.

[11] R. Zhang, W. Lv, G. Li, L. Lei, Electrochemical reduction of CO2 on SnO2/nitrogen-doped multiwalled carbon nanotubes composites in KHCO3 aqueous solution, Mater. Lett. 141 (2015) 63–66. doi:10.1016/J.MATLET.2014.11.040.

[12] F. Li, L. Chen, G.P. Knowles, D.R. MacFarlane, J. Zhang, Hierarchical mesoporous SnO2 nanosheets on carbon cloth: a robust and flexible electrocatalyst for CO2 reduction with high efficiency and selectivity, Angew. Chemie Int. Ed. 56 (2017) 505–509. doi:10.1002/anie.201608279.

[13] S. Bashir, S.S. Hossain, S. ur Rahman, S. Ahmed, Amir Al-Ahmed, M.M. Hossain, Electrocatalytic reduction of carbon dioxide on SnO2/MWCNT in aqueous electrolyte solution, J. CO2 Util. 16 (2016) 346–353. doi:10.1016/J.JCOU.2016.09.002.

[14] D.D. Zhu, J.L. Liu, S.Z. Qiao, Recent Advances in Inorganic Heterogeneous Electrocatalysts for Reduction of Carbon Dioxide, Adv. Mater. 28 (2016) 3423–3452. doi:10.1002/adma.201504766.

[15] G. Centi, S. Perathoner, G. Winè, M. Gangeri, Electrocatalytic conversion of CO2 to long carbon-chain hydrocarbons, Green Chem. 9 (2007) 671–678. doi:10.1039/b615275a.

[16] G. Centi, Problems and perspectives in nanostructured carbon-based electrodes for clean and sustainable energy, Catal. Today. 150 (2010) 151–162. doi:10.1016/J.CATTOD.2009.09.009.

[17] W. Li, M. Seredych, E. Rodríguez-Castellón, T.J. Bandosz, Metal-free Nanoporous Carbon as a Catalyst for Electrochemical Reduction of CO2 to CO and CH4, ChemSusChem. 9 (2016) 606–616. doi:10.1002/cssc.201501575.

[18] A.F. Pérez-Cadenas, C. Moreno-Castilla, F. Carrasco-Marín, F.J. Maldonado-Hódar, S. Morales-Torres, F. Kapteijn, C.H. Ros, DOPED CARBON MATERIAL FOR THE ELECTROCATALYTIC CONVERSION OF CO2 INTO HYDROCARBONS, USES OF THE MATERIAL AND CONVERSION METHOD USING SAID MATERIAL, WO/2013/004882, n.d.

[19] A.F. Pérez-Cadenas, C.H. Ros, S. Morales-Torres, M. Pérez-Cadenas, P.J. Kooyman, C. Moreno-Castilla, F. Kapteijn, Metal-doped carbon xerogels for the electro-catalytic conversion of CO2 to hydrocarbons, Carbon N. Y. 56 (2013) 324–331. doi:10.1016/J.CARBON.2013.01.019.

[20] K.J.P. Schouten, Y. Kwon, C.J.M. van der Ham, Z. Qin, M.T.M. Koper, A new mechanism for the selectivity to C1 and C2 species in the electrochemical reduction of carbon dioxide on copper electrodes, Chem. Sci. 2 (2011) 1902–1909. doi:10.1039/C1SC00277E.

[21] J. Qiao, Y. Liu, F. Hong, J. Zhang, A review of catalysts for the electroreduction of carbon dioxide to produce low-carbon fuels, Chem. Soc. Rev. 43 (2014) 631–675. doi:10.1039/c3cs60323g.

[22] A. Abdelwahab, J. Castelo-Quibén, M. Pérez-Cadenas, A. Elmouwahidi, F. Maldonado-Hódar, F. Carrasco-Marín, A. Pérez-Cadenas, Cobalt-Doped Carbon Gels as Electro-Catalysts for the Reduction of CO2 to Hydrocarbons, Catalysts. 7 (2017) 25. doi:10.3390/catal7010025.

[23] J. Castelo-Quibén, A. Abdelwahab, M. Pérez-Cadenas, S. Morales-Torres, F.J. Maldonado-Hódar, F. Carrasco-Marín, A.F. Pérez-Cadenas, Carbon - iron electro-catalysts for CO2 reduction. The role of the iron particle size, J. CO2 Util. 24 (2018) 240–249. doi:10.1016/j.jcou.2018.01.007.

[24] M.A. Keane, Catalytic transformation of waste polymers to fuel oil, ChemSusChem Chem. Sustain. Energy Mater. 2 (2009) 207–214. doi:10.1002/cssc.200900001.

[25] J. Aguado, D.P. Serrano, G. San Miguel, M.C. Castro, S. Madrid, Feedstock recycling of polyethylene in a two-step thermo-catalytic reaction system, J. Anal. Appl. Pyrolysis. 79 (2007) 415–423. doi:10.1016/j.jaap.2006.11.008.

[26] P. Quicker, Thermal treatment as a chance for material recovery, in: Source Sep. Recycl., Springer, 2017: pp. 119–149. doi:10.1007/698_2017_28.

[27] A. Bazargan, G. McKay, A review–synthesis of carbon nanotubes from plastic wastes, Chem. Eng. J. 195 (2012) 377–391. doi:10.1016/j.cej.2012.03.077.

[28] O. Huerta-Pujol, M. Soliva, F. Giró, M. López, Heavy metal content in rubbish bags used for separate collection of biowaste, Waste Manag. 30 (2010) 1450–1456. doi:10.1016/J.WASMAN.2010.03.023.

[29] K. Yang, Q. Yang, G. Li, Y. Sun, D. Feng, Morphology and mechanical properties of polypropylene/calcium carbonate nanocomposites, Mater. Lett. 60 (2006) 805–809. doi:10.1016/j.matlet.2005.10.020.

[30] F.J. Maldonado-Hódar, C. Moreno-Castilla, J. Rivera-Utrilla, Y. Hanzawa, Y. Yamada, Catalytic Graphitization of Carbon Aerogels by Transition

Metals, Langmuir. 16 (2000) 4367–4373. doi:10.1021/la991080r.

[31] F.J. Maldonado-Hódar, C. Moreno-Castilla, A.F. Pérez-Cadenas, Surface morphology, metal dispersion, and pore texture of transition metal-doped monolithic carbon aerogels and steam-activated derivatives, Microporous Mesoporous Mater. 69 (2004) 119–125. doi:https://doi.org/10.1016/j.micromeso.2004.02.001.

[32] M.R. Gonçalves, A. Gomes, J. Condeço, R. Fernandes, T. Pardal, C.A.C. Sequeira, J.B. Branco, Selective electrochemical conversion of CO2 to C2 hydrocarbons, Energy Convers. Manag. 51 (2010) 30–32. doi:10.1016/j.enconman.2009.08.002.


UNIVERSITAS · GRANATENSIS
PLUS
ULTRA
· 1531 ·

CAPÍTULO IV

FROM POLYETHYLENE TO HIGHLY GRAPHITIC AND MAGNETIC CARBON SPHERES NANOCOMPOSITES:

CARBONIZATION UNDER PRESSURE


UNIVERSITAS · GRANATENSIS
PLUS
ULTRA
· 1531 ·

nanomaterials

MDPI

Communication

From Polyethylene to Highly Graphitic and Magnetic Carbon Spheres Nanocomposites: Carbonization under Pressure

Jesica Castelo-Quibén *, Luisa M. Pastrana-Martínez, Francisco Carrasco-Marín and Agustín F. Pérez-Cadenas

Carbon Materials Research Group, Department of Inorganic Chemistry, Faculty of Sciences, University of Granada, Campus Fuentenueva s/n, ES18071-Granada, Spain; lpastrana@ugr.es (L.M.P.-M.); fmarin@ugr.es (F.C.-M.); afperez@ugr.es (A.F.P.-C.)

* Correspondence: jesicacastelo@ugr.es; Tel.: +34-958-243-235

Received: 1 March 2019; Accepted: 5 April 2019; Published: 12 April 2019

check for updates

Abstract: Carbon nanocomposites microspheres were synthesized from Low-Density Polyethylene (LDPE) by a facile one-step strategy under solvent-free conditions. The synthesis of these materials was carried out in a closed Hastelloy® reactor at 700 °C. The treatment, during which autogenic pressure was generated, leads to highly graphitic materials with stunning properties, particularly concerning the oxidation resistance (compared to the graphite stability). The metallic doping triggers the growth of nanostructures with diverse morphologies around the spheres, obtaining samples with magnetic properties.

Keywords: carbon microspheres; metal-carbon nanocomposites; magnetic composites

*Article published in Nanomaterials, 2019, **9** (4), 606; doi: 10.3390/nano9040606*

Abstract: Carbon nanocomposites microspheres were synthesized from Low-Density Polyethylene (LDPE) by a facile one-step strategy under solvent-free conditions. The synthesis of these materials was carried out in a closed Hastelloy® reactor at 700 °C. The treatment, during which autogenic pressure was generated, leads to highly graphitic materials with stunning properties, particularly concerning the oxidation resistance (compared to the graphite stability). The metallic doping triggers the growth of nanostructures with diverse morphologies around the spheres, obtaining samples with magnetic properties.

Keywords: carbon microspheres; metal-carbon nanocomposites; magnetic composites

IV.1 Introduction

Carbon materials are excellent candidates to be used in a wide range of applications thanks to their great textural, mechanical, thermal and electrical properties. Moreover, the versatility of carbon materials facilitates the possibility of modifying on demand their textural, chemical and electrical properties by tuning the carbon precursor as well as by doping the carbon already prepared in accordance with the required applications [1–4]. Furthermore, due to their chemical stability, the processes can be carried out even if operating conditions are too severe: for example, gas adsorption at a high temperature and pressure or electrochemical applications in an acid or basic medium [5–10].

Carbon spheres (CS) are very promising nanostructures in several applications [11–14]. The spheres can be obtained by different synthesis procedures and methods such as an arc-discharge process, chemical vapour deposition, autoclave methodologies (hydrothermal, solvothermal or by using supercritical fluids) or template methods. Also, several compounds are used as a source of carbon, and among the most commonly used are: resorcinol-formaldehyde (and its derivatives), saccharides or organic acids [15]. Furthermore, the spherical shape allows the entire surface area to be effectively exposed beside the high packing density, which is very important for energy applications [16]. Nevertheless, the synthesis process of CS is usually tedious, and a low amount of material is normally obtained, which makes it an expensive process.

During the last few decades, governments and companies have been making a great effort to improve the current environmental situation. In the research field, one of the strategies involves recycling wastes to obtain advanced materials [17–19]. On this subject, the world plastic production almost reached 350 million tonnes in 2017. In 2016, only 8.4 million tonnes of plastic waste were collected in order to be recycled inside and outside the EU [20]. Moreover, 17.5% of total plastic production corresponds to

Low-Density Polyethylene (LDPE), which is the main compound in plastic bags, trays, containers and agricultural films.

Previous works have investigated the pyrolysis of different polymers into a closed reactor obtaining carbon spherules [21,22]. However, they did not succeed in obtaining highly graphitic materials, nor have they studied the influence of adding metals.

Taking this data into consideration, we have in the present work prepared carbon microspheres from LDPE (solvent free and under autogenic pressure) through a facile one-step method, which implies a high carbon yield and contributes to the development of graphitic clusters, whereby the conductivity of the material is improved. At the same time, the influence of metal doping on the physical and chemical properties of CS has been also reported.

To our knowledge, there has not been any previous reporting of the synthesis of highly graphitic and magnetic CS nanocomposites prepared in similar conditions.

IV.2. Materials and Methods

Three different carbon spheres (CS)-metal composites were obtained by pyrolysis of Low Density Polyethylene (LDPE) (supplied by Sigma-Aldrich) catalyzed by the metal salts $Fe(C_2H_3O_2)_2$, $Co(C_2H_3O_2)_2$ or $Ni(C_2H_3O_2)_2$. Additionally, a metal-free material was obtained under the same experimental conditions for comparative purposes. The samples thus obtained were labelled as PE-Fe, PE-Co, PE-Ni and PE respectively. First, 0.5 *g* of LDPE was placed and treated at 700 °C into a closed hand-made Hastelloy® reactor of 25 mL capacity. The heating rate was 10 °C/min with a dwell time of 2 h at the target temperature. The yield percentage of this synthesis was used to calculate the amount of the corresponding metal precursor to obtain CS-metal composites doped with 10 wt.% of metal.

The amount of metal was determined by a thermogravimetric analysis (TGA), taking into account that the ash percentage corresponds to the metal oxide. TGA was carried in the air with a heating rate of 10 °C/min to 900 °C/min using a Mettler-Toledo TGA/DSC1 thermogravimetric analyzer.

The texture and morphology of the samples were analyzed by scanning electron microscopy (SEM), using a FEI microscope model Quanta 400 and High-resolution transmission electron microscopy (HRTEM) was performed using a FEI Titan G2 microscope.

The crystalline phases of the obtained materials were analysed by Bruker D8 Venture X-ray diffractometer (BRUKER, Rivas-Vaciamadrid, Madrid, Spain).

Raman spectra were recorded using a Micro-Raman JASCO NRS-5100 dispersive spectrophotometer with a 532 nm laser line.

IV.3. Results and Discussion

The schematic diagram outlining the synthesis of the carbon microspheres is illustrated in Figure IV.1.

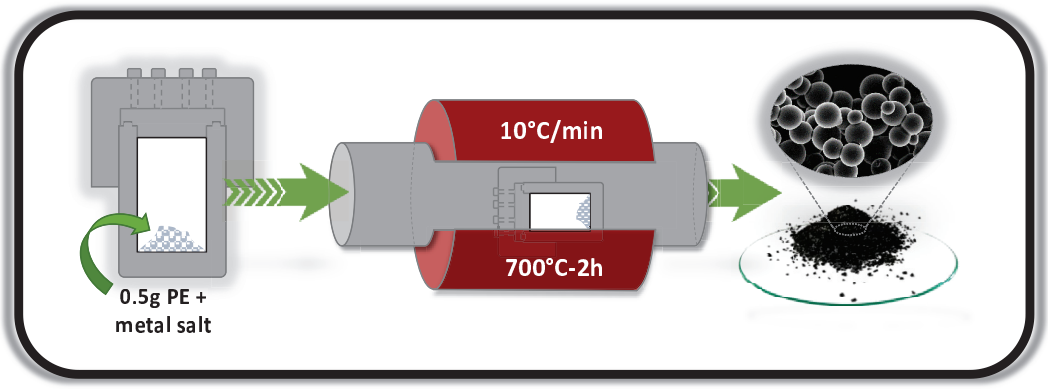

Figure IV.1. Experimental scheme of the synthesis process.

The CS-metal composites that were obtained were labelled as PE-X, where "X" stands for the corresponding metallic precursor salt. For a

comparison, a metal-free CS material (PE) was prepared under the same experimental conditions. The metal contents for PE-Fe, PE-Co and PE-Ni were 3.0, 7.8 and 6.6 wt.%, respectively.

Figures IV.2 and IV.3 illustrate the representative SEM and HRTEM images of PE, PE-Fe, PE-Co and PE-Ni. The images reveal the presence of CS in all cases. The pyrolysis of polyethylene under the experimental conditions of temperature (700 °C) and pressure (~70 bar generated in-situ) results in smooth carbon microspheres that are highly homogeneous in size and shape, whereas the presence of metal provokes the development of carbon nanofibers on the spheres-composites which are especially small in the case of the CS prepared with the iron precursor (PE-Fe). The presence of cobalt in the spheres (PE-Co) causes the growth of carbon nanofibers that are significantly longer than the ones obtained using an iron precursor. On the other hand, almost no microspheres remain in the presence of nickel; instead, graphitic nanostructures emerge.

The TEM images (Figure IV.3) illustrate in detail the graphitization effect on the samples. Figure IV.3a,b shows quite thick carbon spheres which prevent the penetration of electron beams through them; however, it can be clearly observed that PE also features a graphitic order. The above-mentioned catalytic effect of metal doping is also evidenced by TEM, whilst small carbon nanofibers (CNFs) are surrounding the microspheres in PE-Fe, and the cobalt has further catalyzed the CNFs. On the other hand, Figure IV.3d reveals Ni nanoparticles embedded on the graphitic cluster. It should also be noted that the metal phase is highly dispersed throughout the carbon matrix with a small particle size.

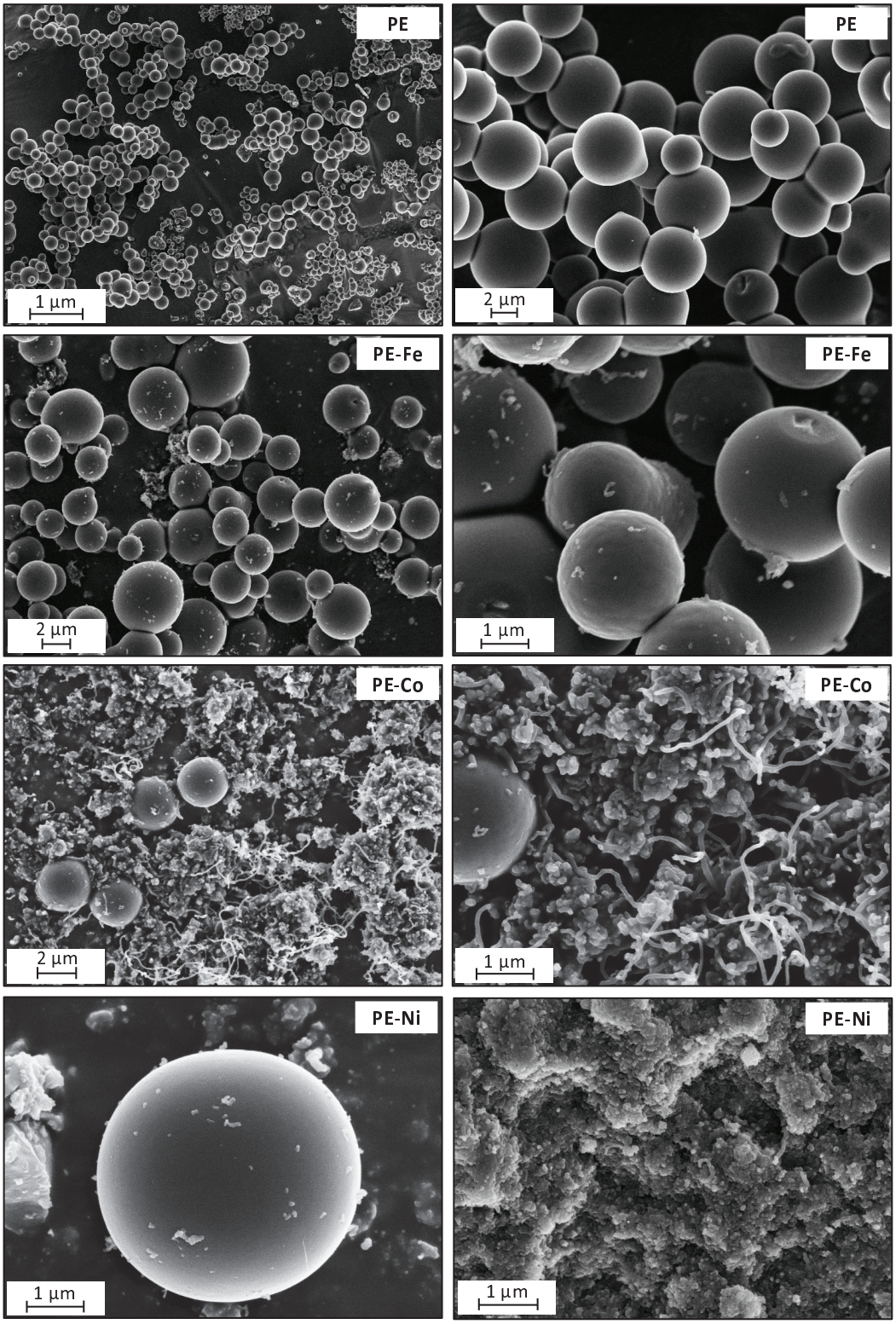

Figure IV.2. SEM images of carbon spheres nanocomposites at different magnifications.

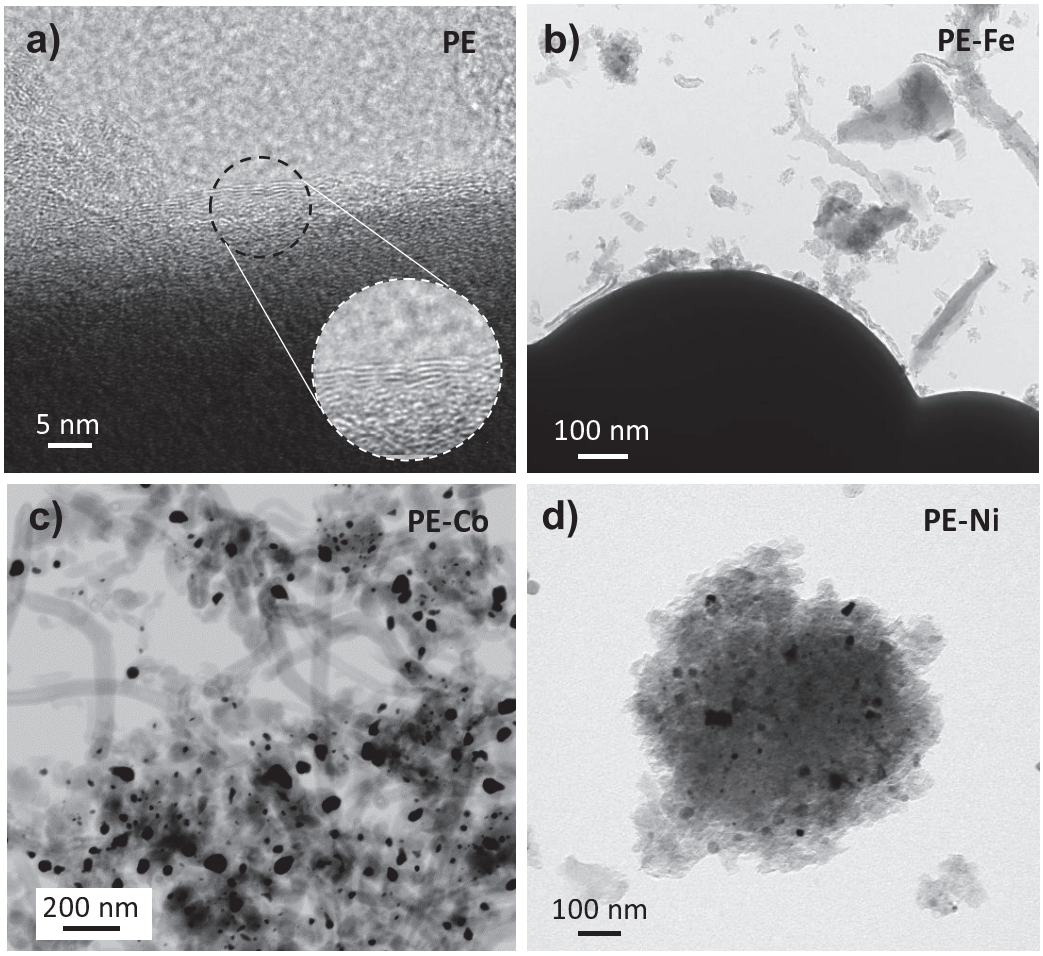

Figure IV.3. (**a**–**d**) TEM and HRTEM images.

The spherical shape of these materials could be attributed to the generated pressure during the pyrolysis process. This statement is based on our previous studies related to plastic waste pyrolyzed into an open reactor, where the presence of carbon microspheres was not found [18].

The sphere size distribution was measured just in those cases where there was a representative statistical population. The obtained histograms are depicted in Figure IV.4. PE shows a broader distribution than PE-Fe or PE-Co, which is centered on 4.5 μm; however, not only the distribution is narrower for the PE-metal samples; additionally, it is centered on a smaller size. Therefore, the presence of metal catalyzes more homogeneous spheres in terms of size, and furthermore these spheres are smaller; such

an effect is slightly accentuated in the case of Co, maybe due to the higher metal content.

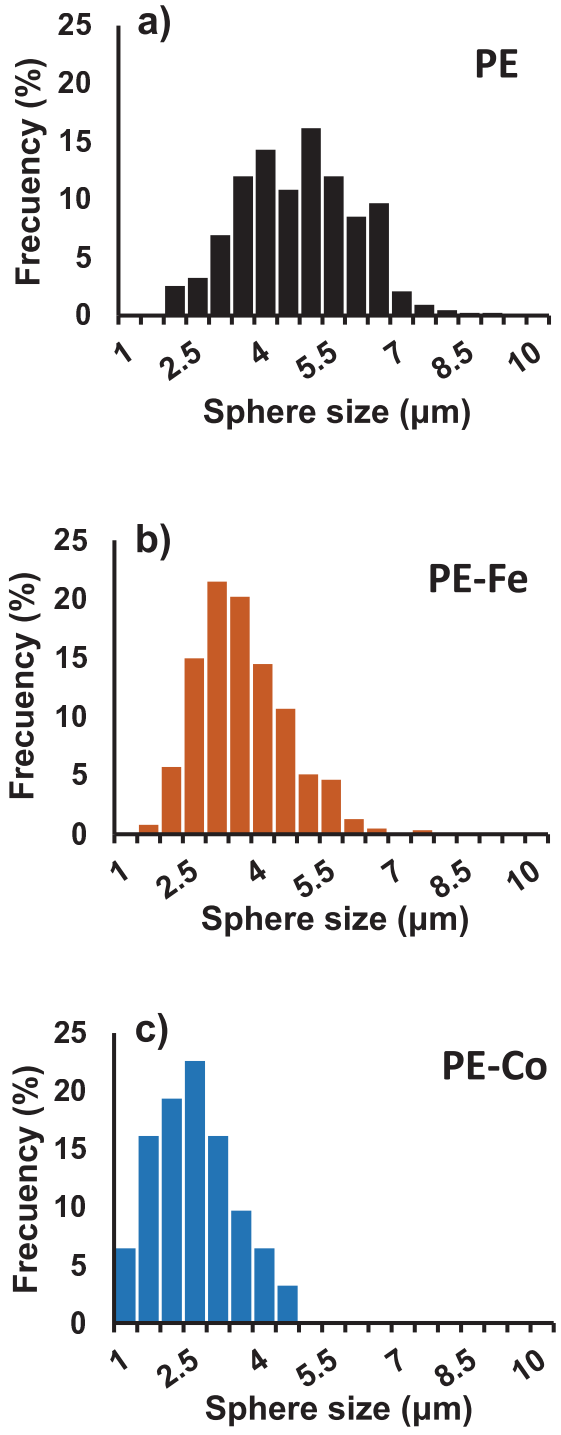

Figure IV.4. (**a**–**c**) Sphere size distribution.

The presence of graphitic domains in the prepared samples is evidenced by X-ray powder diffraction (XRD) and Raman Spectroscopy (Figure IV.5a,b respectively). All materials show graphitic structures, especially in the case of PE, in which no metal catalyst of graphitization was added, indicating the effect of the generated pressure once again.

The XRD pattern (Figure IV.5a) shows the typical diffraction peaks of graphitic crystals at 2θ values around 26° and 44.5°, consistent with the JCPDS card 89-8487. The peaks are intense and well defined, indicating a high crystallinity for all of the samples. The carbon matrix maintains Ni and Co in a 0 oxidation state according to the JCPDS cards 04-0850 (Ni fcc), 15-0806 (Co fcc) and 05-0727 (Co hcp). However, no metallic Fe diffraction peak is observed in the XRD patterns, and this fact, coupled with the Raman results (no iron oxide signal was obtained either), leads us to believe that the Fe(0) crystals could have a mean size that is too small or a very slim laminar shape, as a result of which the ultra-small crystal size is below the XRD detection limit [23].

On the other hand, metal-free carbon microspheres (PE) present the highest ordering level, pointed out by an intense and well-defined G band (which is associated with the development of the sp2 carbon structure), and in particular by the small ratio ID/IG, since the D band is an indicator of disorder [24,25]. The intensity ratio ID/IG increases significantly for PE-Co and PE-Ni. These samples are the ones that have grown further graphitic structures as fibers or clusters, so they have also developed a large number of graphenic edges, which belong to the group of defects responsible for the increment of the D band [26]. These data also demonstrate that the samples are endowed with a high electrical conductivity since such a conductivity is improved with the development of sp2 hybridized carbon fractions, which contribute to the G band in Raman spectra. According to the literature, the lower the intensity ratio of the D/G bands, the higher the electronic conductivity [27,28].

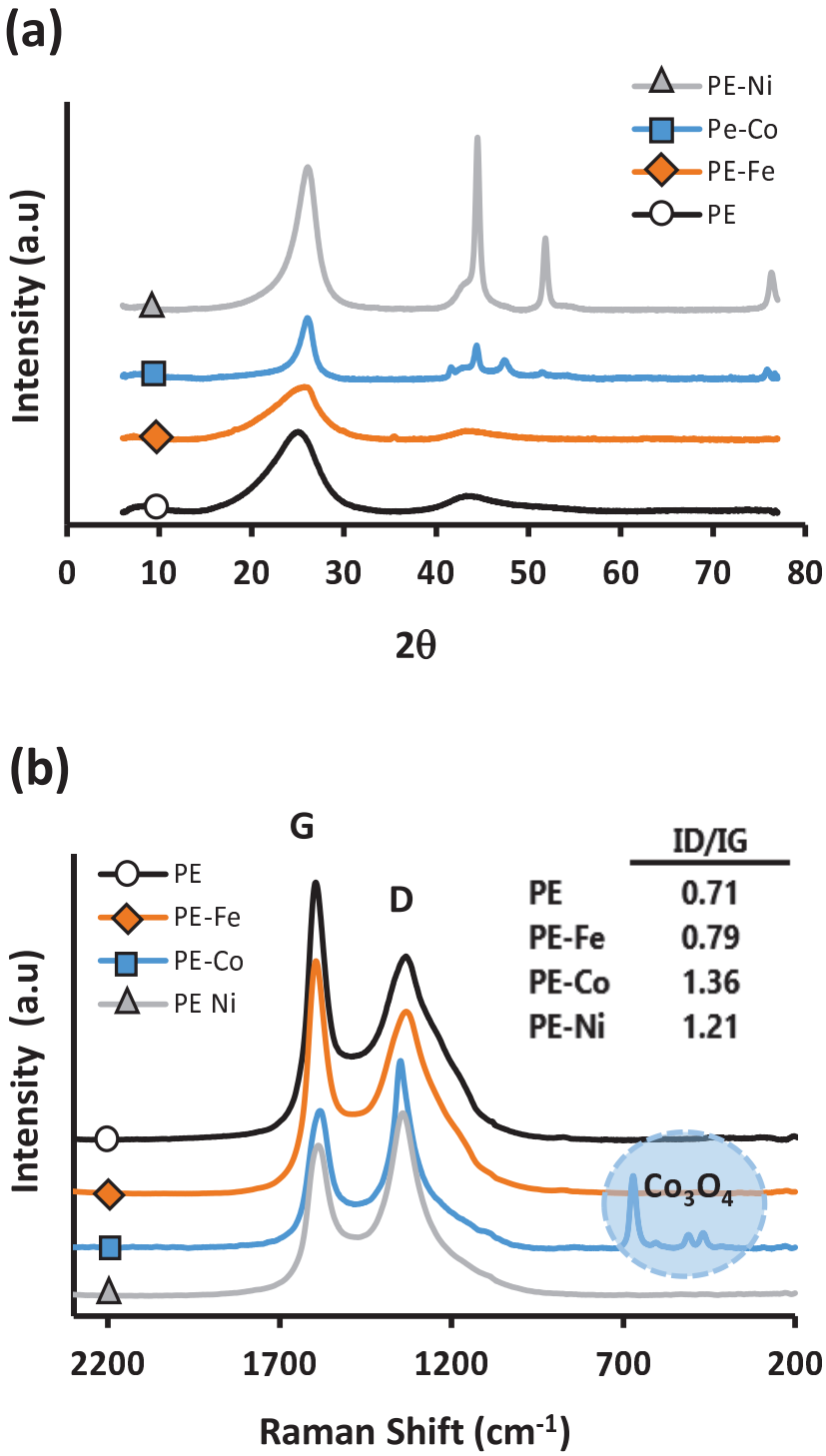

Figure IV.5. (**a**) XRD patterns (**b**) and Raman spectra.

The thermogravimetric analysis (TGA) under air atmosphere (Figure IV.6) manifests an extraordinary thermal stability for PE-Fe, PE-Ni and especially for PE; all of which remain completely stable until 579, 578 and 615 °C, respectively; those temperatures are comparable to that of graphite [29]. This fact supports the highly ordered graphitic structure mentioned above, since the higher the ordering, the better the thermal stability.

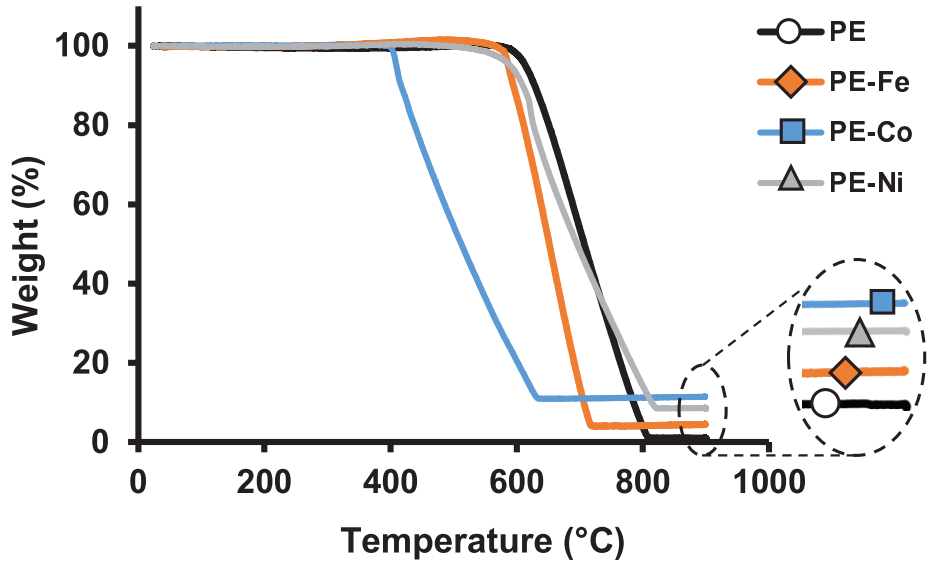

Figure IV.6. TGA in air. Heating rate of 10 °C min^{-1}.

Concerning the PE-Co sample, its thermal stability is significantly lower compared to the others, and this fact could be attributable to the cobalt effect because it catalyses the gasification process further than nickel or iron [30]; besides, the graphitic ordering decreases for PE-Co according to the Raman data. In this regard, as is well known, the stability against oxidation depends on the size, orientation and organization of the graphene layer planes inside the structures [31].

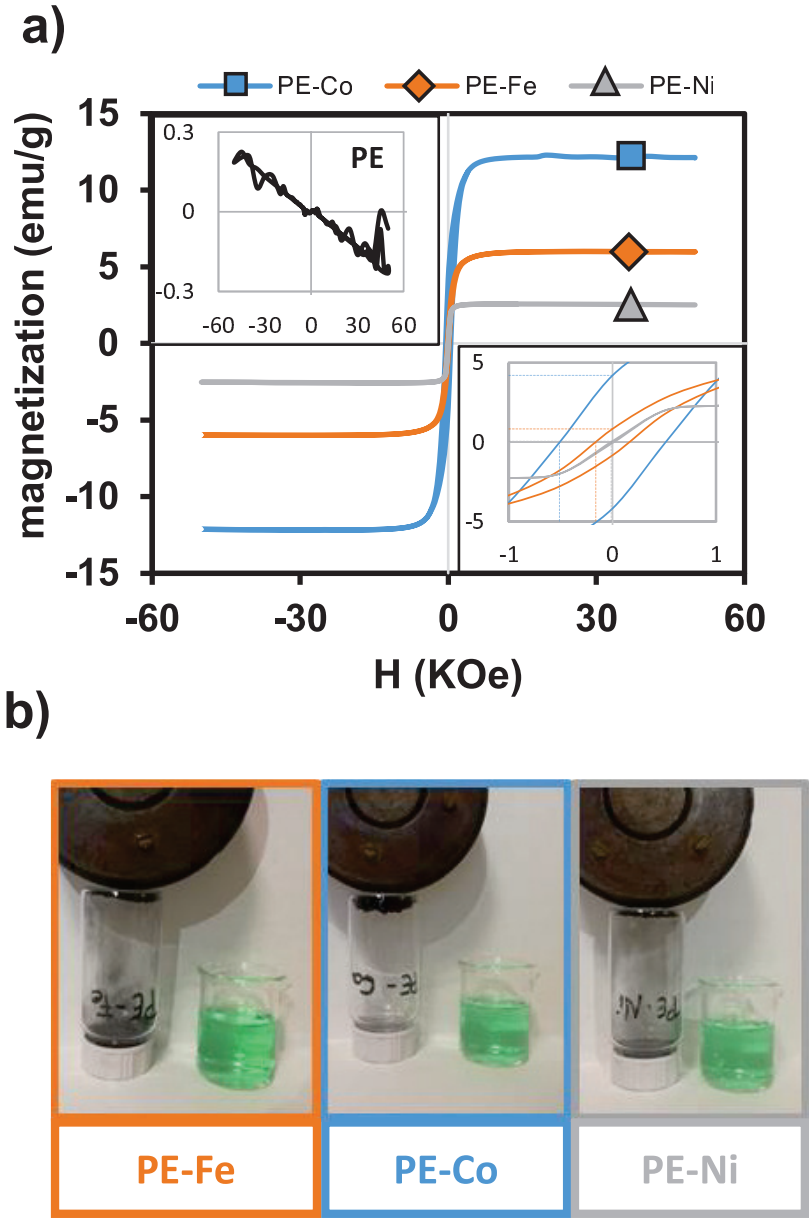

Figure IV.7. Magnetic behaviour: (**a**) Magnetic susceptibility at 293 K. (**b**) Pictures showing magnetic properties.

The magnetic properties were measured at 293 K using a SQUID QUANTUM magnetometer. The magnetization curve of PE (Figure IV.7a) exhibits the typical diamagnetic behaviour of carbon polymorphs [32,33], which becomes ferromagnetic by adding metals, as indicated by the hysteresis loop. However, the narrow loop in PE-Ni indicates a superparamagnetic-like behaviour. The saturation of the magnetization follows the order PE-Co > PE-Fe > PE-Ni, reaching values of 12.15, 6.00 and 2.58 (emu/g), respectively. This trend was already noticed by other authors [34,35]. Furthermore, the magnetism is also evidenced by the fact that the CS nanocomposite materials are strongly attracted by a magnet (Figure IV.7b). This aspect is remarkably interesting, as it enables the separation of the material from the medium upon the application of an external magnetic field.

Consequently, in the view of their properties, these materials would be well suited as electro-catalysts, among other potential applications, but further studies are needed to implement these approaches.

IV.4. Conclusions

In summary, we have obtained highly graphitic carbon microspheres that are quite homogeneous in terms of size and shape, through an easy and fast method, where the precursor polymer was pyrolyzed in the presence of autogenic pressure. The doping with transition metals has triggered the growth of carbon nanostructures, with different sizes, around the microspheres, besides conferring them new properties such as magnetism. Therefore, we have succeeded in obtaining CSs with excellent properties (magnetism, a high degree of graphitization, high conductivity or high thermal stability), which make them suitable for a wide range of applications, even under severe conditions.

IV.5. References

[1] C. Moreno-Castilla, F.J. Maldonado-Hódar, Carbon aerogels for catalysis applications: An overview, Carbon N. Y. 43 (2005) 455–465. doi:10.1016/J.CARBON.2004.10.022.

[2] M. Grigoras, A.M. Catargiu, F. Tudorache, M. Dobromir, Chemical synthesis and characterization of self-doped N-propanesulfonic acid polyaniline derivatives, Iran. Polym. J. 21 (2012) 131–141. doi:10.1007/s13726-011-0011-0.

[3] M. Grigoras, A.M. Catargiu, F. Tudorache, Molecular composites obtained by polyaniline synthesis in the presence of p-octasulfonated calixarene macrocycle, J. Appl. Polym. Sci. 127 (2013) 2796–2802. doi:10.1002/app.37605.

[4] S. Tang, S. Vongehr, X. Meng, Controllable incorporation of Ag and Ag-Au nanoparticles in carbon spheres for tunable optical and catalytic properties, J. Mater. Chem. 20 (2010) 5436–5445. doi:10.1039/c0jm00456a.

[5] M.R. Benzigar, S.N. Talapaneni, S. Joseph, K. Ramadass, G. Singh, J. Scaranto, U. Ravon, K. Al-Bahily, A. Vinu, Recent advances in functionalized micro and mesoporous carbon materials: synthesis and applications, Chem. Soc. Rev. 47 (2018) 2680–2721. doi:10.1039/C7CS00787F.

[6] E. Frackowiak, Q. Abbas, F. Béguin, Carbon / carbon supercapacitors, J. Energy Chem. 22 (2013) 226–240. doi:10.1016/S2095-4956(13)60028-5.

[7] S. Himeno, T. Komatsu, S. Fujita, High-Pressure Adsorption Equilibria of Methane and Carbon Dioxide on Several Activated Carbons, J. Chem. Eng. Data. 50 (2005) 369–376. doi:10.1021/je049786x.

[8] S. Schaefer, V. Fierro, M.T. Izquierdo, A. Celzard, Assessment of hydrogen storage in activated carbons produced from hydrothermally treated organic materials, Int. J. Hydrogen Energy. 41 (2016) 12146–12156. doi:10.1016/J.IJHYDENE.2016.05.086.

[9] X. Du, C. Wang, M. Chen, Y. Jiao, J. Wang, Electrochemical Performances of Nanoparticle Fe3O4/Activated Carbon Supercapacitor Using KOH Electrolyte Solution, J. Phys. Chem. C. 113 (2009) 2643–2646. doi:10.1021/jp8088269.

[10] L. Qiang, Z. Hu, Z. Li, Y. Yang, X. Wang, Y. Zhou, X. Zhang, W. Wang, Q. Wang, Hierarchical porous biomass carbon derived from cypress coats for high energy supercapacitors, J. Mater. Sci. Mater. Electron. (2019). doi:10.1007/s10854-019-01045-1.

[11] J. Liu, N.P. Wickramaratne, S.Z. Qiao, M. Jaroniec, Molecular-based design and emerging applications of nanoporous carbon spheres, Nat. Mater. 14 (2015) 763–774. doi:10.1038/nmat4317.

[12] Y. Chen, B. Song, M. Li, L. Lu, J. Xue, Fe3O4 Nanoparticles embedded in uniform mesoporous carbon spheres for superior High-rate battery applications, Adv. Funct. Mater. 24 (2014) 319–326. doi:10.1002/adfm.201300872.

[13] A. Elmouwahidi, E. Bailón-García, A.F. Pérez-Cadenas, N. Fernández-Sáez, F. Carrasco-Marín, Development of Vanadium-Coated Carbon Microspheres: Electrochemical Behavior as Electrodes for Supercapacitors, Adv. Funct. Mater. 28 (2018) 1802337. doi:10.1002/adfm.201802337.

[14] N.P. Wickramaratne, M. Jaroniec, Activated Carbon Spheres for CO2 Adsorption, ACS Appl. Mater. Interfaces. 5 (2013) 1849–1855. doi:10.1021/am400112m.

[15] A.A. Deshmukh, S.D. Mhlanga, N.J. Coville, Carbon spheres, Mater. Sci. Eng. R Reports. 70 (2010) 1–28. doi:10.1016/J.MSER.2010.06.017.

[16] H.-Q. Wang, Z.-S. Li, Y.-G. Huang, Q.-Y. Li, X.-Y. Wang, A novel hybrid supercapacitor based on spherical activated carbon and spherical MnO2 in a non-aqueous electrolyte, J. Mater. Chem. 20 (2010) 3883–3889. doi:10.1039/C000339E.

[17] P. Ariyadejwanich, W. Tanthapanichakoon, K. Nakagawa, S.. Mukai, H. Tamon, Preparation and characterization of mesoporous activated carbon

from waste tires, Carbon N. Y. 41 (2003) 157–164. doi:10.1016/S0008-6223(02)00267-1.

[18] J. Castelo-Quibén, A. Elmouwahidi, F.J. Maldonado-Hódar, F. Carrasco-Marín, A.F. Pérez-Cadenas, Metal-carbon-CNF composites obtained by catalytic pyrolysis of urban plastic residues as electro-catalysts for the reduction of CO2, Catalysts. 8 (2018) 198. doi:10.3390/catal8050198.

[19] A. Elmouwahidi, J. Castelo-Quibén, J.F. Vivo-Vilches, A.F. Pérez-Cadenas, F.J. Maldonado-Hódar, F. Carrasco-Marín, Activated carbons from agricultural waste solvothermally doped with sulphur as electrodes for supercapacitors, Chem. Eng. J. 334 (2018). doi:10.1016/j.cej.2017.11.141.

[20] PlasticsEurope. Plastic Europe - The facts 2017, (n.d.). https://www.plasticseurope.org/de (accessed 17 March 2019).

[21] M. Inagaki, K.C. Park, M. Endo, Carbonization under pressure, New Carbon Mater. 25 (2010) 409–420. doi:10.1016/S1872-5805(09)60042-1.

[22] S. V. Pol, V.G. Pol, D. Sherman, A. Gedanken, A solvent free process for the generation of strong, conducting carbon spheres by the thermal degradation of waste polyethylene terephthalate, Green Chem. 11 (2009) 448–451. doi:10.1039/b819494g.

[23] Y. Kotolevich, O. Martynyuk, S. Martínez-González, H. Tiznado, A. Pestryakov, M. Avalos Borja, V. Cortés Corberán, N. Bogdanchikova, Novel route of synthesis of ultra-small Au nanoparticles on SiO2 supports, Fuel. 236 (2019) 589–597. doi:10.1016/J.FUEL.2018.09.050.

[24] C. Thomsen, S. Reich, Double resonant raman scattering in graphite, Phys. Rev. Lett. 85 (2000) 5214–5217. doi:10.1103/PhysRevLett.85.5214.

[25] F. Tuinstra, J.L. Koenig, Raman Spectrum of Graphite, J. Chem. Phys. 53 (1970) 1126–1130. doi:10.1063/1.1674108.

[26] Y. Wang, D.C. Alsmeyer, R.L. McCreery, Raman Spectroscopy of Carbon Materials: Structural Basis of Observed Spectra, Chem. Mater. 2 (1990) 557–563. doi:10.1021/cm00011a018.

[27] B. Markovsky, I. Exnar, E. Zinigrad, J. Grinblat, O. Haik, S.K. Martha, Y.

Gofer, G. Deghenghi, D. Aurbach, D. Wang, T. Drezen, LiMnPO[sub 4] as an Advanced Cathode Material for Rechargeable Lithium Batteries, J. Electrochem. Soc. 156 (2009) A541. doi:10.1149/1.3125765.

[28] G.V.S. Rao, V. Aravindan, W. Chuiling, M. V. Reddy, S. Madhavi, B.V.R. Chowdari, Carbon coated nano-LiTi2(PO4)3 electrodes for non-aqueous hybrid supercapacitors, Phys. Chem. Chem. Phys. 14 (2012) 5808. doi:10.1039/c2cp40603a.

[29] L.S.K. Pang, J.D. Saxby, S.P. Chatfield, Thermogravimetric analysis of carbon nanotubes and nanoparticles, J. Phys. Chem. 97 (1993) 6941–6942. doi:10.1021/j100129a001.

[30] C. Moreno-Castilla, J. Rivera-Utrilla, A. López-Peinado, I. Fernández-Morales, F.J. López-Garzón, Gasification reaction of a lignite char catalysed by Cr, Mn, Fe, Co, Ni, Cu and Zn in dry and wet air, Fuel. 64 (1985) 1220–1223. doi:10.1016/0016-2361(85)90178-4.

[31] L. Frusteri, C. Cannilla, K. Barbera, S. Perathoner, G. Centi, F. Frusteri, Carbon growth evidences as a result of benzene pyrolysis, Carbon N. Y. 59 (2013) 296–307. doi:10.1016/J.CARBON.2013.03.022.

[32] M. Fujiwara, E. Oki, M. Hamada, Y. Tanimoto, I. Mukouda, Y. Shimomura, Magnetic Orientation and Magnetic Properties of a Single Carbon Nanotube, J. Phys. Chem. A. 105 (2001) 4383–4386. doi:10.1021/jp004620y.

[33] J. Heremans, C.H. Olk, D.T. Morelli, Magnetic susceptibility of carbon structures, Phys. Rev. B. 49 (1994) 15122–15125. doi:10.1103/PhysRevB.49.15122.

[34] A.A. El-Gendy, E.M.M. Ibrahim, V.O. Khavrus, Y. Krupskaya, S. Hampel, A. Leonhardt, B. Büchner, R. Klingeler, The synthesis of carbon coated Fe, Co and Ni nanoparticles and an examination of their magnetic properties, Carbon N. Y. 47 (2009) 2821–2828. doi:10.1016/J.CARBON.2009.06.025.

[35] X. Sun, A. Gutierrez, M.J. Yacaman, X. Dong, S. Jin, Investigations on magnetic properties and structure for carbon encapsulated nanoparticles of

Fe, Co, Ni, Mater. Sci. Eng. A. 286 (2000) 157–160. doi:10.1016/S0921-5093(00)00628-6.


UNIVERSITAS · GRANATENSIS
PLUS
ULTRA
· 1531 ·


UNIVERSITAS · GRANATENSIS
PLUS
ULTRA
· 1531 ·

CAPÍTULO V

ELECTRO-CATALYTIC BEHAVIOUR OF HIGHLY GRAPHITIC CARBON SPHERES NANOCOMPOSITES FOR THE OXYGEN REDUCTION REACTION (ORR)


UNIVERSITAS · GRANATENSIS
PLUS
ULTRA
· 1531 ·

V.1 Introduction

The unstoppable growth in energy demand has encouraged intensely the researching on alternative energy conversion and storage systems highly efficient which have to be adequately addressed to maintain the sustainability of our environment. Therefore, the production of electrical energy from chemical reactions by using fuel cells, especially the ones refueled with hydrogen from renewable energy, are generally considered one of the most promising solutions because of their competitive advantages, such as zero emission, high efficiency, fast refueling, and low upfront cost [1].

In a typical PEMFC, fuel molecules (e.g., hydrogen) are oxidized on the anode, and oxygen gas is reduced on the cathode, outputting electric energy with pure water and heat as the only by-products [2–4]. Unfortunately, the difficulty in O_2 activation and O–O bond cleavage causes sluggish kinetics of the oxygen reduction reaction (ORR) on the cathode, thus, great efforts are still being taken to improve the ORR kinetics [5–7].

At present, Pt and its alloys are generally considered to be the most efficient ORR catalysts [8–11]. Nevertheless, not only the high cost of Pt greatly hampers further large-scale adoption of PEMFCs but also its low tolerance to fuel molecules. Taking this into consideration, special attention has been paid during the last few decades on the developing of low-Pt-content catalysts [12–14] besides, alternative catalysts based on non-precious metals and metal-free materials are more interesting proposals and they are being actively studied [15–18]. In this regard, carbon based materials are considered as optimal candidates to accomplish the oxygen reduction reaction [19–23].

Carbon materials present numerous advantages such as high surface area, electrical conductivity, high mechanical strength and high electrochemical corrosion resistance. Moreover, their versatility facilitates the possibility of modifying on demand their textural, chemical and electrical

properties by tuning the carbon precursor as well as by doping appropriately in accordance with the required applications [24,25].

Owing to this overview, developing electro-catalysts based on carbon doped with transition metals is certainly an attractive idea, especially doping with iron, nickel or cobalt, since those metals are among the most abundant on Earth's crust, and therefore competitively-priced.

In the present work, we demonstrate the high electro-catalytic behaviour of carbon spheres nanocomposites obtained by catalytic pyrolysis under pressure.

V.2 Experimental

V.2.1 Synthesis of carbon spheres nanocomposites

The synthesis of carbon spheres nanocomposites has been previously described in Chapter IV. Briefly, some amount of low density polyethylene (LDPE) was mixed with the corresponding Fe, Co or Ni acetate and carbonized into a closed reactor at 700 ºC obtaining PE, PE-Fe, PE-Co and PE-Ni materials.

V.2.2 Textural and chemical characterization

The techniques such as thermogravimetric analysis (TGA), scanning electron microscopy (SEM), high-resolution transmission electron microscopy (HRTEM), X-ray diffraction (XRD), Raman spectroscopy and the magnetic susceptibility, were already described in the previous chapter. However, the carbon spheres nanocomposites materials were further characterized in this work by X-ray photoelectron spectroscopy (XPS) by using a Kratos Axis Ultra-DLD spectrometer equipped with a hemispherical electron analyzer connected to a detector DLD (delay-line detector). HRTEM has been also included in this Chapter because, in order to amplify

this study, new analysis and images were made after the publication of the corresponding *Communication*, Chapter IV

V.2.3 Electrochemical measurements

The CSs nanocomposistes were characterized electrochemically, with a Biologic VMP Multichannel potentiostat, using a standard three-electrode cell. CSs nanocomposites, a platinum wire and Ag/AgCl were used as cathode, counter electrode and reference electrode respectively. To evaluate the electro-catalytic activity, a Rotating Disk Electrode (RDE) (Metrohm AUTOLAB RDE-2, 3 mm Glassy Carbon tip), was used as a working electrode, in which, carbon materials were deposited.

In order to study the behaviour of each sample through the electrolyte containing or in absence of oxygen, Cyclic Voltammetries (CVs) were performed in O2-saturated 0.1M KOH solution or in a 0.1M KOH solution completely degasified (by bubbling N2). The sweeping voltage rate was 50mVs, from 0.4V to -0.8V while RDE was rotating at 1000rpm. To prepare the working electrode, 5mg of sample were dispersed in 1mL of a solution previously prepared which contains Nafion (5%) and water in a 1:9 (v:v) ratio and sonicated for 30 min until a homogeneous and stable ink was obtained; after that, 10 µL of this ink were loaded on RDE tip and dried under infrared radiation. The Glassy Carbon tip had been previously polished with alumina powder. Afterwards, Linear Sweep Voltammetries (LSVs) were measured in an O_2-saturated 0.1M KOH solution at different rotation rates from 500 rpm to 4000 rpm. The experiments were conducted from 0.4V to -0.8V (Ag/AgCl) at a sweep rate of 5 mVs^{-1}.

The experimental data were fitted to the Koutecky-Levich model in order to evaluate the electro-catalytic performance of samples and to calculate the number of electrons transferred for each of them as well as the kinetic density current (j_K) and the onset potential (E_{ONSET}).

V.3 Results and discussion

V.3.1 Textural and chemical characterization

Figure V.1 and Figure V.II show the HRTEM images of PE, PE-Fe, PE-Co and PE-Ni samples that complement the images depicted in chapter IV. Here, we can better appreciate the graphitization of these materials. Figure V.1a shows CSs of PE which could not be passed through by the beam of electrons, evidencing the high density of these spheres. However, the edge of the CS in detail (Fig. V.1b), reveals the graphitic lines, demonstrating the high degree of graphitization.

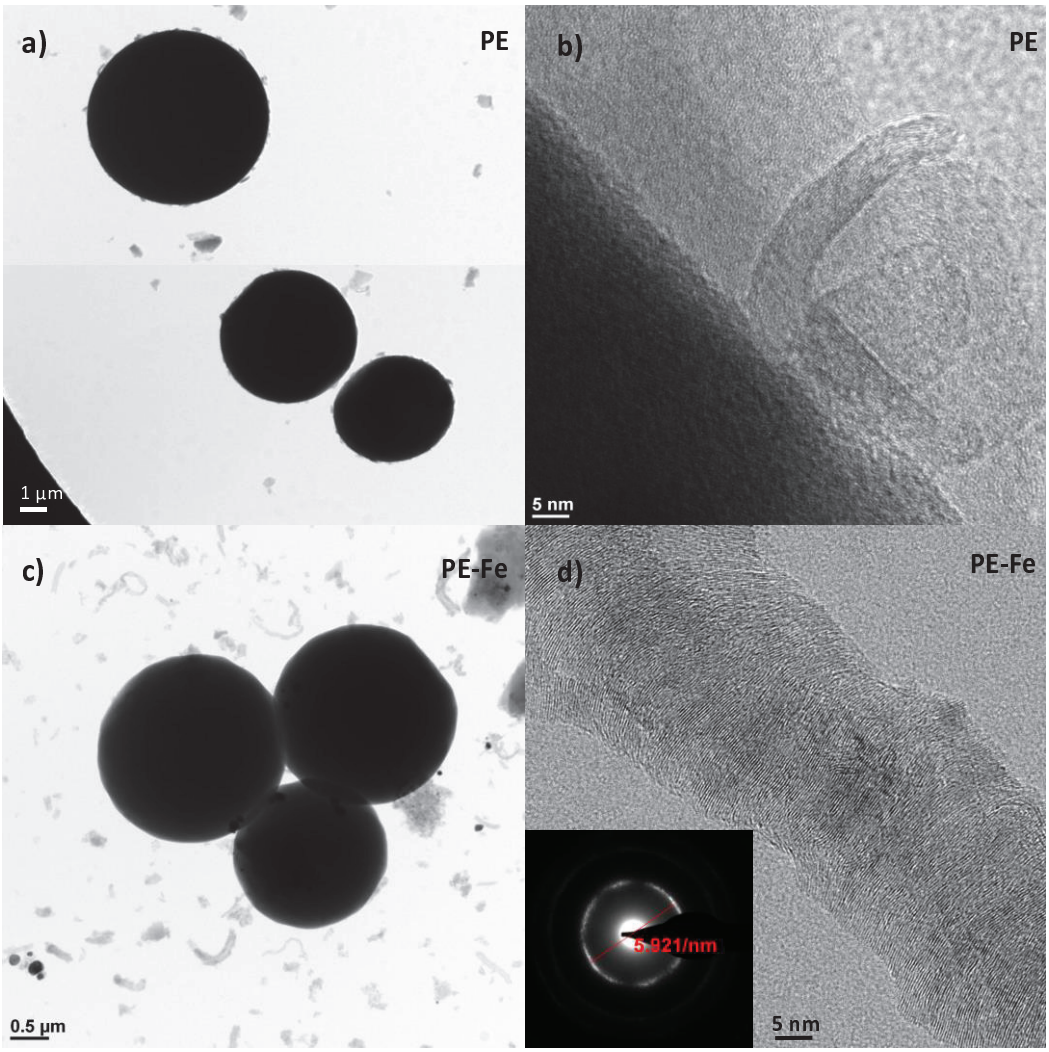

Figure V.1. HRTEM images of PE (a,b), and PE-Fe (c,d) samples

In Figure V.1c, it can be appreciated the carbon microspheres, as well as the carbon nanofibres and the iron particles (responsible for having developed these CNFs) highly dispersed through the carbon material. For example, Fig. V.1d shows one of these CNF with the Fast Fourier Transform (FFT) analysis that clearly illustrates the lattices lines of graphite corresponding to the (002) plane with a 0.337 nm d-spacing.

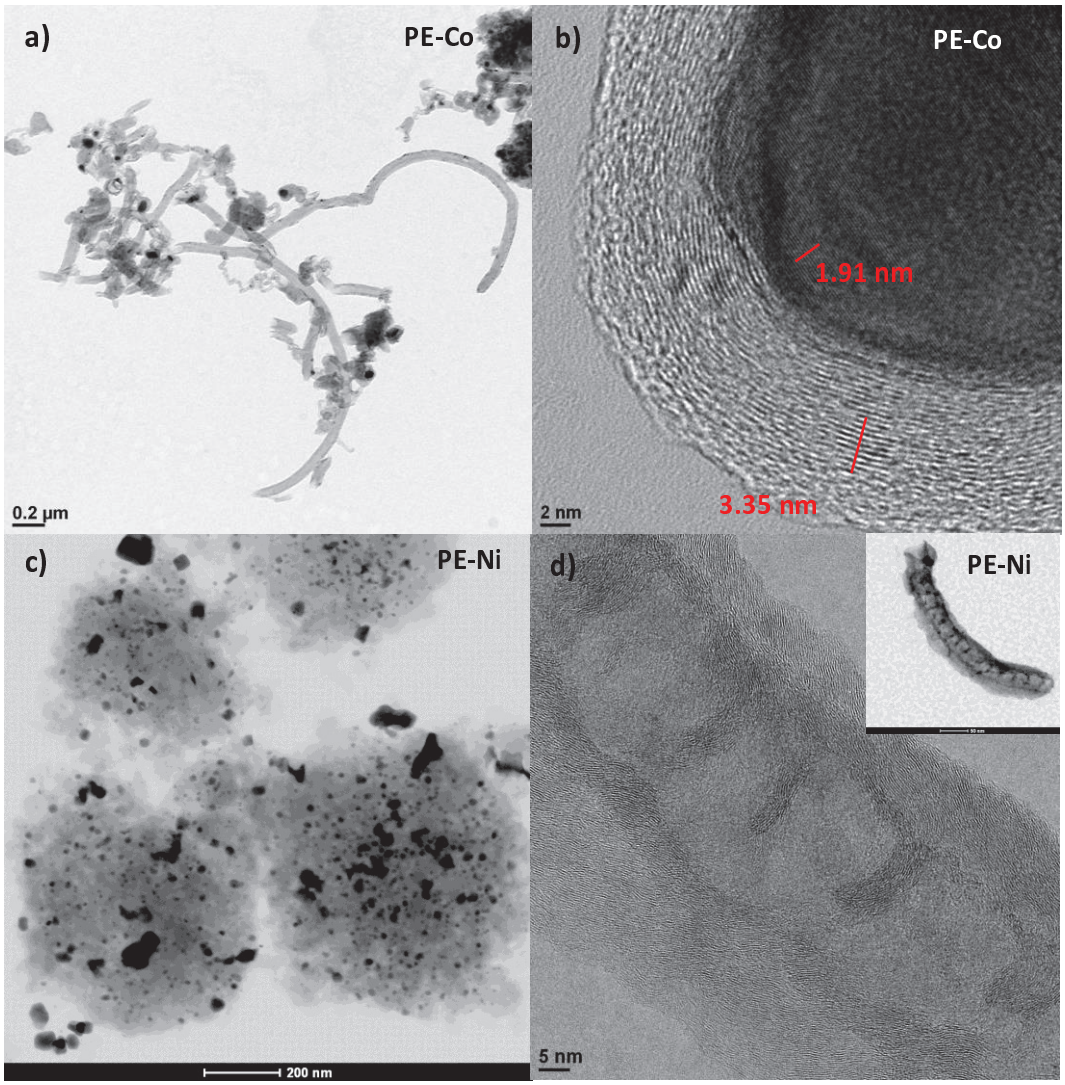

Figure V.2. HRTEM images of PE-Co (a,b) and PE-Ni (c,d)

In the same line, Fig.V.2a shows the CNFs obtained by means of the cobalt particles. These nanofibres are significantly longer than the ones

obtained with Iron, such observation had been already noticed by SEM images (chapter IV). Additionally, here we can appreciate the graphitization around the cobalt particles (Fig. V.2c), where it was also found the hexagonal phase (hcp) of Co^0 (0.191 nm d-spacing). Finally, PE-Ni sample presents a really good dispersion of the metal phase through the carbon matrix and also, it has developed nanofibres in which it can be appreciated the footprint generated during their growing. These observations are in good agreement with Raman spectroscopy (chapter IV) and XRD data (Fig. V.3 and Table V.1), where it had been already found the metal in 0 state for Cobalt and Nickel, accordingly with JCPDS 15-0806 (Co^0 fcc), 05-0727 (Co^0 hcp) and 04-0850 (Ni^0 fcc) cards. However, the small diffraction peaks of PE-Fe could be assigned to the formation of the spinel Fe_3O_4 (JCPDS 75-0033) whose existence has been confirmed by XPS. It is important to note that all samples got a high degree of graphitization pointed out by the intense diffraction peaks corresponding to the graphitic crystals (JCPDS 89-84.87).

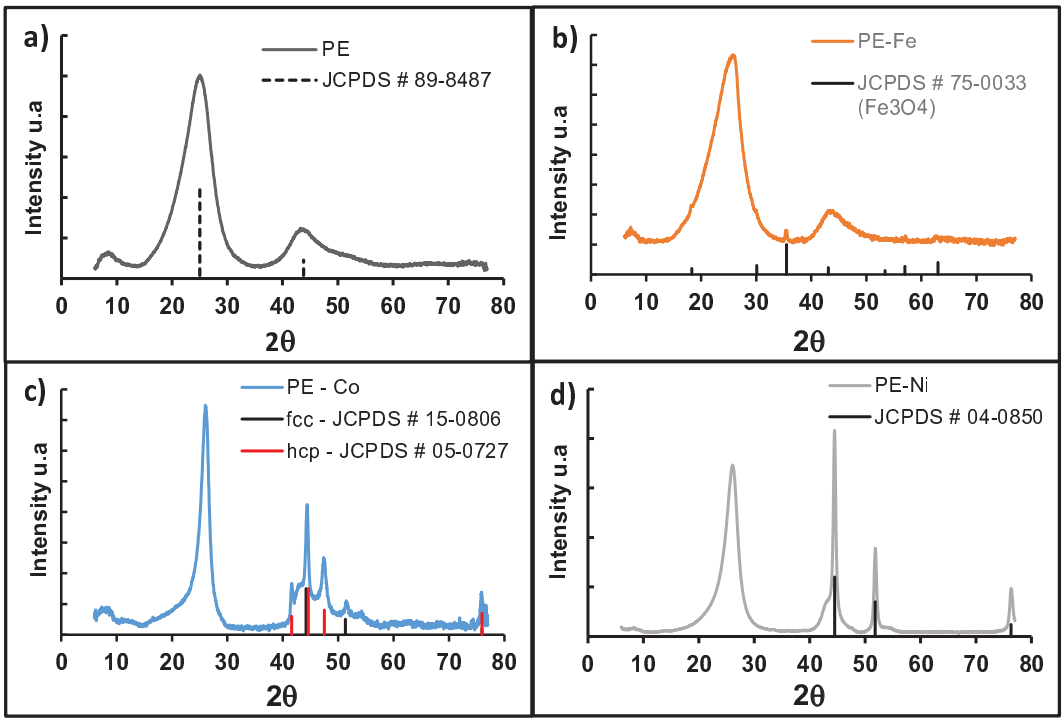

Figure V.3. XRD patterns of PE, PE-Fe PE-Co and PE-Ni with the diffraction peaks of the corresponding JCPDS cards

Table V.1 shows the average crystal size for both, the corresponding metal phase and the graphitic crystals (L_c), obtained by applying the Scherrer equation (1) to the XRD data.

$$d = \frac{k \cdot \lambda}{\beta \cdot cos\theta} \qquad (1)$$

Where *k* is the shape coefficient for reciprocal lattice point (here, assuming k = 0.9), λ the wavelength of the X-ray radiation (1.54056 Å), β is the full width at half maximum (FWHM) of the peak, and θ is the Bragg angle.

Table V.1. Average crystal size of the graphitic crystals and metal phases

Sample	d_{XRD} (nm)			
	L_c	Ni	Fe	Co
PE	1.42	-	-	-
PE-Ni	2.96	15.25	-	-
PE-Fe	1.36	-	n.d.*	-
PE-Co	4.71	-	-	11.72

*Fe peak was not resolved enough to apply the Scherrer eq.

All samples show very small metal crystal size, implying that the metal phase is very well-dispersed though the carbon matrix. On the other hand, Cobalt was which has developed larger graphitic crystals, followed by Ni. It should be mentioned that, similar values of L_C were described in literature for carbon aerogels obtained at temperatures between 1000 ºC-1800 ºC, but in no case were obtained Lc > 1.42 in absence of graphitic catalyst even at 1800 ºC [26,27]. This observation confirms the graphitization effect of the generated pressure, since these materials were obtained just at 700 ºC.

Figures V.4, Figure V.5 and Table V.2 collect the XPS data. The C_{1s} region spectra of PE and PE-Fe samples is compared in Fig.V.4, where is clearly observed the low amount of oxygen in PE since the two main peaks correspond to C=C (284.6 eV) and C-C (285.6) and there is no almost

presence of oxygen (Table V.2). Regarding the metal phase, most of the metal content is not located in the external surface area of the carbon phases, especially in PE-Fe and PE-Co. Only 0.74% of Fe was found by XPS, compared to TGA data (3% wt.), it means that most of Fe is covered by carbon and so, because of the penetrability of XPS, it cannot be measured. In the case of cobalt, its presence on the external surface area of the composite is negligible, since the Co was not detected by XPS (Fig V.5b).

However, in the case of PE-Ni both metal contents determined, by XPS or TGA, are less different than in the case of the other samples (3.88 vs. 6.65% wt.), but these still reveal lower Ni-content on the external surface area of the carbon phases. Amongst this superficial Ni, 58% is found as part of an oxide, while the other 42% is still in zero oxidation state, evidencing the reducing power of the carbon phase.

The carbonaceous phase does appear to play an important role in the stabilization of magnetite specie, being that it was only found the Fe_3O_4 oxide. The deconvolution of the XP spectra has shown that Fe^{2+} represent the 34% while the remaining 66% corresponds to Fe^{3+} [28], which perfectly coincide with Magnetite, where Fe^{2+} and Fe^{3+} represent the 33.3% and 66.6% respectively.

Table V.2. Chemical composition by XPS and the metal content by TGA

Sample	C_{XPS} %wt	O_{XPS} %wt	$Metal_{XPS}$ %wt	$Metal_{TGA}$ %wt
PE	97.61	2.39	-	-
PE-Fe	93.60	5.65	0.74	3.03
PE-Co	95.23	4.77	n.d	7.84
PE-Ni	91.68	4.44	3.88	6.65

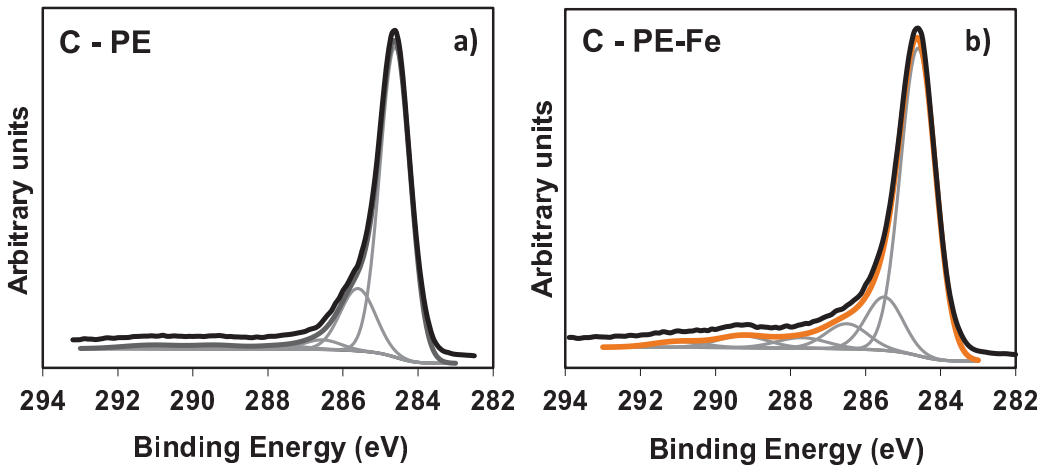

Figure V.4. XP spectra of C_{1s} region for PE (a) and PE-Fe (b)

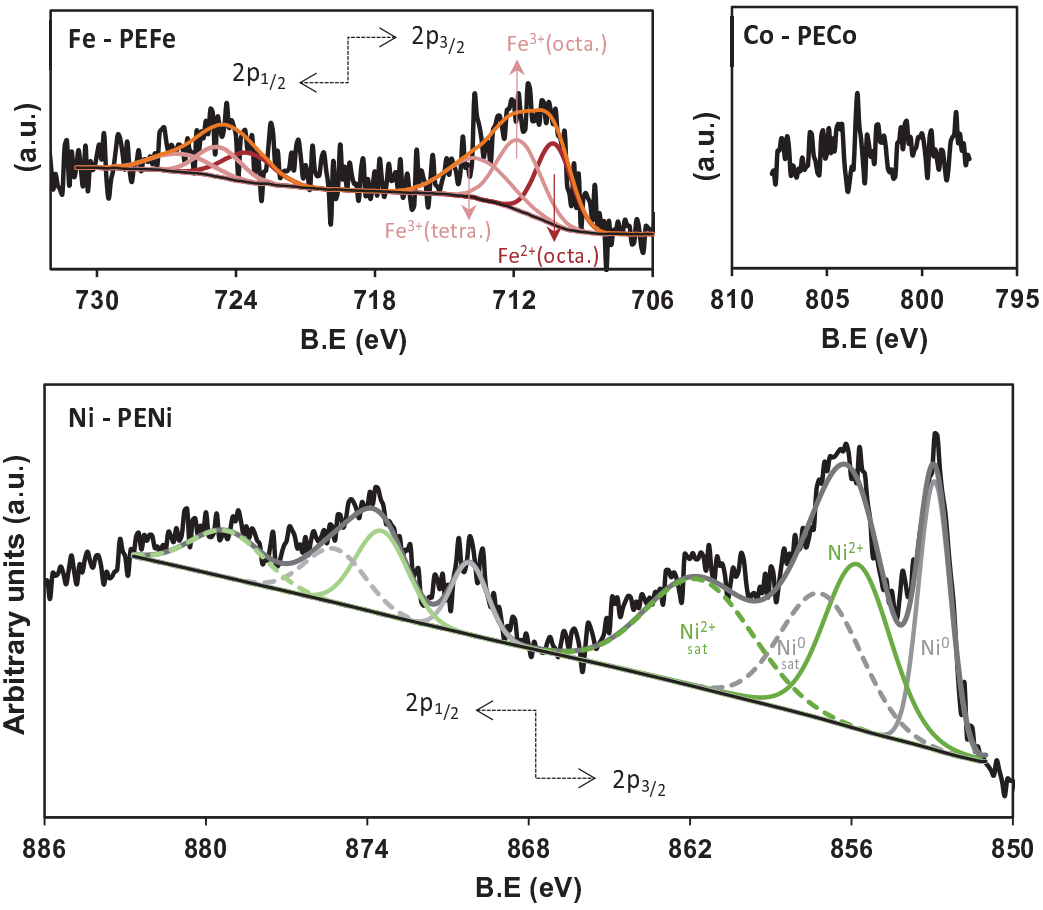

Figure V.5. XPS patterns of the 2p metal region for PE-Fe (a), Pe-Co (b) and PE-Ni (c)

V.3.2 Oxygen Reduction Reaction

Cyclic Voltammetries (CVs) were performed in the presence and absence of Oxygen in order to compare the behaviour of the samples in both situations. The CV curves of each sample are depicted in Fig.V.6. All materials present electro-catalytic activity in the presence of oxygen, since it can be observed that, in all cases, it is produced an increment in the current intensity at values near to -0.2 V (vs. Ag/Ag/Cl) (red line), corresponding to the electro-reduction of oxygen.

Although it is predicted ORR activity for all samples, PE-Fe and PE-Co are the ones which have achieved the highest current intensity at the same potential. It is also worth noting that in Figure 6c, the CV curve of PE-Co in absence of oxygen, shows a pair of broad redox peaks within a potential window from 0.1V to 0.3V which are typical characteristics of faradic reactions in the alkaline electrolyte [29,30]. This result indicates that a little percentage of cobalt could be situated in the macroporous of the sample.

On the other hand, the narrow shape of the curves that enclose a little area, and so, little capacitance, let us glimpse the low surface area of these materials.

After the performance of CVs, were obtained the corresponding Linear Sweep Voltammetrys (LSV) into the O_2-saturated electrolyte at a sweeping rate of 5 mVs^{-1} from 0.4 V to -0.8 V. The experiments were conducted at different rotation speed from 500 rpm to 4000 rpm, in order to apply the Koutecky-Levich equation.

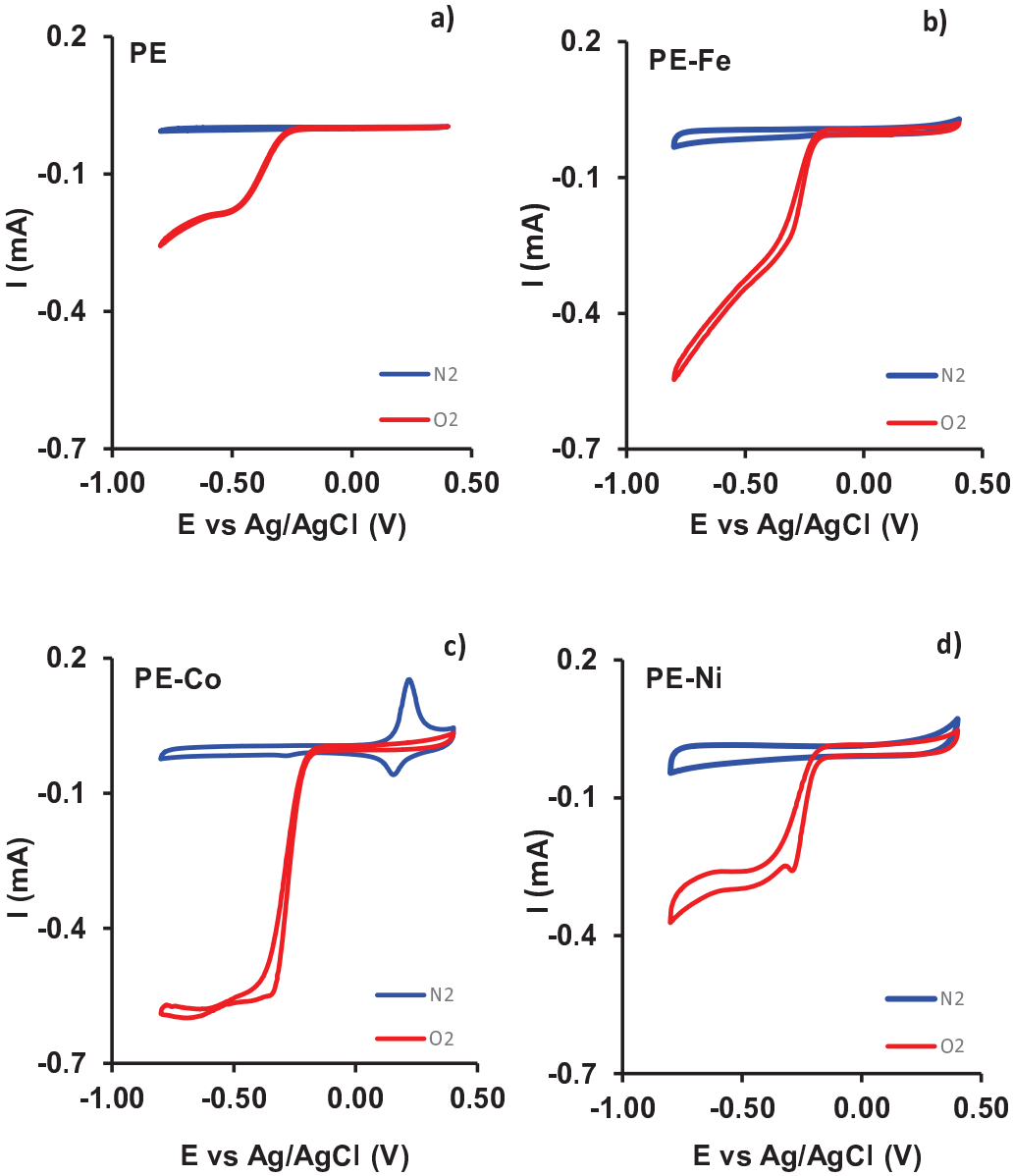

Figure V.6. Cyclic Voltagrams at 1000 rpm and 50 mV/s of PE (a), PE-Fe (b), PE-Co (c) and PE-Ni (d)

Figure V.7 show an example of LSVs for the PE-Co sample (Fig V.7a) and also, the comparison for all samples at 4000 rpm.

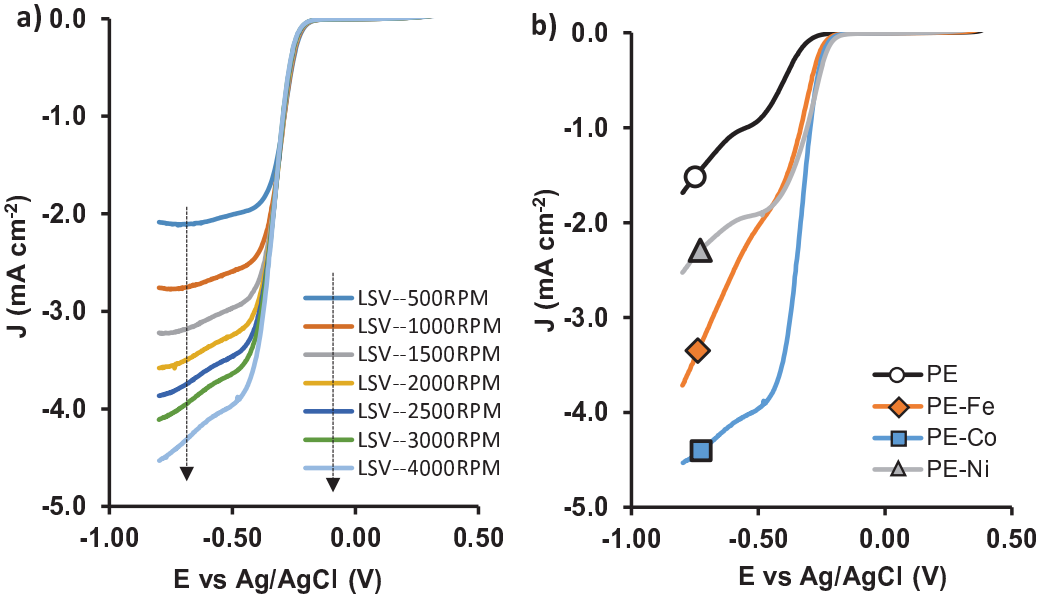

Figure V.7. LSV curves for PE-Co at different RDE rates (a), and LSV curves at 4000 rpm for all samples (b)

Although PE sample shows catalytic activity for ORR, Fig 7b manifest that it shows a poor performance, pointed out not only for the lower density current but also because of the OR reaction starts at higher potentials, while the other samples catalyze it at lower E°.

Data of LSV were fitted to the K-L equation obtaining the K-L plot (Fig. V.8a), then, from the analysis of the K-L plot were obtained de number of electrons transferred at different potentials (Fig. V.8b) as well as the kinetic density current (j_k) (Table V.3)

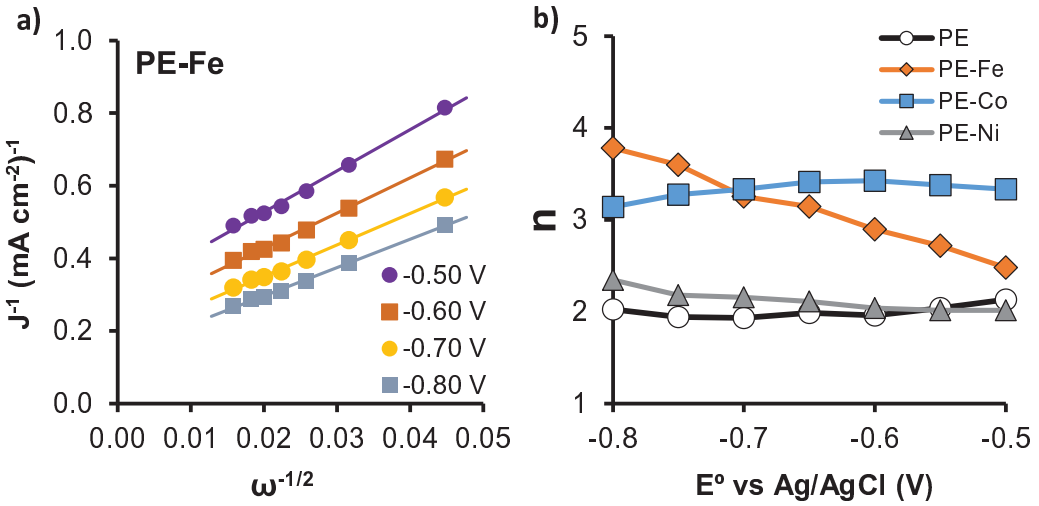

Figure V.8. K-L plot for PE-Fe (a) and number of electron transferred at each potential

Table V.3. Parameters obtained from the analysis of LSV curves

Sample	E_{ONSET} (v)	j_k $mAcm^{-2}$	n
PE	-0.30	2.65	2.0
PE-Fe	-0.24	6.40	3.8
PE-Co	-0.26	12.65	3.1
PE-Ni	-0.20	4.64	2.3

* j_k and n refer to K-L fitting at -0.8V

Metal-free material (PE), is able to accomplish the oxygen reduction reaction purely by the 2-electron pathway, but the reaction starts at -0.30V that is the highest potential compared to the others. However, when some of the metals are present, the electro-catalytic activity improves considerably, all metal-samples present lower E_{ONSET}, improved kinetics and they are able to transfer more electrons. While PE-Ni shows similar n-value than PE, but with improvements in the other parameters, PE-Co and PE-Fe stand out in all parameters, especially in the case of PE-Fe, which performs the ORR by the 4 electrons pathway, and therefore not producing

peroxides species, even though the iron content is only a 3 % wt. However, in spite of PE-Co lead the reaction by a mixed 2-4 electrons pathway, it does it with better kinetics, and also its electro-catalytic performance remains constant at different potentials. This fact could be related with the amount of metal present, since there is 8% of Co, while only 3% of iron in the case of PE-Fe. Previous works have demonstrated that an increment in the metal content leads to better kinetics [31]. On the other hand, the fact that only samples PE-Co and PE-Fe are partially composed by carbon nanofibers, being these two samples the best catalysts independently of the total metal content and its distribution, suggests that CNFs could play a very positive role in the improvement if the catalytic behaviour.

V.4. Conclusions

The present work reports the successful obtaining of highly graphitic carbon materials from Low Density Polyethylene by a quick an easy method. Not only the metal content but also the carbon nanostructures developed in these composites, can influence the electro-catalytic activity leading to a 4-electron pathway although a positive effect of the meso-macro structure cannot be discarded. In spite of, further experiments have to be carried out to clarify this point. In any case, these carbon-metal composites are excellent candidates as ORR electro-catalyst.

V.5. References

[1] M.K. Debe, Electrocatalyst approaches and challenges for automotive fuel cells, Nature. 486 (2012) 43–51. doi:10.1038/nature11115.

[2] M. Winter, R.J. Brodd, What Are Batteries , Fuel Cells , and Supercapacitors ?, 104 (2004) 4245–4270. doi:10.1021/cr020730k.

[3] A. Gabe, J. García-Aguilar, Á. Berenguer-Murcia, E. Morallón, D. Cazorla-Amorós, Key factors improving oxygen reduction reaction activity in cobalt nanoparticles modified carbon nanotubes, Appl. Catal. B Environ. 217 (2017) 303–312. doi:10.1016/J.APCATB.2017.05.096.

[4] R. Engel, Tomorrow's energy: Hydrogen, fuel cells, and the prospects for a cleaner planet, Int. J. Hydrogen Energy. 37 (2012) 16264. doi:10.1016/J.IJHYDENE.2012.08.018.

[5] J. Zhang, M.B. Vukmirovic, K. Sasaki, A.U. Nilekar, M. Mavrikakis, R.R. Adzic, Mixed-Metal Pt Monolayer Electrocatalysts for Enhanced Oxygen Reduction Kinetics, J. Am. Chem. Soc. 127 (2005) 12480–12481. doi:10.1021/ja053695i.

[6] V.R. Stamenkovic, B. Fowler, B.S. Mun, G. Wang, P.N. Ross, C.A. Lucas, N.M. Marković, Improved Oxygen Reduction Activity on $Pt_3Ni(111)$ via Increased Surface Site Availability, Science (80-.). 315 (2007) 493 LP-497. doi:10.1126/science.1135941.

[7] H.A. Gasteiger, S.S. Kocha, B. Sompalli, F.T. Wagner, Activity benchmarks and requirements for Pt, Pt-alloy, and non-Pt oxygen reduction catalysts for PEMFCs, Appl. Catal. B Environ. 56 (2005) 9–35. doi:10.1016/J.APCATB.2004.06.021.

[8] S. Samad, K.S. Loh, W.Y. Wong, T.K. Lee, J. Sunarso, S.T. Chong, W.R. Wan Daud, Carbon and non-carbon support materials for platinum-based catalysts in fuel cells, Int. J. Hydrogen Energy. 43 (2018) 7823–7854. doi:10.1016/J.IJHYDENE.2018.02.154.

[9] M. Min, J. Cho, K. Cho, H. Kim, Particle size and alloying effects of Pt-based alloy catalysts for fuel cell applications, Electrochim. Acta. 45 (2000) 4211–4217. doi:10.1016/S0013-4686(00)00553-3.

[10] B. Lim, M. Jiang, P.H.C. Camargo, E.C. Cho, J. Tao, X. Lu, Y. Zhu, Y. Xia, Pd-Pt Bimetallic Nanodendrites with High Activity for Oxygen Reduction, Science (80-.). 324 (2009) 1302 LP-1305. doi:10.1126/science.1170377.

[11] J. Greeley, I.E.L. Stephens, A.S. Bondarenko, T.P. Johansson, H.A. Hansen, T.F. Jaramillo, J. Rossmeisl, I. Chorkendorff, J.K. Nørskov, Alloys of platinum and early transition metals as oxygen reduction electrocatalysts, Nat. Chem. 1 (2009) 552. doi:10.1038/nchem.367.

[12] L. Wang, P. Wurster, P. Gazdzicki, M. Roussel, D.G. Sanchez, L. Guétaz, P.-A. Jacques, A.S. Gago, K. Andreas Friedrich, Investigation of activity and stability of carbon supported oxynitrides with ultra-low Pt concentration as

ORR catalyst for PEM fuel cells, J. Electroanal. Chem. 819 (2018) 312–321. doi:10.1016/J.JELECHEM.2017.10.067.

[13] W. Zhu, J.P. Zheng, R. Liang, B. Wang, C. Zhang, G. Au, E.J. Plichta, Ultra-low platinum loading high-performance PEMFCs using buckypaper-supported electrodes, Electrochem. Commun. 12 (2010) 1654–1657. doi:10.1016/J.ELECOM.2010.09.019.

[14] S. Arisetty, X. Wang, R.K. Ahluwalia, R. Mukundan, R. Borup, J. Davey, D. Langlois, F. Gambini, O. Polevaya, S. Blanchet, Catalyst Durability in PEM Fuel Cells with Low Platinum Loading, J. Electrochem. Soc. . 159 (2012) B455–B462. doi:10.1149/2.jes113064.

[15] R. Bashyam, P. Zelenay, A class of non-precious metal composite catalysts for fuel cells, in: Mater. Sustain. Energy, n.d.: pp. 247–250. doi:10.1142/9789814317665_0034.

[16] Z. Chen, D. Higgins, A. Yu, L. Zhang, J. Zhang, A review on non-precious metal electrocatalysts for PEM fuel cells, Energy Environ. Sci. 4 (2011) 3167–3192. doi:10.1039/c0ee00558d.

[17] L. Yang, J. Shui, L. Du, Y. Shao, J. Liu, L. Dai, Z. Hu, Carbon- Based Metal-Free ORR Electrocatalysts for Fuel Cells: Past, Present, and Future, Adv. Mater. 31 (2019) 1804799. doi:10.1002/adma.201804799.

[18] G.A. Ferrero, A.B. Fuertes, M. Sevilla, M.-M. Titirici, Efficient metal-free N-doped mesoporous carbon catalysts for ORR by a template-free approach, Carbon N. Y. 106 (2016) 179–187. doi:10.1016/J.CARBON.2016.04.080.

[19] K. Jayasayee, J.A.R. Van Veen, T.G. Manivasagam, S. Celebi, E.J.M. Hensen, F.A. de Bruijn, Oxygen reduction reaction (ORR) activity and durability of carbon supported PtM (Co, Ni, Cu) alloys: Influence of particle size and non-noble metals, Appl. Catal. B Environ. 111–112 (2012) 515–526. doi:10.1016/J.APCATB.2011.11.003.

[20] J. Quílez-Bermejo, E. Morallón, D. Cazorla-Amorós, Oxygen-reduction catalysis of N-doped carbons prepared: Via heat treatment of polyaniline at over 1100 °c, Chem. Commun. 54 (2018) 4441–4444. doi:10.1039/c8cc02105h.

[21] G.A. Ferrero, K. Preuss, A.B. Fuertes, M. Sevilla, M.-M. Titirici, The influence of pore size distribution on the oxygen reduction reaction performance in nitrogen doped carbon microspheres, J. Mater. Chem. A. 4 (2016) 2581–2589. doi:10.1039/C5TA10063A.

[22] A. Abdelwahab, J. Castelo-Quibén, J.F. Vivo-Vilches, M. Pérez-Cadenas, F.J. Maldonado-Hódar, F. Carrasco-Marín, A.F. Pérez-Cadenas, Electrodes Based on Carbon Aerogels Partially Graphitized by Doping with Transition Metals for Oxygen Reduction Reaction, Nanomaterials. 8 (2018) 266. doi:10.3390/nano8040266.

[23] A. Elmouwahidi, J.F. Vivo-Vilches, A.F. Pérez-Cadenas, F.J. Maldonado-Hódar, F. Carrasco-Marín, Free metal oxygen-reduction electro-catalysts obtained from biomass residue of the olive oil industry, Chem. Eng. J. 306

(2016) 1109–1115. doi:10.1016/j.cej.2016.08.042.

[24] M.R. Benzigar, S.N. Talapaneni, S. Joseph, K. Ramadass, G. Singh, J. Scaranto, U. Ravon, K. Al-Bahily, A. Vinu, Recent advances in functionalized micro and mesoporous carbon materials: synthesis and applications, Chem. Soc. Rev. 47 (2018) 2680–2721. doi:10.1039/C7CS00787F.

[25] C. Moreno-Castilla, F.J. Maldonado-Hódar, Carbon aerogels for catalysis applications: An overview, Carbon N. Y. 43 (2005) 455–465. doi:10.1016/J.CARBON.2004.10.022.

[26] F.J. Maldonado-Hódar, C. Moreno-Castilla, J. Rivera-Utrilla, Y. Hanzawa, Y. Yamada, Catalytic Graphitization of Carbon Aerogels by Transition Metals, Langmuir. 16 (2000) 4367–4373. doi:10.1021/la991080r.

[27] M. Sevilla, A.B. Fuertes, Catalytic graphitization of templated mesoporous carbons, Carbon N. Y. 44 (2006) 468–474. doi:10.1016/J.CARBON.2005.08.019.

[28] J. Lu, F. Fu, L. Zhang, B. Tang, Insight into efficient co-removal of Se(IV) and Cr(VI) by magnetic mesoporous carbon microspheres: Performance and mechanism, Chem. Eng. J. 346 (2018) 590–599. doi:10.1016/j.cej.2018.04.077.

[29] X. Wang, C. Yan, A. Sumboja, P.S. Lee, High performance porous nickel cobalt oxide nanowires for asymmetric supercapacitor, Nano Energy. 3 (2014) 119–126. doi:10.1016/j.nanoen.2013.11.001.

[30] V. Gupta, S. Gupta, N. Miura, Potentiostatically deposited nanostructured CoxNi1− x layered double hydroxides as electrode materials for redox-supercapacitors, J. Power Sources. 175 (2008) 680–685. doi:10.1016/j.jpowsour.2007.09.004.

[31] A. Abdelwahab, J. Castelo-Quibén, J.F. Vivo-Vilches, M. Pérez-Cadenas, F.J. Maldonado-Hódar, F. Carrasco-Marín, A.F. Pérez-Cadenas, Electrodes based on carbon aerogels partially graphitized by doping with transition metals for oxygen reduction reaction, Nanomaterials. 8 (2018). doi:10.3390/nano8040266.


UNIVERSITAS · GRANATENSIS
PLUS
ULTRA
· 1531 ·

CAPÍTULO VI

MESOPOROUS CARBON NANOSPHERES WITH IMPROVED CONDUCTIVITY FOR ELECTRO-CATALYTIC REDUCTION OF OXYGEN AND CO_2


UNIVERSITAS · GRANATENSIS
PLUS
ULTRA
· 1531 ·

VI.1. Introduction

Most of the primary energy used today in the world is coming from fossil fuels (over 80%) and therefore limited resources: oil, natural gas and coal [1]. However, the dwindling global reserves of fossil fuels coupled with the need to protect and care the environment against the threat of global warming, make it necessary the study and implementation of new clean and renewable technologies to supply the energy needs of the population. Greenhouse gas emissions are mainly produced by the transport sector and power stations where huge amounts of fossil fuels are consumed [2]. Because of that, many efforts are being taken to reduce CO_2 emissions, particularly anthropogenic emissions, since these are responsible for altering the natural carbon dioxide cycle. Therefore, reducing CO_2 concentration and transforming CO_2 into useful materials seems to be critical for environmental protection. In this way, the electro-reduction of carbon dioxide to hydrocarbons is an attractive choice to supply this demand inasmuch as the energy required to accomplish this reaction could come from renewable energy sources, and therefore, it would close the cycle since net emissions of CO_2 would not increase.

On the other hand, another promising technology is also the fuel cells, which provides clean and sustainable energy [3]. This technology has generated great interest because of its high energy conversion efficiency, clean and renewable character and the potential large-scale applications [4]. The most important reaction controlling the efficiency of the fuel cell is the oxygen reduction, hence the importance of its study and optimization [5]. Due to the slow kinetics of oxygen reduction reaction (ORR), the use of catalysts is required to increase the activity of this cathodic reaction which in turn promotes the transformation by a direct path (4 electrons transferred), thereby, it increases the faradic efficiency. Traditionally, Pt used to be the best catalyst for ORR, unfortunately, the high cost and limited reserves of Pt are the main barriers for large-scale production of fuel cells

[6]. Besides, not only the prohibitive price of Pt is the determining factor, but also the sensitiveness to contaminants (impurities contained in the feed stream of the fuel cell) which can easily poison it is an important limiting factor [5,7]. Therefore, the development and optimization of alternative catalysts for ORR that are cost-effective, accessible and even with improved performance than conventional Pt catalysts, are required.

On this line, one reaction or the other can be carried out by means of catalysts based on the metal dispersion through a carbon matrix in such a manner as to improve cost and efficiency while decreasing metal loading. Furthermore, due to the high stability, electrical properties, tunability as well as the high specific surface area of carbon materials it is allowed high dispersion of particles guaranteeing a large reaction area [8,9]. In fact, metal-doped carbon materials have been successfully tested as electro-catalysts for CO2 reduction to hydrocarbons [10] as well as for catalysing the oxygen reduction reaction [11–13] and great efforts are being made to accomplish these electro-catalytic reactions with non-noble metals [14–18]. Among carbon materials, carbon gels present numerous advantages, starting with its purity, since they are obtained by carbonization of an organic precursor gel that develops a well-defined porosity during the gelation process [19], moreover, textural and morphological properties can be easily designed by modifying the experimental conditions [18,20–23]. On that basis, previous works, using carbon gels doped with transition metals as catalysts for CO2 electro-reduction, have been reported [15,24,25].

Taking into account this overview, it would be great to have poly-functional materials which can work as electro-catalysts in both applications. Therefore, the aim of the present work is to develop poly-functional reduction electro-catalysts based on non-precious metal and carbon gels for the electrochemical reduction of Oxygen, as well as CO2. Different carbon composites, xerogel-nanotubes and xerogel-nanohorns, doped with nickel were synthesized and tested as cathodes for both reactions. The

effect of porosity, conductivity and metal-carbon interaction was studied and discussed.

VI.2. Experimental

VI.2.1. Synthesis of supports

Three different types of carbon supports were prepared by sol-gel synthesis: pure carbon xerogel, carbon nanotubes (CNT) doped xerogel and carbon nanohorns (CNH) doped xerogel. The synthesis procedure is described below.

VI.2.1.1. Carbon xerogels (J and J-CTAB)

Carbon xerogels were prepared by a sol-gel process based on the resorcinol (R)-formaldehyde (F) polycondensation. In a typical procedure, the surfactant (S) is dispersed in 900 mL of n-heptane and heated at 65 °C under reflux and stirring (450 rpm). Once the temperature is stabilized, an aqueous solution (W) containing the corresponding amount of resorcinol (R), formaldehyde (F) and Sodium dodecylbenzenesulfonate (DBSS) is added drop-wise. (DBSS is added to facilitate the dispersion of carbon nanomaterials (CNT and CNH), in this case even when no carbon nanomaterials are present, DBSS was also added to maintain constant the synthesis conditions). The final molar ratio of the mixture was R/F=1/2, R/W=1/14, R/S=4.5 and R/DBSS=245.

The R-F hydrogel was cured at 65 °C for 24h under stirring, after that, the solid obtained was filtered and immersed in acetone (5 days, changing acetone twice daily) in order to remove all other traces of unreacted product as well as exchanging the solvent within the pores by acetone. This procedure prevent the porosity collapse during the subsequent drying process [26]. After that, the gel was filtered again and dried by microwave heating under Argon atmosphere for ranging periods of 1 minute at 300W until constant weight. The pyrolysis of organic xerogels, to obtain the

corresponding carbon xerogels, was carried out in a tubular furnace under pure N2 flow (300 cm^3/min) up to 900 °C with a heating rate of 1 °C/min and a dwell time of 2h.

In order to study the influence of the surfactant nature on the carbon xerogel morphology, two different surfactants were used: a non-ionic surfactant, Span 80 and a cationic surfactant, CTAB. The samples were referred as “J” and “J-CTAB” respectively.

VI.2.1.2. CNT and CNH-doped carbon xerogel (JT and JH)

The doping of carbon xerogels with carbon nanotubes and carbon nanohorns was carried out following the same procedure described above using Span80 as surfactant. So, the proper amount of CNT (MWCNTs 95% from Nanoamor Inc.) or CNH (SWCNHs, 90% from Sigma-Aldrich) to obtain 1 wt. % doped materials was added to the aqueous solution (W) containing the corresponding amount of resorcinol (R), formaldehyde (F) and sodium dodecylbenzenesulfonate (DBSS). This solution was sonicated for 30 min to allow a good dispersion of carbon nanomaterials in the mixture before the addition to the heptane solution.

VI.2.2. Synthesis of Ni-catalysts

Ni-catalysts were prepared by two different methods:

i) Method 1: by Ni-doping during sol-gel synthesis.
ii) Method 2: by impregnation of the prepared supports J, JT and JH with a Ni salt solution.

i) Method 1: Ni-doping during sol-gel synthesis

Ni-doping was performed following the same method used in the synthesis of the corresponding supports but adding the proper amount of nickel acetate to the R+F aqueous mixture. To adjust the final amount of Ni

(2.0 wt.%), it was supposed a weight loss of 50% during the carbonization [27].

Catalysts obtained were labelled as J-Ni1, JT-Ni1 and JH-Ni1 where 1 stands for the first method of doping.

ii) Method 2: Incipient wetness impregnation

Nickel catalysts were prepared by the incipient wetness impregnation technique. To do that, the appropriate amount of metallic precursor salt (Ni(OCOCH3)2·4H2O), to obtain a carbon catalyst doped with 2.0 wt. % Ni, was dissolved in the same volume of distilled water as the pore volume of the support. Supports J, JT and JH were impregnated and dried overnight at 120 °C. After that, samples were heated at 350 °C in N_2 flow for 2h in order to breakdown the metallic salt.

The samples thus obtained were labelled as J-Ni2, JT-Ni2 and JH-Ni2, where 2 stands for the second method of doping, impregnation.

Table VI.1. Composition and preparation method of supports and catalysts.summarize the information of synthesis of all materials obtained.

Table VI.1. Composition and preparation method of supports and catalysts.

Sample	Type	Preparation method	Composition (% wt.)
J	Support	Polycondensation R-F	Carbon xerogel
JT	Support	Polycondensation R-F	Carbon xerogel + 1% CNT
JH	Support	Polycondensation R-F	Carbon xerogel + 1% CNH
J-Ni1	Catalyst	Ni-doping during polycondensation R-F	Carbon xerogel + 2.0% Ni
JT-Ni1	Catalyst	Ni-doping during polycondensation R-F	Carbon xerogel + 1% CNT + 2.0% Ni
JH-Ni1	Catalyst	Ni-doping during polycondensation R-F	Carbon xerogel + 1% CNH + 2.0% Ni
J-Ni2	Catalyst	Polycondensation R-F + incipient wetness impregnation	Carbon xerogel + 2.0% Ni
JT-Ni2	Catalyst	Polycondensation R-F + incipient wetness impregnation	Carbon xerogel + 1% CNT + 2.0% Ni
JH-Ni2	Catalyst	Polycondensation R-F + incipient wetness impregnation	Carbon xerogel + 1% CNH + 2.0% Ni

VI.2.3. Textural and chemical characterization

The porous texture of all samples was analyzed by physical adsorption of N_2 at -196°C and CO_2 at 0°C, using a Quantachrome Autosorb-1 equipment. Before the gas adsorption, the samples were outgassed at 110°C overnight. BET and Dubinin-Radushkevich equations were applied to determine the apparent surface area (S_{BET}), the micropore volume (W_0) and the mean micropore width (L_0). Furthermore, the BJH method was applied to the desorption branch of the nitrogen isotherms to obtain the

mesopore volume of the samples (V_{mes}). The total pore volume ($V_{0.95}$) was considered as the volume of N_2 adsorbed at $P/P_0 = 0.95$.

The morphology was analyzed by scanning electron microscopy (SEM) and high-resolution transmission electron microscopy (HRTEM).

The total Nickel content was obtained by thermogravimetric analysis (TGA) using a Mettler-Toledo TGA/DSC1 thermobalance. TGAs were carried out under air atmosphere with a heating rate of 10ºC/min to 900ºC, once achieve that temperature it was held isothermal for 30 minutes. The amount of Ni was calculated from the ash.

XRD patterns were obtained using a Bruker D8 Advance X-ray diffractometer with Cu Kα radiation at a wavelength (λ) of 1.541 Å. The 2θ angles were scanned in the range 2θ from 20 to 70°. The Ni average crystal sizes (d) were estimated by the Debye-Scherrer equation.

The chemical characterization of catalysts was further analyzed by X-ray photoelectron spectroscopy (XPS). The spectra were obtained on a Kratos Axis Ultra-DLD X-ray photoelectron spectrometer equipped with a hemispherical electron analyzer connected to a detector DLD (delay-line detector).

VI.2.4. Electrochemical measurements

VI.2.4.1 Electrochemical characterization

The electrochemical characterization of all samples was carried out with a Biologic VMP Multichannel potentiostat using a three electrodes system. Carbon-based materials, a platinum wire and Ag/AgCl were used as cathode, counter electrode and reference electrode respectively. All the samples were characterized by Cyclic Voltammetries (CVs) and Electrochemical Impedance Spectroscopy (EIS).

In order to study the behaviour of each sample through the electrolyte containing or in absence of Oxygen, CVs were performed in O2-saturated 0.1M KOH solution or in a 0.1M KOH solution completely degasified (by bubbling N2). The sweeping voltage rate was 50mVs, from 0.4V to -0.8V while RDE was rotating at 1000rpm. The working electrode was conformed as described below in detail.

The Electrochemical Impedance Spectroscopy (EIS) measurements were performed with a three-electrode system using H_2SO_4 0.1M solution as electrolyte. EIS experiments were studied from a frequency of 1 mHz to 100 kHz with a sinusoidal signal amplitude of 10 mV. To perform EIS, the carbon electrodes were prepared by spreading a past onto a graphite sheet of 50 mm × 8 mm × 0.25 mm thick. That past was made with 80mg of carbon and 10 wt.% of polytetrafluoroethylene 60%wt. (PFTEE), used as binder.

VI.2.4.2 Oxygen reduction reaction (ORR)

The oxygen reduction reaction was carried out in a standard three-electrode cell with a Pt wire as the counter electrode, Ag/AgCl as reference electrode and the Rotating Disk Electrode (RDE) Metrohm AUTOLAB RDE-2 with a 3mm Glassy Carbon tip fitted with the carbon materials as the working electrode.

To prepare the electrocatalysts, 5mg of carbon were dispersed in 1mL of a solution previously prepared which contains Nafion (5%) and water in a 1:9 (v:V) ratio and sonicated for 30 min until a homogeneous and stable ink was obtained; after that, 10 µL of this ink were loaded on RDE tip and dried under infrared radiation. The Glassy Carbon tip had been previously polished with alumina powder. Afterwards, Linear Sweep Voltammetries (LSVs) were measured in an O_2-saturated 0.1M KOH solution at different rotation rates from 500 rpm to 3000 rpm. The experiments were conducted from 0.4V to -0.8V (Ag/AgCl) at a sweep rate of 5 mVs^{-1}.

The experimental data were fitted to the Koutecky-Levich model in order to evaluate the electrocatalytic performance of samples and to calculate the number of electrons transferred for each of them [28].

VI.2.4.3 CO_2 electro-reduction

The electro-catalytic conversion of CO_2 was carried out in a three-electrode cell of 300 cm^3 of capacity at room temperature and pressure. A Biologic VMP multichannel potentiostat was used to perform the electrochemical measurements. A platinum wire and saturated Ag/AgCl were employed as the counter and reference electrode respectively while 0.1M potassium bicarbonate aqueous solution (150 cm^3) was used as electrolyte. The working electrode (cathode) was prepared as it was referenced in our previous works [15,24], briefly, 80 mg of catalyst was mixed with PTFE (60% wt. suspension) and homogeneously pasted on a graphite sheet. After that, the electrode was immersed in 0.1M KHCO3 overnight.

The setup was working in potentiostatic mode at -1.6 V, reproducing the voltage conditions of previous works [29]. Before the electrocatalytic reduction of CO_2, the solution containing the electrolyte was saturated with CO_2 by bubbling through for 3h. Once the solution is saturated, the gas inlet closes off and the cell operates in batch mode. All electrocatalysts were also tested in a CO2-free solution (by bubbling Ar).

All samples were characterized by Linear Sweep Voltammetry (LSV) from 0 V to -2 V (vs. Ag/AgCl) with a sweeping rate of 5mV/s using the same experimental conditions and reactor set-up as those for the CO_2 electrocatalytic conversion.

The gas phase of the reactor was analyzed by gas chromatography (GC), where gases were directly injected into the GC column using a gas recirculating pump for low flows. The GC was equipped with a FID detector

and Chrompack Poraplot Q column (50 m × 0.53 mm) with He as the carrier gas.

The gaseous products distribution is expressed in terms of the carbon selectivity as the amount of carbon (from CO2) in a specific product relative to the total amount of carbon in the detected hydrocarbons, and it was calculated by equation (1), where n_{Ci} represents the number of moles of product Ci, and *i* the number of carbon atoms in that product.

$$S_{C_i}\ (\%) = \frac{i \cdot n_{C_i}}{\sum_i i \cdot n_{C_i}} \times 100\% \qquad (1)$$

VI.3. Results and discussion

VI.3.1. Textural and chemical characterization

Notable textual and morphological differences (Figure VI.1a, VI.Figure **VI.2**a and VI.Figure **VI.2**b) are observed comparing samples prepared with different surfactants (J and J-CTAB). The use of Span80 (J) results in nanometric spheres while the presence of CTAB produces non-spherical structures with large amount of macropores (Figure VI.2). Isotherms of both samples (Figure VI.1a) are completely different, while J-CTAB shows a type I isotherm, typical of microporous materials, J presents a hybrid I-IV type isotherm typical of micro-mesoporous samples. After these observations, Span80 was selected as surfactant to prepare the rest of samples in order to obtain mesoporous carbon nanospheres.

The N_2 adsorption isotherms at -196 ºC of carbon xerogel supports and Ni-doped carbon xerogels are also shown in Figure VI.1b and VI.1c, respectively. All samples show type I-IV hybrid isotherms according to the IUPAC classification, typical of micro-mesoporous materials. The doping with carbon nanotubes and carbon nanohorns does not significantly affect

the textural properties of the final carbon xerogels (Figure VI.1b and VI.1c) within each series (J*X* or J*X*-Ni1). However, Ni-doping affects the morphology and consequently, the textural properties of samples (Figure VI.1d).

Analyzing SEM and TEM images (Figure VI.2 and Figure VI.4b, VI.4c) it was found that the addition of Ni by the first method increases the nanospheres average size (174.0 vs 433.4 nm for J to J-Ni1, 177.2 vs. 388.1 nm for JT to JT-Ni1 and 213.7 vs 302.5 nm for JH to JH-Ni1, respectively) (Table VI.2). Whereas, the incipient impregnation and the subsequent thermal treatment at 350ºC do not affect significantly the sphere size. These size differences affect the textural properties increasing the surface area due mainly to the increase of the mesopore volume (Table VI.2). It is well known that carbon xerogels are formed by interconnected primary particles where the microporous structure is mainly due to pores inside these primary particles while meso and macroporous are related with the interparticle voids, as consequence, the higher the primary particle size, the higher the mesopore size [30]. In that case, as can be observed in SEM and TEM images (Figure VI.2 and Figure VI.4b, VI.4c), isolated carbon nanospheres are obtained, so that, no mesopores are expected, however, a significant volume of mesopores are obtained by gas adsorption which increases with the nanosphere size (Figure VI.3). This fact manifests that mesopores are localized inside the nanospheres. As denoted TEM images (Figure VI.2 and Figure VI.4), nanospheres are formed in their turn by the fusion of primary particles of few nm leaving mesopores between them. As it is described above, if mesopores were due to the fusion of nanospheres, higher mesopore size would be expected in Ni-doped series because of the higher nanospheres size, but the opposite trend is obtained; lower mesopore size (7.5 vs 12.8 nm) at higher nanospheres size (433.4 vs 174.0 nm, respectively) which corroborates that mesopores are localized inside the nanospheres. So, micro-mesoporous carbon nanospheres are obtained by a simply sol-gel method.

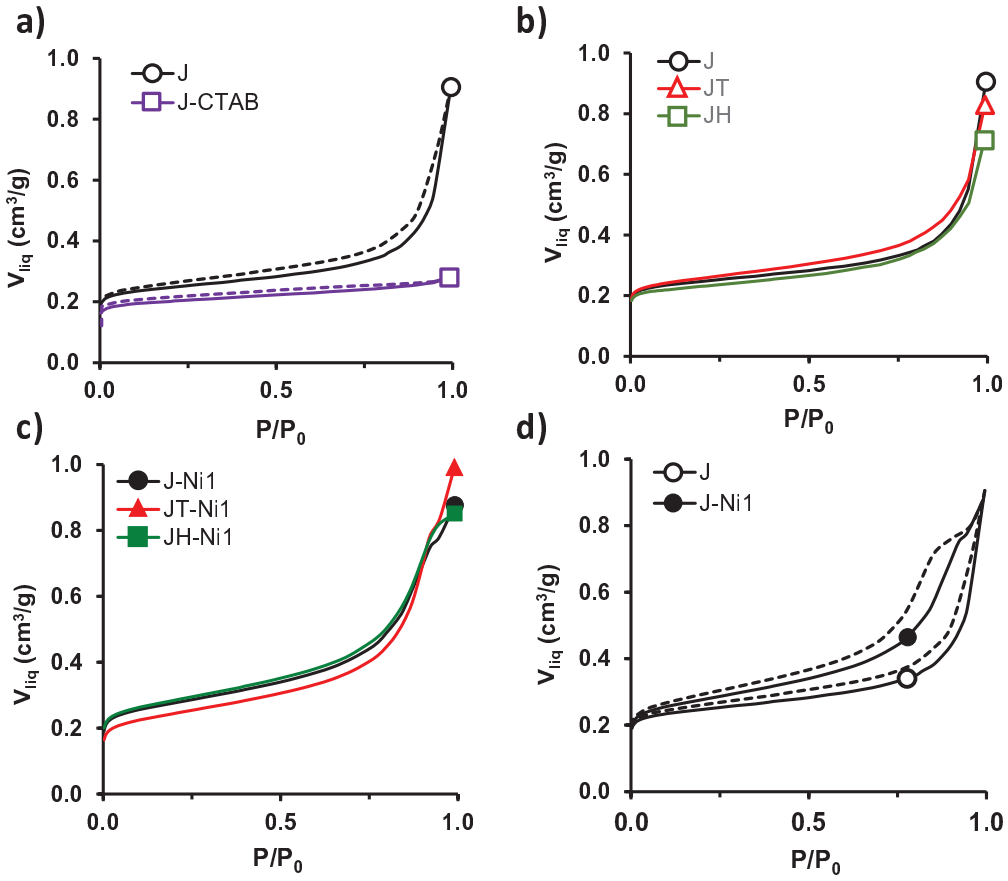

Figure VI.1. N_2-adsorption/desorption isotherms of support and catalysts: a) effect of surfactant nature: J (○) and J-CTAB (□), b) effect of CNT or CNH doping on supports: J (○), JT (△) and JH (□), c) effect of CNT or CNH doping in doped catalysts: J-Ni1 (●), JT-Ni1 (▲) and JH-Ni1 (■), and d) effect of Ni presence: J (○) and J-Ni1 (●) on textural properties.

A more in-depth analysis of Table VI.2 allows us to state the issues discussed above. Furthermore, W_0 (N_2) < W_0 (CO_2) indicates the presence of some diffusional limitations at the entrance of the narrowest micropores in supports samples. This difference is more significant in J-CTAB sample, due to the presence of narrow micropores and the absence of mesoporosity. However, W_0 (N_2) > W_0 (CO_2) in Ni-doped samples which manifests the contribution of the widest micropores and mesopores to the N_2 adsorption capacity at -196 ºC. Notably, Ni-doped samples (prepared by method 1)

present wider micropores (L_0 (N_2) ~ 1.10 nm) than their respective supports (L_0 (N_2) ~ 0.80 nm) and a significant increase in mesopore volume is produced as well. So, it may be said that Ni influences the R-F polymerization given samples with a larger amount of mesopores and wider microporosity.

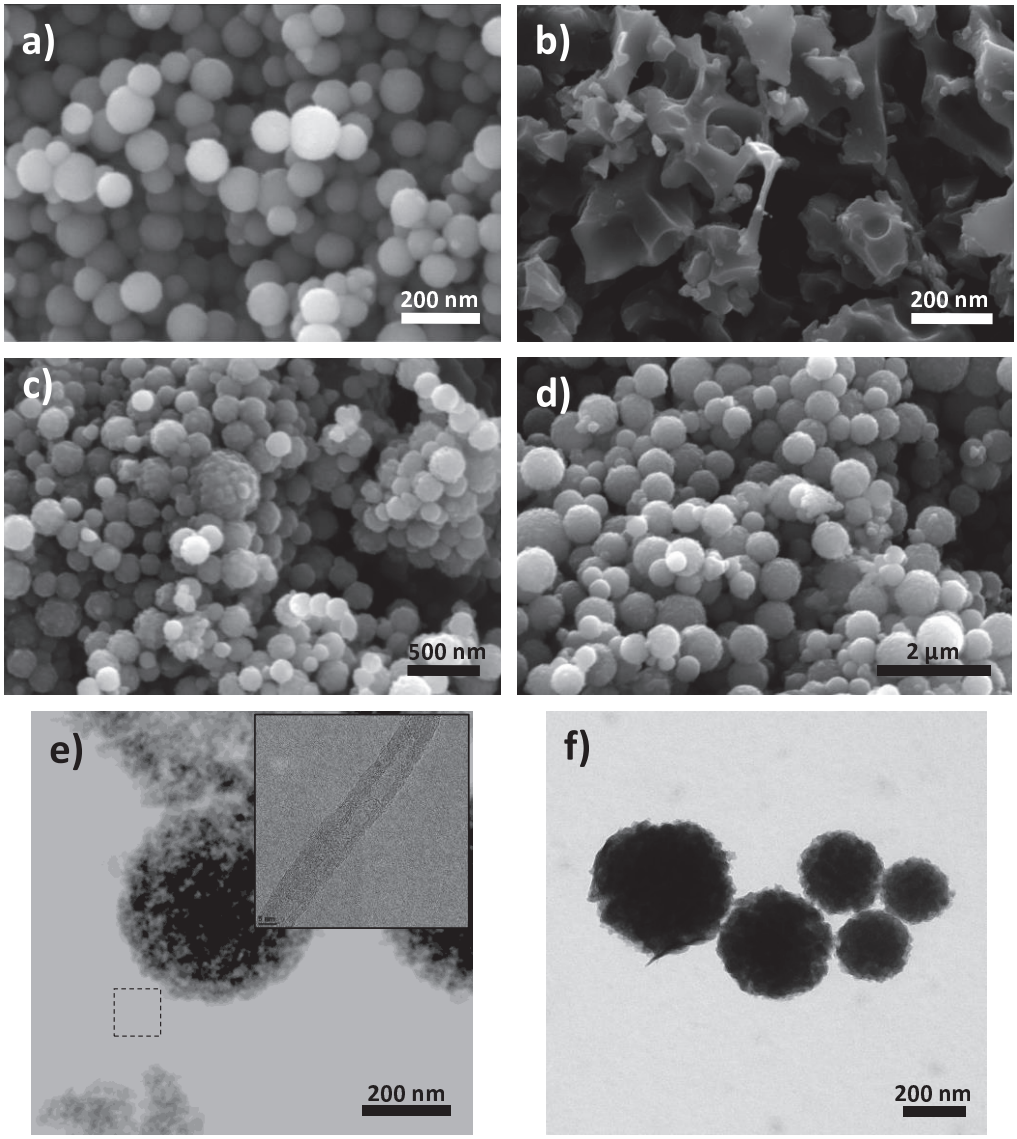

Figure VI.2. SEM images of the samples: a) J; b) J-CTAB; c) JH; d) JH-Ni1 and TEM images of e) JT, f) JH

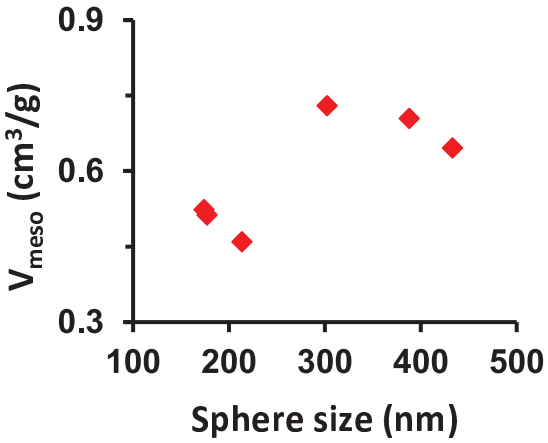

Figure VI.3. Relationship between the nanospheres size and the mesopore volume.

Table VI.2. Textural properties and spheres average size (Ds)

Sample	S_{BET}	W_0 (N_2)	W_0 (CO_2)	L_0 (N_2)	L_0 (CO_2)	$V_{0.95}$	V_{BJH}	d_{meso}	D_s
	$m^2 \cdot g^{-1}$	$cm^3 \cdot g^{-1}$	$cm^3 \cdot g^{-1}$	nm	nm	$cm^3 \cdot g^{-1}$	$cm^3 \cdot g^{-1}$	nm	nm
J	599	0.238	0.263	0.87	0.62	0.555	0.524	15.3	174.0
J-CTAB	495	0.195	0.254	0.72	0.59	0.263	0.084	2.8	-
JT	617	0.232	0.252	0.79	0.59	0.583	0.513	12.8	177.2
JH	560	0.224	0.266	0.81	0.58	0.506	0.460	15.4	213.7
J-Ni1	655	0.257	0.236	1.06	0.61	0.778	0.646	7.5	433.4
JT-Ni1	574	0.24	0.208	1.28	0.58	0.85	0.705	9.0	388.1
JH-Ni1	672	0.264	0.229	1.05	0.6	0.537	0.730	7.5	302.5
J-Ni2	500	0.200	0.231	1.1	0.45	0.481	0.437	16.8	168.7
JT-Ni2	539	0.218	0.263	1.21	0.59	0.541	0.465	14.0	188.1
JH-Ni2	474	0.194	0.222	1.22	0.57	0.454	0.438	14.0	214.1

The metal phase was characterized by TGA, XRD and XPS.

The total Ni amounts obtained by TGA are summarized in Table VI.3. The amount of Ni, as it was to be expected, was around 2.0 wt. % with small variations due to the real carbonization loss was slightly higher than 50 %.

The content and crystal size of the metallic phase were also characterized and collected in Table VI.3. X-ray diffraction (Figure VI.4a) shows two broad peaks for all samples at 2θ values ~25° and ~44° corresponding to (002) and (100) planes of graphite in accordance with JCPDS card 89-8487, therefore, it demonstrates that these carbon xerogels are materials with a high development degree of graphitic clusteres. Furthermore, J*X*-Ni1 samples show two additional peaks at 2θ= 44.5° and 51.8° which correspond to (111) and (200) planes of Ni^0 respectively, so carbon matrix maintains Ni in 0 oxidation state. However, no metal diffraction peaks are obtained for J*X*-Ni2, it is attributed to Ni incipient impregnation provokes too small crystallite sizes (below 3 nm) [31].

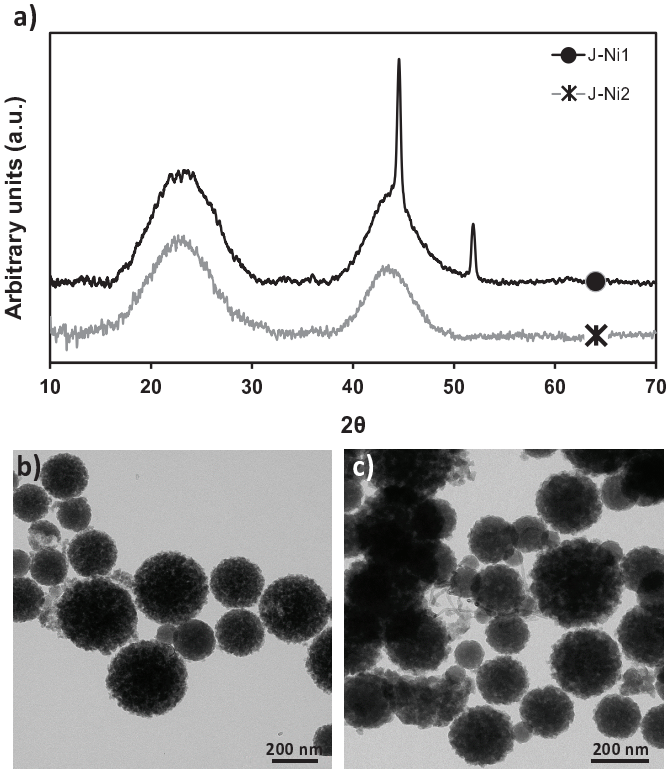

Figure VI.4. a) XRD of impregnated (✱) and doped (●) Ni-catalysts. TEM images of b) JH-Ni1 and c) JT-Ni2.

The surface chemistry of support and catalysts was analysed by X-ray Photoelectron Spectroscopy (XPS). Results are collected in Table VI.3. Similar deconvolution of Oxygen and Carbon regions was obtained for supports and Ni-xerogels doped by the first method (*JX* and *JX*-Ni1 series), which denotes a similar chemical nature of their surfaces. However, no XPS peaks of Ni were obtained in *JX*-Ni1 materials, this fact clearly supports the discussion above mentioned, Ni-particles are mainly embedded into the carbonaceous matrix. On the other hand, analysing Ni-impregnated catalysts (J*X*-Ni2 series), around 9.5% of Ni was obtained for all impregnated samples.

Besides, Ni_{XPS} (%) > Ni loading (2.0%) indicating higher Ni-concentration on the external surface.

Table VI.3. Chemical composition determined by XPS and TGA; and the average crystal size by XRD.

Sample	C_{XPS} %wt	O_{XPS} %wt	Ni_{XPS} %wt	Ni_{TGA} %wt	dp_{XRD} (nm)
J	96.3	3.7	0.0	-	-
JT	94.6	5.4	0.0	-	-
JH	94.9	5.1	0.0	-	-
J-Ni1	94.1	5.9	0.0	2.11	22.95
JT-Ni1	94.2	5.8	0.0	2.61	28.95
JH-Ni1	94.3	5.7	0.0	2.14	27.25
J-Ni2	73.0	18.7	8.3	1.97	-
JT-Ni2	73.1	16.3	10.5	2.00	-
JH-Ni2	73.8	16.6	9.7	2.29	-

VI.3.2. Electrochemical measurements

VI.3.2.1. Impedance Spectroscopy (EIS)

The Impedance Spectroscopy was measured in order to investigate the resistance of the materials through the electrolyte (H2SO4 0.1M). Taking into account that all measurements were performed in the same conditions, the found results are attributed to the differences among each sample for comparison purposes.

Figure VI.5 shows the Nyquist plot for electro-catalysts obtained by incipient wetness impregnation. The presence of the semicircle reveals good electrical conductivity at the electrode−electrolyte interface [32]. The high frequency intercept on the Z' axis represents the sum of the resistances arising from the electrolyte, the intrinsic resistance of the carbon active material, and the contact resistance between the active material and the current collector [32]. So, the larger semicircle for J-Ni2 implies a notably higher resistance meanwhile the presence of carbon nanotube and carbon nanohorns greatly decreases the resistance, especially in the case of carbon nanohorns.

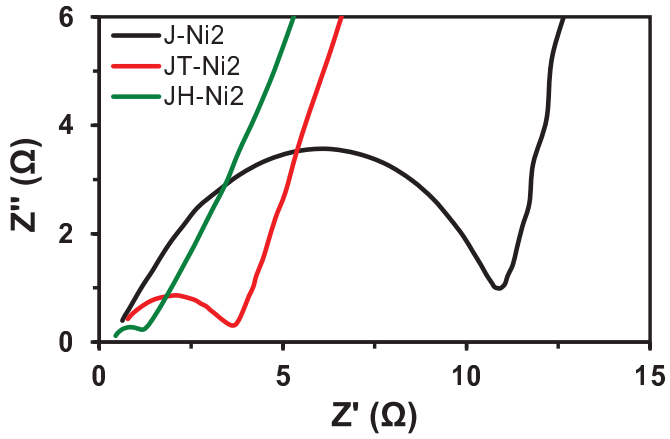

Figure VI.5. Nyquist plot of Electrochemical Impedance Espectroscopy (EIS)

VI.3.2.2. Oxygen Reduction Reaction: CV and LSV

Cyclic Voltammetry (CV) curves were obtained while N_2 or O_2 were bubbling through 0.1 M KOH solution. CVs were measured at a rotation rate of 1000 rpm and at a scan rate of $50mV \cdot s^{-1}$. As discussed in previous sections, textural and chemical properties in each series are very close, and consequently, the different electrochemical behaviour must be related with the presence of Ni or nanomaterials. In such a manner, Figure VI.6a and VI.6b depict the CVs in N_2 of supports and their corresponding Ni-doped catalysts. An increase in capacitance is obtained following the order J<JH<JT and J-Ni1<JH-Ni1<JT-Ni1. This improvement in storage capacity by adding nanomaterials can be attributed to the improvement of the conductivity of the samples, since the textural and chemical properties are very close.

In order to analyze the influence of the presence of nickel as well as the Ni-catalysts preparation (method 1 or method 2), JT, JT-Ni1 and JT-Ni2 CVs are shown in Figure VI.6c. A significant improvement in the storage capacity of the material is obtained using Ni-catalysts instead the support. Comparing JT with JT-Ni2 (same support and similar tectural properties) it can be said that this higher intensity can be achieved thanks to the improvement in electrical conductivity caused by nickel particles. On the other hand, comparing JT-Ni2 and JT-Ni1 samples, an improved capacity is obtained when the doping method is used instead of the impregnation one. These observations are also consistent with the textural changes after doping (greater area and higher volume of micro and mesopores).

Comparing CVs in N_2 and O_2, differences are observed in the negative potential region for all samples (as example Figure VI.6d) which already predict activity in the oxygen electro-reduction reaction.

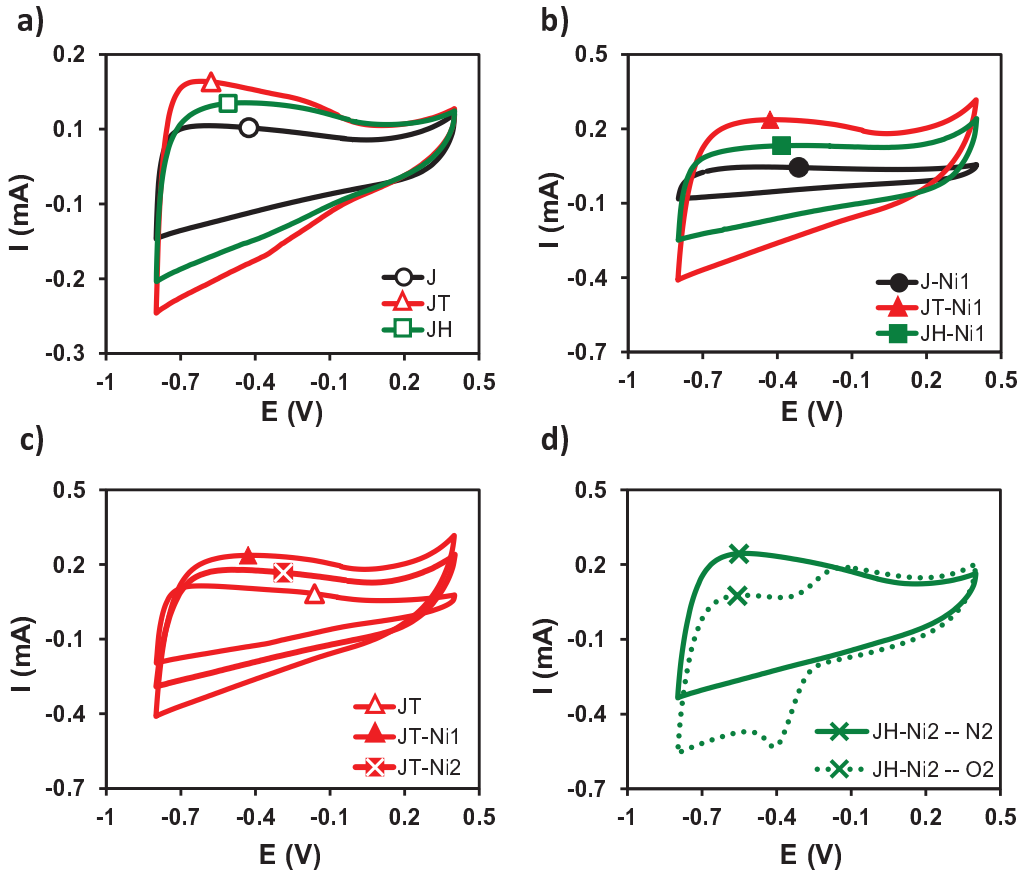

Figure VI.6. a), b) and c) Cyclic Voltammetry (CV) curves in N_2 of a) Supports: J (○) JT (△) JH (□), b) Ni-catalysts doped by the first method: J-Ni1 (●) JT-Ni1 (▲) and JH-Ni1(■), c) Series with CNTs: JT (△), JT-Ni1 (▲) and JT-Ni2 (⊠) and d) CVs in N2 (—) and O_2 (···) of JH-Ni2 catalyst.

Data obtained from LSVs were fitted to the K-L model in order to evaluate the electro-catalytic behaviour. Two main ORR pathways are defined in basic media: *via* two-electrons (eq. 3) or *via* four-electrons (eq. 4):

$$O_2 + H_2O + 2e^- \rightarrow HO_2^- + OH^- \quad (3)$$

$$O_2 + 2H_2O + 4e^- \rightarrow 4OH^- \quad (4)$$

It would be desirable for ORR to take place by the 4-electrons pathway rather than the 2-electrons pathway, since the former implies higher current densities on the electrochemical cell and the latter leads to the formation of peroxide species that worsen the catalytic efficiency. Therefore, it is crucial to determine whether ORR catalysts are leading the reaction by the one or the other mechanism. Thus, LSV curves were obtained at different RDE rotation rates for all samples (as example Figure VI.7a) and data were fitted to K-L equation in order to study the kinetics, the number of electron transferred and the onset potential (Figure VI.7 and Table VI.4). K-L plot at different potentials is displayed in Figure VI.7b where linear regressions exhibits good linearity and all lines are nearly parallels to each other, suggesting that they all have the similar values of B ($0.2nF(D_{O_2})^{2/3}\upsilon^{-1/6}C_{O_2}$). As we know the D_{O2}, C_{O2}, ν and F, the electron-transfer number, n, is calculated (Table VI.4) Furthermore, from K-L intercepts at different electrode potentials, the kinetic current density (J_k) is obtained.

Data from Table VI.4 show that the doping with nanomaterials, CNT and CNH, clearly improve the electro-catalytic performances, especially in the case of CNH doping; it could be attributed to the greater enhancement of the electrical conductivity (Figure VI.5). However, the pure 4-electrons pathway is not achieved until Ni-doping is included, what is more, only samples doped with both, Ni and CNH or CNT, are able to reduce oxygen to HO- by the direct mechanism. This improvement evidences a synergistic effect between carbon nanostructures and Ni particles which had already shown activity in this reaction [16].

It is also worth noting that free-metal samples display an outstanding and unexpected electro-catalytic activity, since all of them can carry out the oxygen reduction reaction, simply do not do by 4-electrons, but they do it by “3-electrons” pathway (mixing pathway between 2 and 4 electrons), which implies 50% production of hydrogen peroxide.

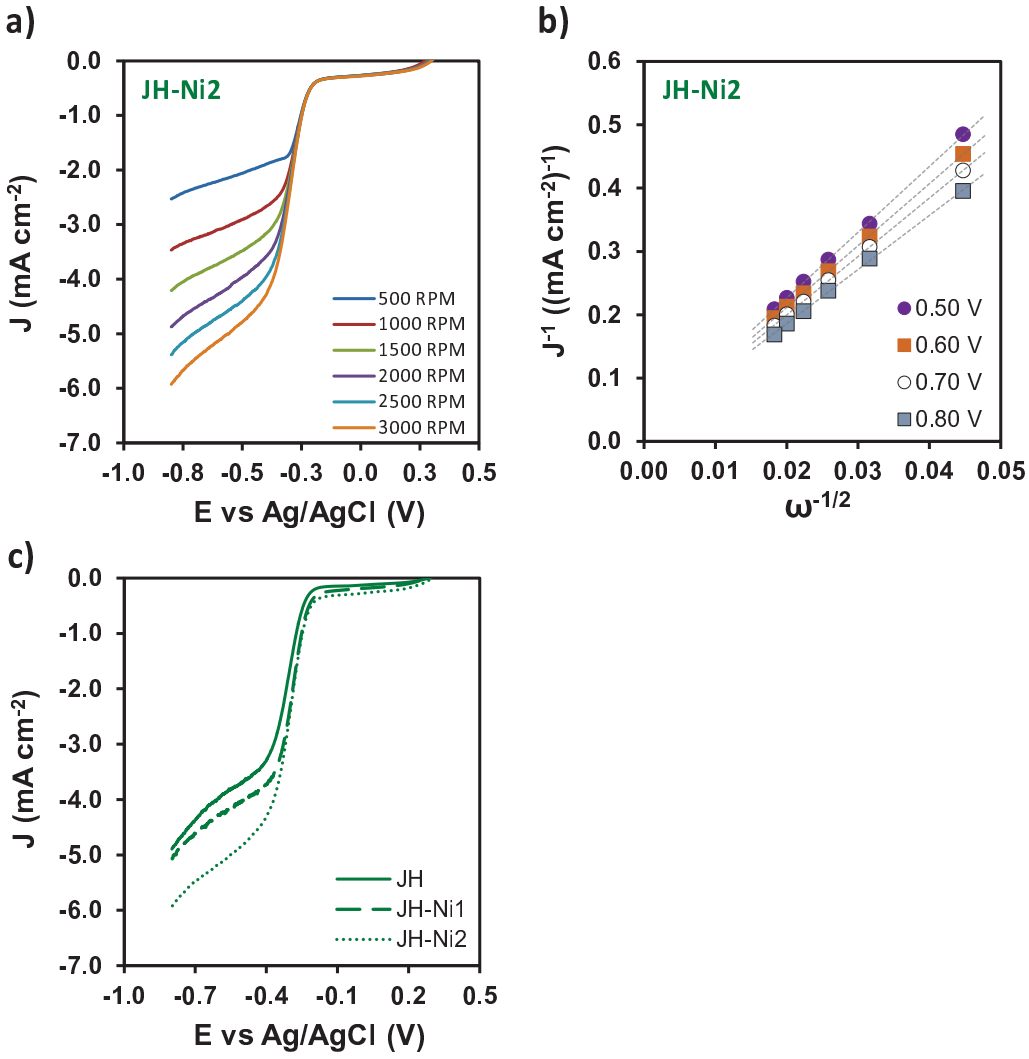

Figure VI.7. a) LSV at different rotation rate for JH-Ni2; b) K-L plot of JH-Ni2 obtained from a); c) Comparison of LSV at 3000 rpm for support and Ni-doped samples of JH series.

Analysing the electrochemical differences between Ni-doped catalysts obtained by the two different methods (1 or 2), it was found that, overall, the Ni-impregnation method (2) accomplish better performances respecting to kinetics, inasmuch as they present higher kinetic current density (j_k), slightly lower onset potential ($E°_{onset}$) and higher electrons transferred as well. Such finding goes hand in hand with their textural and chemical characterization: despite the porosity is slightly reduced by the

incipient impregnation, this method allows a more accessible metallic phase, Ni is mainly on the surface of the spheres where the electrolyte easily permeates. Furthermore, Ni-particles are smaller and so, more and better scattered through the matrix which contributes to improving the electro-catalytic activity.

By contrast, in J*X*-Ni1 materials, Ni particle size is bigger and particles are mainly embedded into the carbon matrix, so fewer active centres are accessible for oxygen.

Table VI.4. Electrochemical parameters obtained from the RDE experiments (values of jk and n are referred to K-L fitting for data at -0.8V).

sample	j_k	$E°_{onset}$	n
J	21.6	-0.23	3.2
JT	10.3	-0.24	2.9
JH	24.0	-0.24	3.5
J-Ni1	6.15	-0.21	2.4
JT-Ni1	17.7	-0.21	2.9
JH-Ni1	13.0	-0.22	4.2
J-Ni2	17.7	-0.22	2.9
JT-Ni2	13.0	-0.23	4.2
JH-Ni2	67.1	-0.23	3.3

In any case, both, carbon nanomaterials and Ni, clearly improve the electro-catalytic performance of carbon xerogels in ORR although both types of improvements are not always equally linear, which suggest that other factors have also significant influence on this reaction as the electrical conductivity or the textural properties in relation with the accessibility of the electrolyte to the Ni nanoparticles or to the carbon nanomaterials, but this last point is very difficult to assess.

VI.3.2.2. CO_2 electro-reduction to hydrocarbons.

All samples were tested as cathode in the CO_2 electro-catalytic reduction reaction to hydrocarbons. The total hydrocarbons molar production (hydrocarbons from C1 to C4) and faradaic efficiency (F.E) are summarized in Table VI.5.

All materials have shown electro-catalytic activity, all of them have been able to reduce CO_2 to hydrocarbons, even supports, which do not have metal. However, surprisingly, J*X*-Ni1 series have not improved the activity with respect to the supports, these six materials have almost produced the same amount of hydrocarbons remaining in any case below 20 ppm. The small differences between each other could be justified by the differences in textural properties (Table VI.2). However, the reason why this series (J*X*-Ni1) has not better activity than their corresponding supports is that in these cases Ni is embedded into the carbon matrix in such a way metal phase is not accessible to the electrolyte, so the CO_2 dissolved cannot permeate to the metal particles, as we have discussed in previous sections. On the other side, these results show that the carbon nanomaterials doping does not improve the electro-activity of the carbon xerogels in this reaction. Moreover, only Ni phases, when these are clearly accessible to the electrolyte, are really working well as active sites.

Therefore, the incipient Ni-impregnation leads to an improvement of activity by over an order of magnitude regarding the total production of hydrocarbons. It's worth recalling that these samples have the metal phase mainly on the surface of the spheres so Nickel is completely exposed to the electrolyte and so, to the CO_2 dissolved. Thereby, the most active electro-catalyst was JH-Ni2, the one doped with CNH, while the most efficient was JT-Ni2, doped with CNT. These results are consistent with the fact that JT-Ni2 possesses the largest amount of surface Ni while JH-Ni2 contents the highest Ni total percentage in addition to being the most conductive material.

Table VI.5. Total production of hydrocarbons (ppm) and faradaic efficiency after 200 minutes.

Sample	Nickel	HC (ppm)	Faradaic Efficiency (%)
J	No	13	-
JT	No	18	-
JH	No	13	-
J-Ni1	yes	8	-
JT-Ni1	yes	11	-
JH-Ni1	yes	9	-
J-Ni2	**yes**	**90**	**0.3**
JT-Ni2	**yes**	**91**	**0.6**
JH-Ni2	**yes**	**117**	**0.3**

The apparent faradaic efficiency is in good agreement with data displayed in Figure VI.8, nevertheless it should be noted that only hydrocarbons from C1 to C4 were taken into consideration to calculate the F.E. but also Hydrogen and Oxygen were produced and are not being considered.

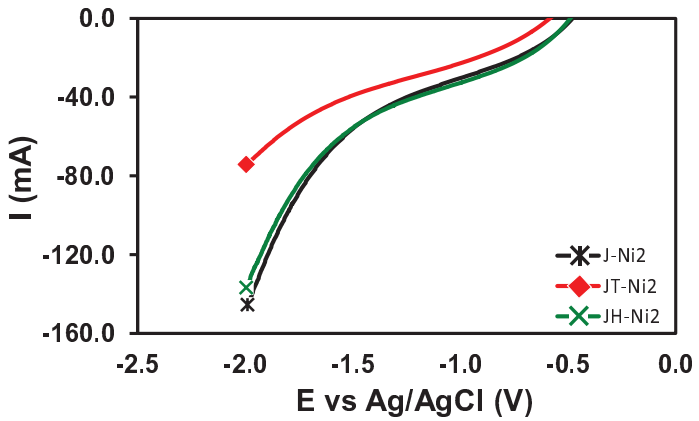

Figure VI.8. LSV at 5 mV/s of samples obtained by incipient Ni-impregnation in 0.1M KHCO3 saturated with CO_2.

After analyzing the results, it was not found any trend between the catalysts obtained by incipient impregnation (J*X*-Ni2 series) and their respective supports (J*X* series), so the differences between each other might be related with the Ni particle size [33] as well as its distribution and accesibility on the surface of the spheres.

Figure VI.9a shows a clear trend for all materials, the selectivity to hydrocarbons is always following C1 > C2 > C3 > C4, along the same line than other catalysts based on Ni reported in bibliography [34]; besides, methane is the main product detected. To end with, Figure VI.9b manifests that selectivity remains constant during the reaction time once the kinetic equilibrium has been achieved.

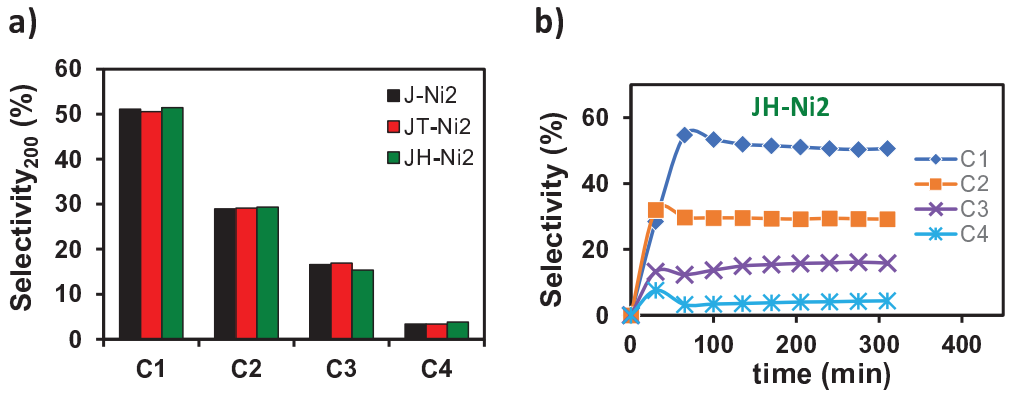

Figure VI.9. Product distribution (%) in terms of selectivity for: a) JX-Ni2 samples after 200 min; b) JH-Ni2 against the reaction time.

VI.4. Conclusions

Mesoporous carbon spheres doped with CNT or carbon CNH were obtained by sol-gel synthesis through polycondensation of resorcinol and formaldehyde. The addition of these carbon nanomaterials (nanotubes or nanohorns) has not interfered with the polymerization process since materials with similar properties have been obtained. However, the Ni doping by the first method (during the gelation process) does affect the

textural properties, especially the volume of mesopores, which bears a good relationship with the spheres size, the bigger the sphere the higher the mesoporous volume.

The presence of these nanomaterials substantially increases the electrical conductivity and so the electrochemical measurements related with this aspect have been clearly improved. All materials, even the metal-free materials, present electro-catalytic activity in both reactions, oxygen and carbon dioxide electro-reduction. While doping with carbon nanomaterials clearly improve the electro-activity of carbon xerogels in ORR even being good free-metal electro-catalysts, this doping does not improve for themselves the electro-activity of carbon xerogels in CO_2 reduction. On the other hand, the presence of Ni phases enhances the electro-activity of carbon xerogels in both reactions, however, in the case of CO_2 reduction, a good accessibility of Ni particles to the electrolyte not only is more relevant but necessary. It should be remarked that these xerogels, all of them, have very low contents of, both, carbon nanomaterials and Ni, however the electro-catalytic results obtained in the best cases for each application are enoughly good and they are in the same line that those available in the literature based in carbon materials. Finally, the presence of mesopores in the catalysts has been always shown as a positive factor in both electro-reduction reactions.

VI.5. References

[1] International Energy Agency, Global Energy & CO2 Status Report, (n.d.). https://www.iea.org/geco/ (accessed 22 January 2019).

[2] International Energy Agency, CO2 Emissions, (n.d.). https://www.iea.org/statistics/co2emissions/ (accessed 22 January 2019).

[3] N.H. Behling, Chapter 2 - Fuel Cells and the Challenges Ahead, in: N.H. Behling (Ed.), Fuel Cells, Elsevier, 2013: pp. 7–36. doi:https://doi.org/10.1016/B978-0-444-56325-5.00002-8.

[4] B. Suddhasatwa, Recent trends in fuel cell science and technology, 2007.

[5] M. Winter, R.J. Brodd, What Are Batteries, Fuel Cells, and Supercapacitors?, Chem. Rev. 104 (2004) 4245–4270. doi:10.1021/cr020730k.

[6] C. Sealy, The problem with platinum, Mater. Today. 11 (2008) 65–68. doi:10.1016/S1369-7021(08)70254-2.

[7] L. Zhang, J. Zhang, D.P. Wilkinson, H. Wang, Progress in preparation of non-noble electrocatalysts for PEM fuel cell reactions, J. Power Sources. 156 (2006) 171–182. doi:10.1016/J.JPOWSOUR.2005.05.069.

[8] B.C. Marepally, C. Ampelli, C. Genovese, F. Tavella, L. Veyre, E.A. Quadrelli, S. Perathoner, G. Centi, Role of small Cu nanoparticles in the behaviour of nanocarbon-based electrodes for the electrocatalytic reduction of CO2, J. CO2 Util. 21 (2017) 534–542. doi:10.1016/J.JCOU.2017.08.008.

[9] F.J. Maldonado-Hódar, C. Moreno-Castilla, A.F. Pérez-Cadenas, Surface morphology, metal dispersion, and pore texture of transition metal-doped monolithic carbon aerogels and steam-activated derivatives, Microporous Mesoporous Mater. 69 (2004) 119–125. doi:10.1016/J.MICROMESO.2004.02.001.

[10] G. Centi, S. Perathoner, G. Winè, M. Gangeri, Electrocatalytic conversion of CO2 to long carbon-chain hydrocarbons, Green Chem. 9 (2007) 671–678. doi:10.1039/b615275a.

[11] K. Jayasayee, J.A.R. Van Veen, T.G. Manivasagam, S. Celebi, E.J.M.

Hensen, F.A. de Bruijn, Oxygen reduction reaction (ORR) activity and durability of carbon supported PtM (Co, Ni, Cu) alloys: Influence of particle size and non-noble metals, Appl. Catal. B Environ. 111–112 (2012) 515–526. doi:10.1016/J.APCATB.2011.11.003.

[12] E. Higuchi, H. Uchida, M. Watanabe, Effect of loading level in platinum-dispersed carbon black electrocatalysts on oxygen reduction activity evaluated by rotating disk electrode, J. Electroanal. Chem. 583 (2005) 69–76. doi:10.1016/J.JELECHEM.2005.01.041.

[13] J. Marie, S. Berthon-Fabry, P. Achard, M. Chatenet, A. Pradourat, E. Chainet, Highly dispersed platinum on carbon aerogels as supported catalysts for PEM fuel cell-electrodes: comparison of two different synthesis paths, J. Non. Cryst. Solids. 350 (2004) 88–96. doi:10.1016/J.JNONCRYSOL.2004.06.038.

[14] A. Gabe, J. García-Aguilar, Á. Berenguer-Murcia, E. Morallón, D. Cazorla-Amorós, Key factors improving oxygen reduction reaction activity in cobalt nanoparticles modified carbon nanotubes, Appl. Catal. B Environ. 217 (2017) 303–312. doi:10.1016/J.APCATB.2017.05.096.

[15] J. Castelo-Quibén, A. Abdelwahab, M. Pérez-Cadenas, S. Morales-Torres, F.J. Maldonado-Hódar, F. Carrasco-Marín, A.F. Pérez-Cadenas, Carbon - iron electro-catalysts for CO2 reduction. The role of the iron particle size, J. CO2 Util. 24 (2018) 240–249. doi:10.1016/j.jcou.2018.01.007.

[16] A. Abdelwahab, J. Castelo-Quibén, J.F. Vivo-Vilches, M. Pérez-Cadenas, F.J. Maldonado-Hódar, F. Carrasco-Marín, A.F. Pérez-Cadenas, Electrodes based on carbon aerogels partially graphitized by doping with transition metals for oxygen reduction reaction, Nanomaterials. 8 (2018). doi:10.3390/nano8040266.

[17] C. Genovese, C. Ampelli, S. Perathoner, G. Centi, Electrocatalytic conversion of CO<inf>2</inf> on carbon nanotube-based electrodes for producing solar fuels, J. Catal. 308 (2013) 237–249. doi:10.1016/j.jcat.2013.08.026.

[18] F.J.F.J. Maldonado-Hódar, H. Jirglová, A.F.A.F. Pérez-Cadenas, S.

Morales-Torres, Chemical control of the characteristics of Mo-doped carbon xerogels by surfactant-mediated synthesis, Carbon N. Y. 51 (2013) 213–223. doi:10.1016/j.carbon.2012.08.046.

[19] R.W. Pekala, C.T. Alviso, F.M. Kong, S.S. Hulsey, Aerogels derived from multifunctional organic monomers, J. Non. Cryst. Solids. 145 (1992) 90–98. doi:10.1016/S0022-3093(05)80436-3.

[20] E. Bailón-García, F. Carrasco-Marín, A.F. Pérez-Cadenas, F.J. Maldonado-Hódar, Microspheres of carbon xerogel: An alternative Pt-support for the selective hydrogenation of citral, Appl. Catal. A Gen. 482 (2014) 318–326. doi:10.1016/j.apcata.2014.06.011.

[21] A. Elmouwahidi, E. Bailón-García, A.F. Pérez-Cadenas, F.J. Maldonado-Hódar, J. Castelo-Quibén, F. Carrasco-Marín, Electrochemical performances of supercapacitors from carbon-ZrO2 composites, Electrochim. Acta. 259 (2018) 803–814. doi:10.1016/J.ELECTACTA.2017.11.041.

[22] J.F. Vivo-Vilches, F. Carrasco-Marín, A.F. Pérez-Cadenas, F.J. Maldonado-Hódar, Fitting the porosity of carbon xerogel by CO2 activation to improve the TMP/n-octane separation, Microporous Mesoporous Mater. 209 (2015) 10–17. doi:10.1016/J.MICROMESO.2015.01.010.

[23] S. Morales-Torres, F.J. Maldonado-Hódar, A.F. Pérez-Cadenas, F. Carrasco-Marín, Structural characterization of carbon xerogels: From film to monolith, Microporous Mesoporous Mater. 153 (2012) 24–29. doi:10.1016/J.MICROMESO.2011.12.022.

[24] A. Abdelwahab, J. Castelo-Quibén, M. Pérez-Cadenas, A. Elmouwahidi, F. Maldonado-Hódar, F. Carrasco-Marín, A. Pérez-Cadenas, Cobalt-Doped Carbon Gels as Electro-Catalysts for the Reduction of CO2 to Hydrocarbons, Catalysts. 7 (2017) 25. doi:10.3390/catal7010025.

[25] A.F. Pérez-Cadenas, C.H. Ros, S. Morales-Torres, M. Pérez-Cadenas, P.J. Kooyman, C. Moreno-Castilla, F. Kapteijn, Metal-doped carbon xerogels for the electro-catalytic conversion of CO2 to hydrocarbons, Carbon N. Y. 56 (2013) 324–331. doi:10.1016/J.CARBON.2013.01.019.

[26] E. Gallegos-Suárez, A.F. Pérez-Cadenas, F.J. Maldonado-Hódar, F. Carrasco-Marín, On the micro-and mesoporosity of carbon aerogels and xerogels. The role of the drying conditions during the synthesis processes, Chem. Eng. J. 181 (2012) 851–855. doi:10.1016/j.cej.2011.12.002.

[27] C. Lin, J.A. Ritter, Effect of synthesis pH on the structure of carbon xerogels, Carbon N. Y. 35 (1997) 1271–1278. doi:10.1016/S0008-6223(97)00069-9.

[28] C. Du, Q. Tan, G. Yin, J. Zhang, 5 - Rotating Disk Electrode Method, in: W. Xing, G. Yin, J. Zhang (Eds.), Rotating Electrode Methods Oxyg. Reduct. Electrocatal., Elsevier, Amsterdam, 2014: pp. 171–198. doi:https://doi.org/10.1016/B978-0-444-63278-4.00005-7.

[29] H. Shibata, J.A. Moulijn, G. Mul, Enabling Electrocatalytic Fischer--Tropsch Synthesis from Carbon Dioxide Over Copper-based Electrodes, Catal. Letters. 123 (2008) 186. doi:10.1007/s10562-008-9488-3.

[30] D. Fairén-Jiménez, F. Carrasco-Marín, C. Moreno-Castilla, Inter- and intra-primary-particle structure of monolithic carbon aerogels obtained with varying solvents, Langmuir. 24 (2008) 2820–2825. doi:10.1021/la703386q.

[31] V. Uvarov, I. Popov, Metrological characterization of X-ray diffraction methods for determination of crystallite size in nano-scale materials, Mater. Charact. 58 (2007) 883–891. doi:10.1016/J.MATCHAR.2006.09.002.

[32] Y. Zhao, M. Liu, L. Gan, X. Ma, D. Zhu, Z. Xu, L. Chen, Ultramicroporous Carbon Nanoparticles for the High-Performance Electrical Double-Layer Capacitor Electrode, Energy & Fuels. 28 (2014) 1561–1568. doi:10.1021/ef402070j.

[33] E.B. Nursanto, H.S. Jeon, C. Kim, M.S. Jee, J.H. Koh, Y.J. Hwang, B.K. Min, Gold catalyst reactivity for CO 2 electro-reduction: From nano particle to layer, Catal. Today. 260 (2016) 107–111. doi:10.1016/j.cattod.2015.05.017.

[34] S. Back, M.S. Yeom, Y. Jung, Active sites of Au and Ag nanoparticle catalysts for CO2 electroreduction to CO, Acs Catal. 5 (2015) 5089–5096. doi:10.1021/acscatal.5b00462.


UNIVERSITAS · GRANATENSIS
PLUS
ULTRA
· 1531 ·


UNIVERSITAS · GRANATENSIS
PLUS
ULTRA
· 1531 ·

CAPÍTULO VII

SYNTHESIS AND CHARACTERIZATION OF CARBON SPHERES DOPED WITH NITROGEN AND TUNGSTEN FOR THE OXYGEN REDUCTION REACTION


UNIVERSITAS · GRANATENSIS
PLUS ULTRA
· 1531 ·

VII. 1 Introduction

Taking into account the energy and environmental crisis that we are suffering nowadays, there is a growing interest in finding new sources of energy that respect the environment, especially for applications in the transport sector. The development of electric vehicles is nowadays one of the most promising alternatives to replace the combustion engines. Therefore, the production of electrical energy from chemical reactions through the use of fuel cells is a really interesting field from the industrial and fundamental research point of view [1–5]. The oxygen reduction reaction (ORR) is the one that takes place at the cathode of a fuel cell. In the literature published to date, several works can be found about the synthesis and optimization of electro-catalytic materials for this reaction [6–11].

Among them, the platinum-based electro-catalysts are the most studied, since Pt is the most active metal for ORR However, the increase in the price of platinum and other precious metals such as Pd or Ir makes it more difficult to market the devices that contain them. This is the reason why the non-precious metals electro-catalysts are more numerous and more studied to reduce the costs of the fuel cells [7,12–14].

In this regard, tungsten-based electro-catalysts are showing great interest recently [15–22]. For example, it has been suggested that tungsten carbide can improve the activity and dispersion of supported Pt [16,19,23,24]. Although some works that have developed electro-catalysts based on tungsten carbide and doped with iron and nitrogen showed an indirect pathway for ORR (2-electron pathway) [25], others have shown to work four electrons pathway [18,21]. Fe / Co / WC @ NC hybrid catalysts have also been synthesized, consisting of uniform Fe_3C and Co_3C nanoparticles encapsulated in graphitized carbon doped with nitrogen on their surface, and in turn wrapped with a tungsten carbide (WC) in the form of a plate that works as an efficient catalyst for oxygen reduction reaction

(ORR) [26]. It was shown that the presence of WC promotes the ORR activity of Fe/Co based electro-catalysts. The results suggest that this composite exhibits an efficient electro-catalytic activity, a greater durability and capacity for methanol tolerance in comparison with commercial Pt / C catalysts for ORR in alkaline medium. These results are similar to those obtained with tungsten-cobalt carbides encapsulated in carbon (CoWC @ C) [27].

Finally, there are also previous works using carbon gels doped with nitrogen as precursors of electro-catalysts based on tungsten carbide [22]. The obtaining results were close to those obtained with platinum catalyst in alkaline media, and even improved the onset potential. It should be noted that, in addition to the activity associated with tungsten carbide, the presence of mesoporosity also increases the electro-catalytic activity of these materials [18].

VII.2 Experimental

VII.2.1 Synthesis of materials

VII.2.1.1 Hydrothermal synthesis of polymer spheres

Polymeric nanospheres were obtained by sol-gel hydrothermal synthesis using monomers of pyrocatechol and formaldehyde in an ethanol:water aqueous solution and in the presence of ammonia. The procedure carried out is an extension of the Stöber method [28], specifically following the procedure recently used by Moreno et. al [29].

Firstly, 0.212 g pirocatechol (P) were dissolved in 60 mL of a water:EtOH solution (2.5:1 volume ratio), then, a NH_3 and formaldehyde (F) solution was added, with the molar ratios NH_3/P=1.5 and F/P=2. This mixture was placed into a 100 mL capacity autoclave (Parr Instruments) and located in an oven at 100 °C for 24 hours

After 24 hours the precipitate was filtered, washed with ethanol and the solvent was exchanged with acetone for 3 days, in which the acetone was changed daily. Finally the material was dried under an IR lamp. The organic gel spheres sample thus obtained, was named "S"

VII.2.1.2 Impregnation with the tungsten precursor.

The obtained organic gel spheres, S, were impregnated with a ammonium tungstate solution, [$(NH_4)_2(WO_4)$], by the incipient impregnation method. The solution volume used was the porous V_{TOTAL} of S obtained by mercury intrusion porosimetry. The impregnation was carried out with solutions of ammonium tungstate of different concentration to obtain doped spheres with 2%, 5% and 10% theoretical of W in the final carbon. To do the calculation, a mass loss of 50% was assumed during the carbonization. Once impregnated, they were dried under IR lamp overnight.

VII.2.1.3 Carbonization of the polymeric spheres and the corresponding obtaining of the electro-catalysts.

Both, undoped (S) and doped ammonium tungstate (SW2, SW5 and SW10) polymeric spheres were carbonized under nitrogen atmosphere in a tubular oven at 900 °C with a heating rate of 2 °C/min. Once reached the 900 ºC, this temperature was kept for 2 hours. CS, CSW2, CSW5 and CSW10 samples were obtained following this procedure.

It should be noted that the presence of NH_3 in the synthesis, as well as, the impregnation with ammonium tungstate predicts a functionalization with nitrogen in these materials

VII.2.2 Electrochemical measurements

All the electrochemical measurements were carried out in a three electrode cell using the corresponding sample supported on the tip of the rotating disc electrode (RDE) as the working electrode.

Previously supporting every sample, the RDE tip, 0.071 cm^2 in area, was carefully polished with 0.3 μm grain size alumina powder.

To study the behaviour of materials in the absence and presence of oxygen, firstly, N_2 was bubbled through the electrolytic solution (KOH 0.1M) until all the oxygen has been removed and a cyclic voltammetry (CV) was performed from 0.4 V at -0.8 V with a sweeping rate of 50 mVs^{-1} at 1000 rpm. The same experiment was accomplished with the saturated oxygen solution.

To study the mechanism and parameters of the ORR, linear sweep voltametries (LSV) were performed with a potential sweeping speed of 5 mVs^{-1} at different sweeping speeds from 500 rpm to 4000 rpm, and in every cases the electrolytic solution is saturated with oxygen. The data of these experiments were adjusted to the Koutecky-Levich equation to obtain the number of electrons transferred, as well as the kinetic density current (j_k) and the ONSET potential, which the ORR starts.

VII.3 Results and Discussion

The analysis of the porosity and surface area of the materials was achieved by physical adsorption of N_2 at -196 ºC. The results are presented in Figure VII.1 and in Table VII.1 which includes the apparent surface area (S_{BET}), the micropores volume (W_0), the micropores average size (L_0), as well as the total contents nitrogen and tungsten. Figure VII.1 shows how the carbon spheres (SC) are non-microporous materials, and it can be deduced the presence of a certain mesoporosity and/or interparticular spaces of the

mesoporous order from their adsorption isotherm. On the other hand, all the tungsten-coated spheres show Type I - Type IV hybrid isotherms, typical of mesoporous solids but also with some adsorption at very low relative pressures, P/P_0, revealing the presence of micropores.

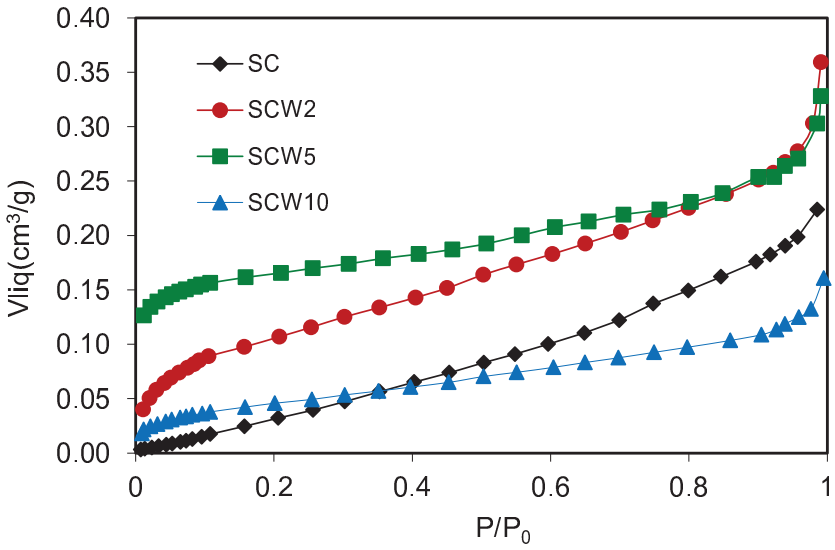

Figure VII.1. N_2-adsorption isotherms

The development of the porosity and the surface area in the tungsten spheres is probably due to the gasifying action of said metal during the carbonization [30]. Thus, a higher tungsten content should produce more gasification, as is clearly the case with samples SCW2 and SCW5. However, the SCW10 sample, although clearly more porous than the SC, has not followed the suggested trend, which may be due either to an extremely small particle size of W that causes a more attenuated gasification activity or a worse dispersion of the metallic phase on the surface of the sphere so that the gassing activity on the carbonaceous phase would be given to a lesser extent.

Table VII.1. Textural properties and total amount of W by TGA.

Sample	S_{BET} $m^2 \cdot g^{-1}$	W_0 $cm^3 \cdot g^{-1}$	L_0 nm	$W_{TOTAL-TGA}$ (%)
S	n.d.	-	-	0.0
SC	41	-	-	0.0
SCW2	254	0.107	2.7	2.7
SCW5	374	0.165	1.5	5.6
SCW10	96	0.043	2.4	10.0

Regarding the morphology of these materials, the images of scanning electron microscopy (SEM) and transmission electron microscopy (TEM) clearly show that spheres with average sizes between 300 and 400 nm of diameter have been obtained (Figures VII.2 and VII.3), mostly isolated, although partially fused aggregates are also observed, more abundant in the case of the tungsten spheres than in the SC sample. The presence of tungsten carbide particles has been detected in the tungsten spheres, by SEM and EDX analysis (Figures VII.2 and VII.3). The red mark in Fig. VII.2d indicates the exact point the EDX measurement. However, it was also found the presence of tungsten oxide particles by TEM (Fig. VII.4) and whose existence has been corroborated by XPS.

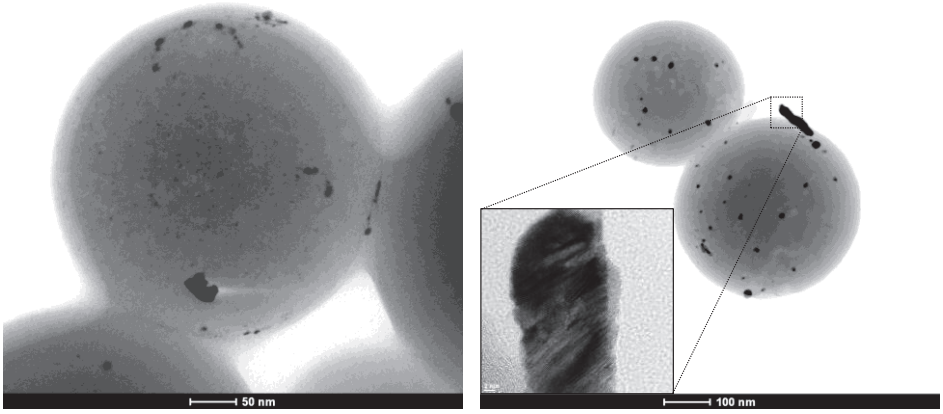

Figure VII.2. TEM and HRTEM images of SCW2

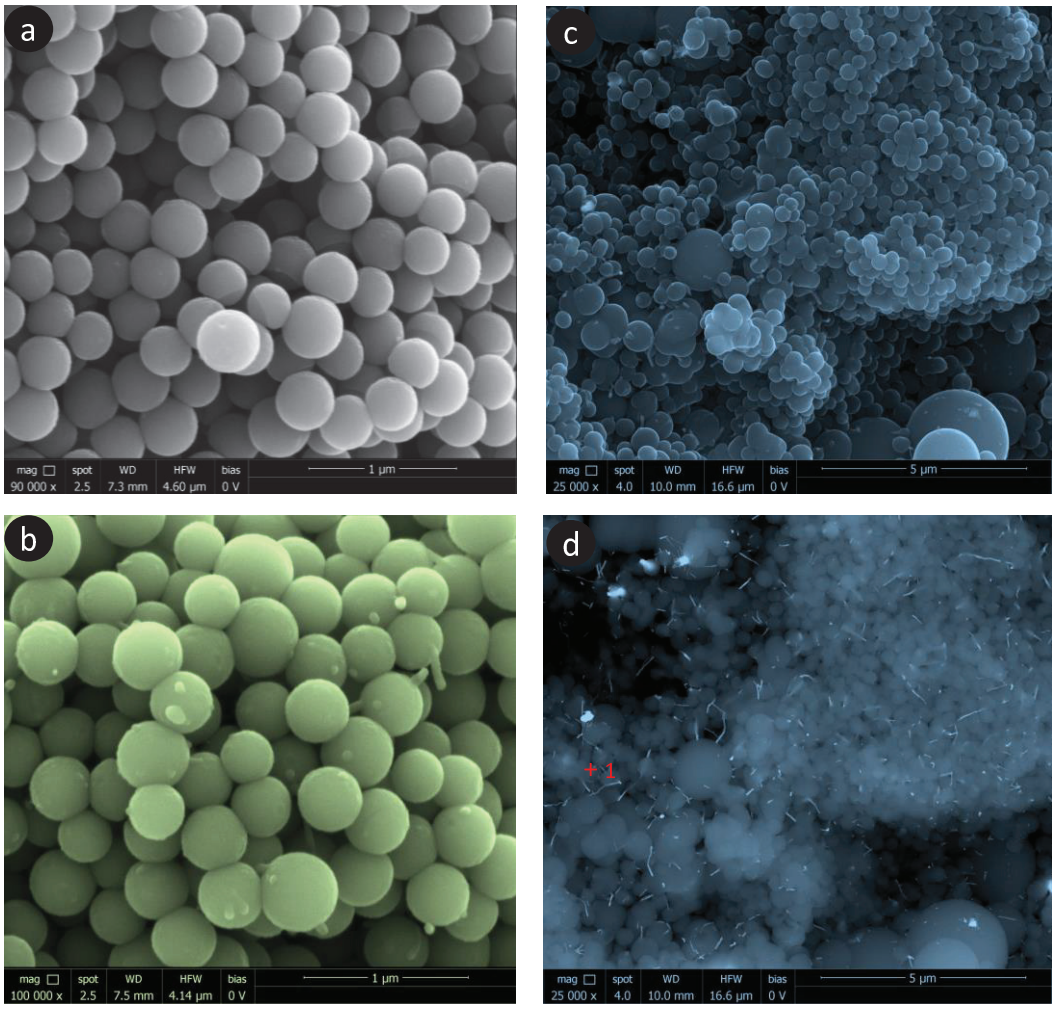

Figure VII.3. SEM images a) SC; b) SCW5; c) SCW10 with ETD detector and d) SCW10 with CBS detector

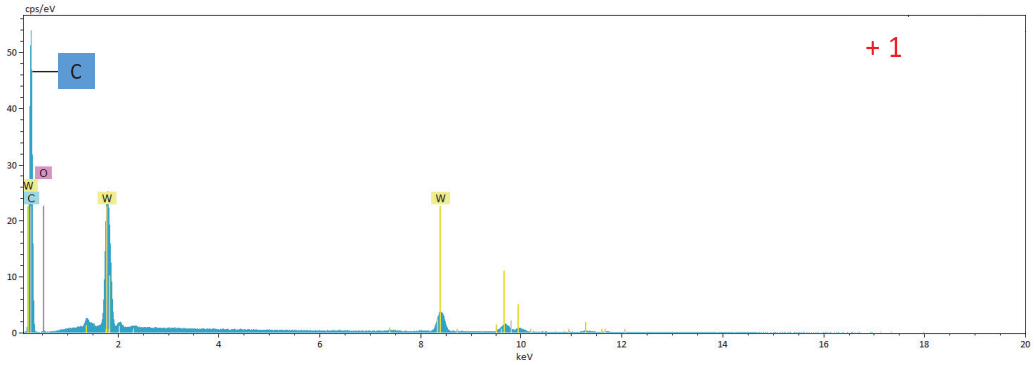

Figure VII.4. EDX analysis of the SCW10.

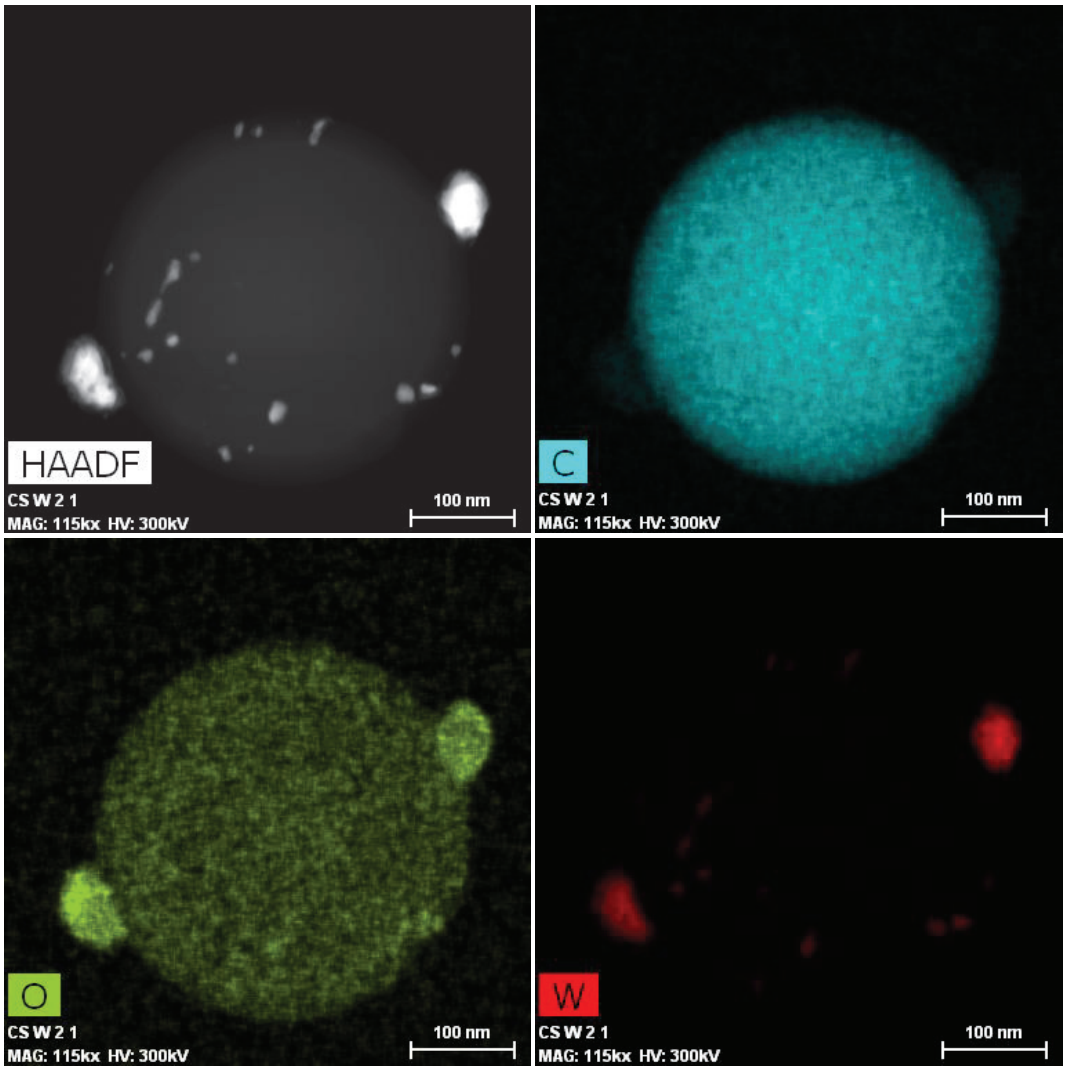

Figure VII.5 TEM-HAADF and EDX mapping images of SCW5

Table VII.2. Surface chemical composition XPS.

Sample	% C_{XPS}	% O_{XPS}	% N_{XPS}	% W_{XPS}
SC	76.9	16.3	6.8	0
SCW2	92.3	4	1.5	2.2
SCW5	91.4	4	1.3	3.2
SCW10	83.4	4.9	1.6	10.1

Tables VII.1 to VII.5 show chemical characterization data of the materials. It should be noted the good adjustment of the metallic content obtained with respect to the theoretically calculated (Table VII.1). On the other hand, the high content in superficial N of the SC sample is very remarkable, which reaches 7%, a really relevant fact taking into account the high temperature of carbonization (900 ºC) and the thermal lability of this type of surface complexes [31]. On the other hand, when the organic gel spheres impregnated with tungsten were carbonized, a decrease in both the oxygen and nitrogen content relative to the SC material was clearly produced, and in parallel to the gasification process. Even so, C-spheres coated with tungsten also have a notable percentage of surface nitrogen, around 1.5% by weight (Table VII.2). This surface nitrogen is part of different functionalities or surface complexes of nitrogen (Table VII.3), type N-6 or pyridinic, type N-Q or quaternary, or type N-X that would correspond to pyridine nitrogen bound to oxygenated groups [32]. Figure VII.6 shows the spectra deconvolution of the N_{1S} region for the SC sample.

The N-Q type groups are the most numerous in all prepared materials, exceeding in all cases 50% of the total surface nitrogen (Table VII.3), meanwhile the remaining nitrogen content is distributed in two equal parts between N-6 and NX groups.

Finally, Table VII.4 shows the surface tungsten species detected by XPS, as well as the binding energies (E.L.) to which they have been detected. It should be noted that % W_{XPS} is lower than the total obtained by TGA (Table VII.1) in SCW2 and SCW5 samples, especially in the second one, which would indicate a greater penetration of the metallic phase within the porous structure of the developed material during gasification. However,this phenomenon doesn't seem to be happening in the same way in SCW10 sample, which could justify the surface area results described above.

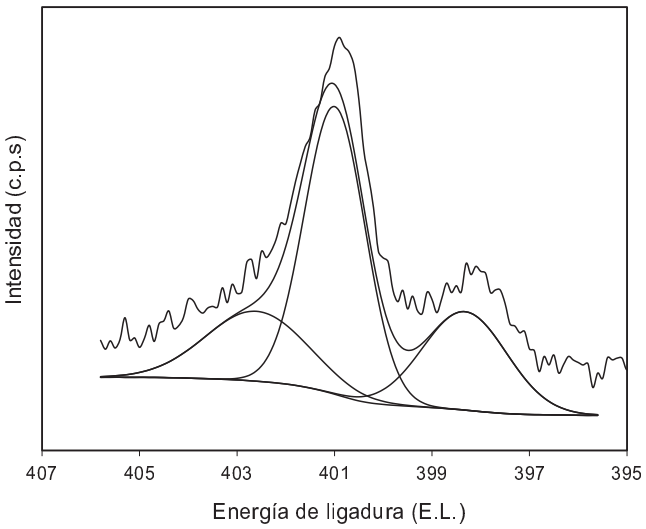

Figure VII.6. Deconvoluted XPS spectra of the N_{1s} región for the SC sample.

Table VII.3. Surface content of nitrogen complexes obtained by XPS, with the corresponding binding.

Sample	% N_{XPS} total	% N-6	% N-Q	% N-X
SC	**6.8**	25	55	22
SCW2	**1.5**	18	66	16
SCW5	**1.3**	23	57	20
SCW10	**1.6**	25	53	22
E.L. (eV)	**N1s**	398.5	401	402.5

Table VII.4. Surface tungsten content obtained by XPS. The percentage of both species are referred to the total.

Sample	% W_{XPS} total	% WC	% WO_3
SC	**0**	-	-
SCW2	**2.2**	44	56
SCW5	**3.2**	57	43
SCW10	**10.1**	68	32
E.L. (eV)	**$W4f_{7/2}$**	32	35.7

In any case, Table VII.4 clearly shows that all materials doped with tungsten have WC and WO_3 on their external surface, as the SEM-EDX and TEM-EDX advanced us. However, the presence of WC gradually increases with the total content of tungsten, while that of WO_3 decreases. Thus, while in SCW2 sample, the presence of WC corresponds to 44% by weight of the total tungsten, in the sample SCW10 the presence of WC is clearly the majority with 68%. As an example, figure VII.7 shows the deconvolution of the W_{4f} spectra of sample SCW5.

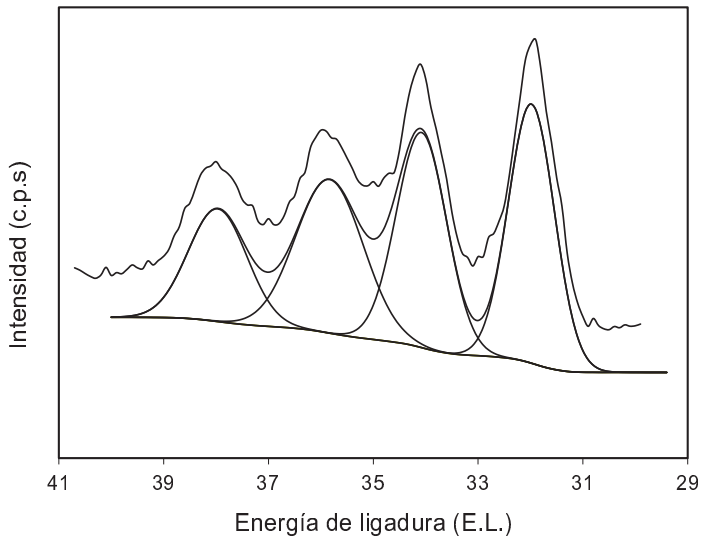

Figure VII.7. Deconvoluted XPS spectra of the W_{4f} región for the SCW5 sample.

Figure VII.8 shows the diffraction spectra of the materials. In all the tungsten-coated spheres samples, the presence of WC and W_2C has been detected. In addition, there also appear to be W^0 in CSW5 sample. However, the formation of WO_3 hasn't been detected in any sample, which suggests that this phase is composed of amorphous particles, or extremely small particles that are not diffracting; the formation of WO_3 (detected by XPS) would be related to a tungsten oxidation by exposing the samples to the air, mainly from the W^0 phase, since the carbide phases are more stable to spontaneous oxidation.

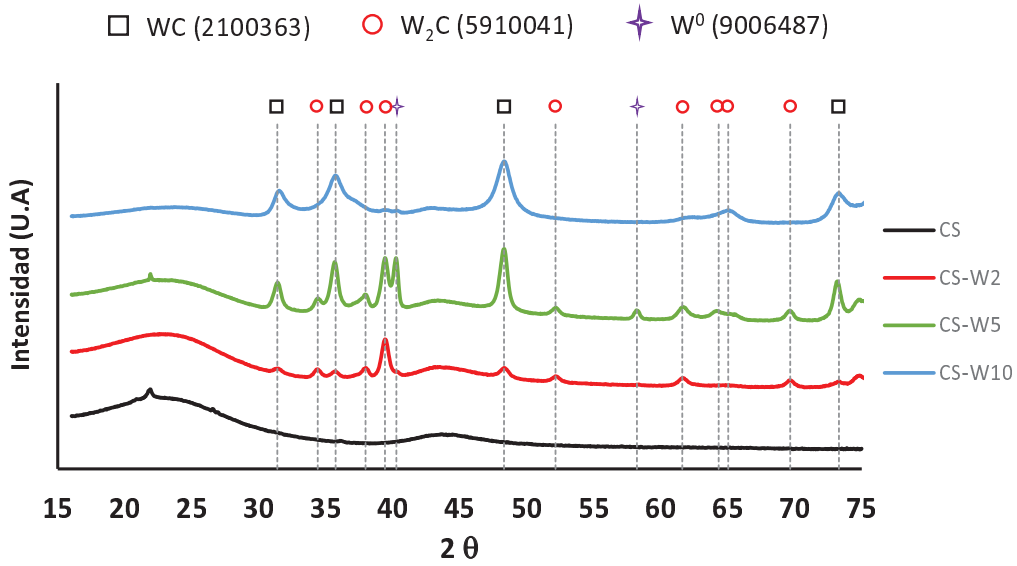

Figure VII.12. XRD patterns of all samples and the corresponding signal for WC, W_2C and W^0 phases.

The average crystal sizes were obtained by applying the Scherrer equation to the diffraction data (Table VII.5).

Table VII.5. Average crystal size obtained by XRD.

Sample	d (nm)		
	WC	W_2C	W°
CSW2	11.4	14.1	-
CSW5	12.2	13.6	18.1
CSW10	7.1	-	-

Figure VII.13 shows the cyclic voltammetries (CVs) performed in KOH 0.1 M, in absence of oxygen (blue) and saturated in O_2 (red), in which, it is observed the activity in the electro-reduction of O_2 for all samples. After the CVs, the LSV curves were obtained at different rotation speeds (Figure VII.14), for all the samples. Data from the LSVs were fitted to the Koutecky-Levich equation and the parameters obtained are collected in Table VII.6.

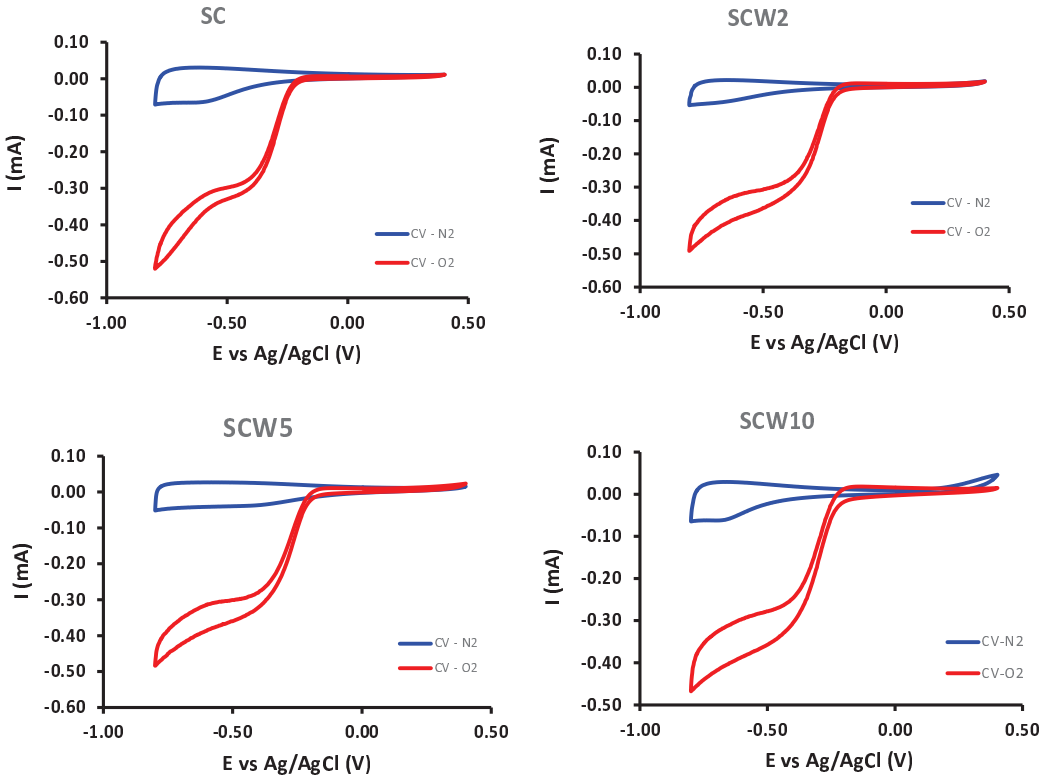

Figure VII.13. Cyclic Voltagrams at 1000 rpm and 50 mV/s

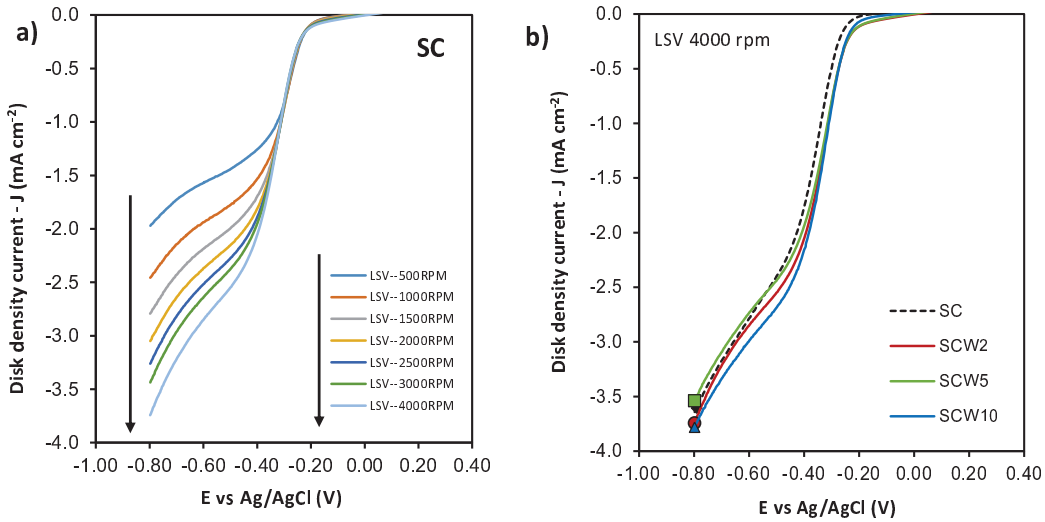

Figure VII.14. LSV curves for *SC* at different RDE rates (a), and LSV curves at 4000 rpm for all samples (b)

Table VII.6. Electrochemical parameters obtained from LSV curves

Sample	n*	j_K* mA·cm^{-2}	E_{ONSET} V
SC	3.51	6.31	-0.265
CSW2	3.19	7.14	-0.253
CSW5	3.09	6.6	-0.243
CSW10	3.17	7.28	-0.241

* obtained at -0.8 V

All the calculated parameters, n, j_k and E_{ONSET} are shown in Table VII.6. As it can be observed, all the samples catalyze the oxygen electro-reduction reaction through a mixed pathway of 2 and 4 electrons. But the spheres with the highest nitrogen content (SC) tend, to a greater extent, to carry out electro-catalysis by the 4 electrons pathway. However, they need some optimization to advance on an exclusive electro-catalytic pathway. This improvement in activity for the SC material is due to the high nitrogen content, especially the quaternary nitrogen [33].

The presence of tungsten on these spheres does not seem, a priori, to improve the electro-catalytic behaviour, nevertheless it is worth mentioning that the nitrogen content in these spheres is five times lower than in SC sample, so that a certain positive effect must presuppose in accordance with the results shown in Table VII.6. In addition, both current and potential kinetic density values improve considerably with the presence of tungsten. However, it is obvious that the clear synergetic effect that the WC has with other electro-catalytic metals does not seem to have it in the same extent with the superficial nitrogen complexes of these spheres.

VII.4 Conclusions

In the present work, carbon nanospheres have been obtained by a simple solvothermal method. These spheres stand out for the high nitrogen content despite the high carbonization temperature. In addition, during this carbonization process, tungsten carbide was generated, in those cases in which a tungsten precursor was added, thus obtaining carbon spheres doped with nitrogen and coated with CW.

The presence of tungsten during the carbonization produced the partial gasification of the spheres favouring the development of the porosity and the surface area.

Finally, all the prepared materials in this work carried out the oxygen electro-reduction of by a mixed pathway of 2 and 4 electrons, highlighting the CS spheres thanks to their high nitrogen content.

VII.5 References

[1] F. Barbir, PEM fuel cells: theory and practice, Academic Press, 2012.

[2] K. Kendall, B.G. Pollet, Hydrogen and fuel cells in transport, in: Compr. Renew. Energy, 2012: pp. 301–313. doi:10.1016/B978-0-08-087872-0.00419-4.

[3] L. Carrette, K.A. Friedrich, U. Stimming, Fuel Cells - Fundamentals and Applications, Fuel Cells. 1 (2002) 5–39. doi:10.1002/1615-6854(200105)1:1<5::aid-fuce5>3.0.co;2-g.

[4] A. de Frank Bruijn, G.J.M. Janssen, ORR, Fuel Cells Hydrog. Prod. A Vol. Encycl. Sustain. Sci. Technol. Second Ed. (2019) 195–234.

[5] A.B. Stambouli, Fuel cells: The expectations for an environmental-friendly and sustainable source of energy, Renew. Sustain. Energy Rev. 15 (2011) 4507–4520. doi:10.1016/j.rser.2011.07.100.

[6] S. Sui, X. Wang, X. Zhou, Y. Su, S. Riffat, C. Liu, A comprehensive review of Pt electrocatalysts for the oxygen reduction reaction: Nanostructure, activity, mechanism and carbon support in PEM fuel cells, J. Mater. Chem. A. 5 (2017) 1808–1825. doi:10.1039/C6TA08580F.

[7] D. Banham, S. Ye, K. Pei, J.-I. Ozaki, T. Kishimoto, Y. Imashiro, A review of the stability and durability of non-precious metal catalysts for the oxygen reduction reaction in proton exchange membrane fuel cells, J. Power Sources. 285 (2015) 334–348. doi:10.1016/j.jpowsour.2015.03.047.

[8] D.H. Jung, S.J. Bae, S.J. Kim, K.S. Nahm, P. Kim, Effect of the Pt precursor on the morphology and catalytic performance of Pt-impregnated on Pd/C for the oxygen reduction reaction in polymer electrolyte fuel cells, Int. J. Hydrogen Energy. 36 (2011) 9115–9122. doi:10.1016/j.ijhydene.2011.04.166.

[9] M.M. Hossen, K. Artyushkova, P. Atanassov, A. Serov, Synthesis and characterization of high performing Fe-NC catalyst for oxygen reduction reaction (ORR) in Alkaline Exchange Membrane Fuel Cells, J. Power Sources. 375 (2018) 214–221. doi:10.1016/j.jpowsour.2017.08.036.

[10] T. Ishii, T. Maie, N. Kimura, Y. Kobori, Y. Imashiro, J.-I. Ozaki, Enhanced catalytic activity of nanoshell carbon co-doped with boron and nitrogen in the oxygen reduction reaction, Int. J. Hydrogen Energy. 42 (2017) 5–12. doi:10.1016/j.ijhydene.2017.05.003.

[11] D.Y. Chung, J.M. Yoo, Y. Sung, Highly Durable and Active Pt- Based Nanoscale Design for Fuel- Cell Oxygen- Reduction

Electrocatalysts, Adv. Mater. 30 (2018) 1704123. doi:10.1016/j.ijhydene.2018.11.210.

[12] A. Sarapuu, L. Samolberg, K. Kreek, M. Koel, L. Matisen, K. Tammeveski, Cobalt- and iron-containing nitrogen-doped carbon aerogels as non-precious metal catalysts for electrochemical reduction of oxygen, J. Electroanal. Chem. 746 (2015) 9–17. doi:https://doi.org/10.1016/j.jelechem.2015.03.021.

[13] A. Elmouwahidi, E. Bailón-García, A.F. Pérez-Cadenas, J. Castelo-Quibén, F. Carrasco-Marín, Carbon-vanadium composites as non-precious catalysts for electro-reduction of oxygen, Carbon N. Y. 144 (2019) 289–300. doi:10.1016/j.carbon.2018.12.038.

[14] Z. Chen, D. Higgins, A. Yu, L. Zhang, J. Zhang, A review on non-precious metal electrocatalysts for PEM fuel cells, Energy Environ. Sci. 4 (2011) 3167. doi:10.1039/c0ee00558d.

[15] K. Lee, A. Ishihara, S. Mitsushima, N. Kamiya, K.I. Ota, Transition metal carbides for new cathode material of polymer electrolyte fuel cell, ECS Proc. Vol. 2004 (2004) 213–221. doi:10.1149/200421.0213PV.

[16] M. Shao, B. Merzougui, K. Shoemaker, L. Stolar, L. Protsailo, Z.J. Mellinger, I.J. Hsu, J.G. Chen, Tungsten carbide modified high surface area carbon as fuel cell catalyst support, J. Power Sources. 196 (2011) 7426–7434.

[17] Y. Liu, T.G. Kelly, J.G. Chen, W.E. Mustain, Metal carbides as alternative electrocatalyst supports, Acs Catal. 3 (2013) 1184–1194.

[18] J.-S. Moon, Y.-W. Lee, S.-B. Han, D.-H. Kwak, K.-H. Lee, A.-R. Park, J.I. Sohn, S.N. Cha, K.-W. Park, Iron–nitrogen-doped mesoporous tungsten carbide nanostructures as oxygen reduction electrocatalysts, Phys. Chem. Chem. Phys. 16 (2014) 14644–14650. doi:10.1039/C4CP01157K.

[19] L. Xiong, L. Zheng, C. Liu, L. Jin, Q. Liu, J. Xu, Tungsten carbide microspheres with high surface area as platinum catalyst supports for enhanced electrocatalytic activity, J. Electrochem. Soc. 162 (2015) F468–F473.

[20] K. Huang, K. Bi, J.C. Xu, C. Liang, S. Lin, W.J. Wang, T.Z. Yang, Y.X. Du, R. Zhang, H.J. Yang, Novel graphite-carbon encased tungsten carbide nanocomposites by solid-state reaction and their ORR electrocatalytic performance in alkaline medium, Electrochim. Acta. 174 (2015) 172–177.

[21] L. Song, T. Wang, Y. Wang, H. Xue, X. Fan, H. Guo, W. Xia, H. Gong, J. He, Porous iron-tungsten carbide electrocatalyst with high activity

and stability toward oxygen reduction reaction: from the self-assisted synthetic mechanism to its active-species probing, ACS Appl. Mater. Interfaces. 9 (2017) 3713–3722. doi:10.1021/acsami.6b14754.

[22] H. Zhu, Z. Sun, M. Chen, H. Cao, K. Li, Y. Cai, F. Wang, Highly porous composite based on tungsten carbide and N-doped carbon aerogels for electrocatalyzing oxygen reduction reaction in acidic and alkaline media, Electrochim. Acta. 236 (2017) 154–160. doi:10.1016/j.electacta.2017.02.156.

[23] Y. Sohn, J.Y. Jung, P. Kim, Facile synthesis of tungsten carbide-carbon composites for oxygen reduction reaction, Korean J. Chem. Eng. 34 (2017) 2162–2168. doi:10.1007/s11814-017-0124-z.

[24] J.L. Bott-Neto, W. Beck Jr, L.C. Varanda, E.A. Ticianelli, Electrocatalytic activity of platinum nanoparticles supported on different phases of tungsten carbides for the oxygen reduction reaction, Int. J. Hydrogen Energy. 42 (2017) 20677–20688. doi:10.1016/j.ijhydene.2017.07.065.

[25] U.A. do Rêgo, T. Lopes, J.L. Bott-Neto, A.A. Tanaka, E.A. Ticianelli, Oxygen reduction electrocatalysis on transition metal-nitrogen modified tungsten carbide nanomaterials, J. Electroanal. Chem. 810 (2018) 222–231. doi:10.1016/j.jelechem.2018.01.013.

[26] J. Zhang, J. Chen, Y. Jiang, F. Zhou, G. Wang, R. Wang, Tungsten carbide encapsulated in nitrogen-doped carbon with iron/cobalt carbides electrocatalyst for oxygen reduction reaction, Appl. Surf. Sci. 389 (2016) 157–164. doi:10.1016/J.APSUSC.2016.07.071.

[27] G. Zhong, H. Wang, H. Yu, F. Peng, A Novel Carbon-Encapsulated Cobalt-Tungsten Carbide as Electrocatalyst for Oxygen Reduction Reaction in Alkaline Media, Fuel Cells. 13 (2013) 387–391. doi:10.1002/fuce.201300057.

[28] W. Stöber, A. Fink, E. Bohn, Controlled growth of monodisperse silica spheres in the micron size range, J. Colloid Interface Sci. 26 (1968) 62–69. doi:10.1016/0021-9797(68)90272-5.

[29] C. Moreno-Castilla, H. García-Rosero, F. Carrasco-Marín, Synthesis and characterization of solid polymer and carbon spheres derived from an emulsion polymerization reaction of different phenolic compounds with formaldehyde, Colloids Surfaces A Physicochem. Eng. Asp. 520 (2017) 488–496. doi:10.1016/j.colsurfa.2017.02.021.

[30] F.J. Maldonado-Hódar, A.F. Pérez-Cadenas, C. Moreno-Castilla, Morphology of heat-treated tunsgten doped monolithic carbon aerogels, Carbon N. Y. 41 (2003) 1291–1299. doi:10.1016/S0008-6223(03)00069-1.

[31] M. Pérez-Cadenas, C. Moreno-Castilla, F. Carrasco-Marín, A.F. Pérez-Cadenas, Surface chemistry, porous texture, and morphology of N-doped carbon xerogels, Langmuir. 25 (2008) 466–470. doi:10.1021/la8027786.

[32] Z. Zapata-Benabithe, F. Carrasco-Marín, C. Moreno-Castilla, Preparation, surface characteristics, and electrochemical double-layer capacitance of KOH-activated carbon aerogels and their O-and N-doped derivatives, J. Power Sources. 219 (2012) 80–88.

[33] D. Geng, Y. Chen, Y. Chen, Y. Li, R. Li, X. Sun, S. Ye, S. Knights, High oxygen-reduction activity and durability of nitrogen-doped graphene, Energy Environ. Sci. 4 (2011) 760–764. doi:10.1039/C0EE00326C.


UNIVERSITAS · GRANATENSIS
PLUS
ULTRA
· 1531 ·

CAPÍTULO VIII

CONCLUSIONES GENERALES


UNIVERSITAS · GRANATENSIS
PLUS
ULTRA
· 1531 ·

En la presente Tesis Doctoral se han preparado materiales avanzados basados en carbono a partir de diferentes tipos de polímeros orgánicos. Los polímeros utilizados han sido, por una parte, residuos plásticos urbanos cuya composición principal es polietileno de baja densidad (LDPE), así como LDPE comercial de alta pureza. Por otra parte, se han sintetizado polímeros, o geles orgánicos, a partir de monómeros del tipo bencenodiol-formaldehído mediante distintos métodos como precursores de diferentes materiales avanzados de carbono. Parte de estos materiales se han dopado con metales de transición, Fe, Co, Ni, W, y/o con nanotubos o nanoconos de carbono.

Por un lado, se ha estudiado como afecta el método de preparación de los materiales y el contenido dopante de los mismos en sus características químico-físicas, y finalmente, todos estos materiales se han utilizado como electro-catalizadores para la reducción de oxígeno y/o dióxido de carbono.

En función del tipo de pirólisis se ha determinado que la carbonización de LDPE en un reactor cerrado da lugar a densas microesferas con alto grado de grafitización, lo cual fue puesto de manifiesto tanto por espectroscopía Raman como por Difracción de Rayos-X. Se ha observado que estas microesferas se han producido como consecuencia de la presión autógena del proceso, ya que, la pirólisis de LDPE en una celda abierta (en la cual no se ha generado presión) no dio lugar a materiales esféricos. Por otro lado, el dopado durante el proceso de síntesis de los geles orgánicos con los metales de transición Fe, Co y Ni afectó a la morfología de material sintetizado, aunque bien es cierto que en distinta medida. Así, se han formado nanofibras de carbono en presencia de los tres metales, pero con mayor tamaño en el caso del dopado con cobalto, habiendo obtenido materiales compuestos carbono-nanofibras en todos los casos.

Los materiales obtenidos a partir de residuos plásticos han manifestado actividad electro-catalítica en la reacción de electro-reducción de dióxido de carbono y se han obtenido en todos los casos (con Fe, Co o Ni) hidrocarburos ligeros de 1 a 4 átomos de carbono. Entre ellos, destaca el cobalto por presentar la mayor selectividad hacia hidrocarburos de tipo C3.

Por otra parte, las microesferas obtenidas a alta presión presentan excelente actividad en la reacción de electro-reducción de oxígeno. Se observa el efecto sinérgico de las fases carbono-metal, mejorando en todos los casos los parámetros de densidad de corriente cinética y el potencial de comienzo de la reacción. En este caso, destacan los materiales dopados con Fe por ser capaces de transferir 4 electrones, y con cobalto, que pese a no alcanzar una transferencia de 4 electrones, su intercambio es más constante durante los potenciales aplicados.

En cuanto a los materiales obtenidos a partir de la policondensación de resorcinol/pirocatecol con formaldehído, hemos logrado obtener esferas de carbono de tamaño nanométrico. Se desarrolló elevada área superficial y gran volumen de mesoporos cuando se realizó la condensación de resorcinol con formaldehído por el método de emulsión inversa. Además, se puso de manifiesto la influencia del dopado con nanotubos y nanoconos, así como el dopado, o simplemente posterior impregnación, con Ni. Estos materiales se utilizaron como cátodo en las reacciones de electro-reducción de CO_2 y electro-reducción de oxígeno obteniendo resultados muy interesantes. Se observa que la presencia de nanomateriales mejora la conductividad del material y por lo tanto mejora la actividad electro-catalítica. La presencia de Ni mejora considerablemente la actividad, sobretodo, cuando el níquel se encuentra en la superficie de las esferas al depositarlo mediante impregnación incipiente.

Finalmente, mediante síntesis solvotermal y posterior carbonización se obtuvieron esferas de carbono no microporosas dopadas con un elevado

contenido de nitrógeno. El recubrimiento de las esferas de gel orgánico con wolframio y su posterior carbonización produjo un claro desarrollo de la microporosidad debido a un efecto de gasificación catalizado por este metal, mientras que se redujo el contenido de nitrógeno superficial. De este modo, se obtuvieron esferas recubiertas con las fases de óxido de wolframio y carburo, incluidos los carburos WC y W_2C, con tamaños de cristal inferiores a 20 nm. Cabe destacar que también se ha detectado la presencia de partículas de wolframio con aspecto filamentoso homogéneamente distribuidas por la superficie de las esferas. Todos estos materiales fueron capaces de reducir al oxígeno mediante una vía mixta de 2-4 electrones, incluso las esferas sin recubrimiento de wolframio. La presencia de wolframio, a priori, parece no influir notablemente en la actividad electro-catalítica. Sin embargo, no se puede obviar el hecho de que el dopado con wolframio produce una clara disminución del contenido en complejos superficiales nitrógeno, siendo estos reconocidos como importantes inductores de actividad en ORR, por tanto, no se puede descartar un efecto promotor del W sobre la actividad electro-catalítica de estos materiales en ORR